

การพัฒนาไบโอเซนเซอร์ชนิดควอทซ์คริสตัลไมโครบาลานซ์ เพื่อการตรวจวัดตัวบ่งชี้  
ของการเป็นโรคหัวใจ

นางสาวกรองกมล วงษ์เอก

วิทยานิพนธ์นี้เป็นส่วนหนึ่งของการศึกษาตามหลักสูตรปริญญาวิทยาศาสตรดุษฎีบัณฑิต  
สาขาวิชาวิทยาศาสตร์นาโนและเทคโนโลยี  
บัณฑิตวิทยาลัย จุฬาลงกรณ์มหาวิทยาลัย  
ปีการศึกษา 2553  
ลิขสิทธิ์ของจุฬาลงกรณ์มหาวิทยาลัย

DEVELOPMENT OF A QUARTZ CRYSTAL MICROBALANCE BIOSENSOR  
FOR CARDIOVASCULAR MARKER DETECTION

Miss Krongkamol Wong-ek

A Dissertation Submitted in Partial Fulfillment of the Requirements  
for the Degree of Doctor of Philosophy Program in Nanoscience and Technology

(Interdisciplinary Program)

Graduate School

Chulalongkorn University

Academic Year 2010

Copyright of Chulalongkorn University

Thesis Title DEVELOPMENT OF A QUARTZ CRYSTAL  
MICROBALANCE BIOSENSOR FOR  
CARDIOVASCULAR MARKER DETECTION

By Miss Krongkamol Wong-ek

Field of Study Nanoscience and Technology

Thesis Advisor Associate Professor Orawon Chailapakul, Ph. D.


Thesis Co-Advisor Adisorn Tuantranont, Ph. D.


---

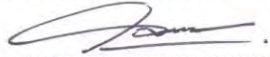
Accepted by the Graduate School, Chulalongkorn University in Partial  
Fulfillment of the Requirements for the Doctoral Degree

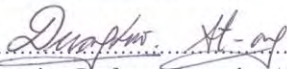
..... Dean of the Graduate School  
(Associate Professor Pornpote Piumsomboon, Ph. D.)

THESIS COMMITTEE

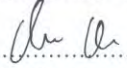
  
..... Chairman  
(Associate Professor Vudhichai Parasuk, Ph. D.)

  
..... Thesis Advisor  
(Associate Professor Orawon Chailapakul, Ph. D.)

  
..... Thesis Co-Advisor  
(Adisorn Tuantranont, Ph. D.)

  
..... Examiner  
(Associate Professor Duangdao Aht-Ong, Ph. D.)

  
..... Examiner  
(Assistant Professor Sukkaneste Tungasmita, Ph. D.)

  
..... External Examiner  
(Noppadon Nuntawong, Ph. D.)

กรองกลม วงษ์เอก : การพัฒนาไบโอเซนเซอร์ชนิดควอตซ์คริสตัลไมโครบาลานซ์ เพื่อการตรวจวัด  
 ตัวบ่งชี้ของการเป็นโรคหัวใจ (DEVELOPMENT OF A QUARTZ CRYSTAL MICROBALANCE  
 BIOSENSOR FOR CARDIOVASCULAR MARKER DETECTION) อาจารย์ที่ปรึกษาวิทยานิพนธ์  
 หลัก: รศ. ดร. อรวรรณ ชัยลภากุล, อาจารย์ที่ปรึกษาวิทยานิพนธ์ร่วม: ดร. อติสร เตือนตรานนท์, 129  
 หน้า.

การตรวจวัดระดับโปรตีนโทรโปนินที่เป็นตัวบ่งชี้ที่นิยมใช้มากที่สุดในการตรวจวินิจฉัยภาวะ  
 กล้ามเนื้อหัวใจตายเฉียบพลันซึ่งทำให้เกิดหัวใจวายขึ้น จากการศึกษานี้ได้ทำการศึกษาและพัฒนาเซนเซอร์เพื่อ  
 ใช้ในการตรวจวัดโทรโปนินที่มีหลักการที่แตกต่างกันสองชนิด ได้แก่ เซนเซอร์ในหลักการ Quartz Crystal  
 Microbalance ซึ่งมีการพัฒนาพื้นผิวหน้าของเซนเซอร์ด้วยชั้นของพอลิเมอร์ชนิดพีวีซีที่เกาะติดด้วยหมู่ของกรด  
 อินทรีย์ แล้วทำการศึกษาลักษณะของพื้นผิวภายใต้เงื่อนไขการเปลี่ยนแปลงความหนาของชั้นเกาะติดด้วยกล้อง  
 จุลทรรศน์อิเล็กตรอนแบบส่องกราดและกล้องจุลทรรศน์แรงอะตอม ผลที่ได้จากการพัฒนาพื้นผิวดังกล่าว  
 สามารถใช้ร่วมกับปฏิกิริยาทางภูมิคุ้มกันในการวิเคราะห์โปรตีนโทรโปนินที่ได้ในระยะเวลาที่รวดเร็ว และทำ  
 การคำนวณค่าส่วนต่างของความถี่ก่อนและหลังการวัดเป็นปริมาณโทรโปนินที่ถึงระดับ 5 นาโนกรัมต่อเลือด 1  
 มิลลิลิตร และเซนเซอร์ชนิดที่สองซึ่งใช้หลักการ Raman spectroscopy ได้ทำการพัฒนาพื้นผิวในระดับ  
 โครงสร้างนาโนด้วยการปลูกฟิล์มบางของธาตุอะลูมิเนียมและเงิน เพื่อเพิ่มระดับสัญญาณรบกวน และทำการ  
 ตรวจวัดโปรตีนโทรโปนินที่ด้วยการใช้เลเซอร์กระตุ้นอะตอมของธาตุเงินเพื่อให้เกิดการสั่นในระดับโมเลกุล  
 ผลที่ได้จากการพัฒนาเซนเซอร์ทั้งสองชนิดนี้ สามารถนำไปใช้ตรวจวัดโปรตีนโทรโปนินที่ได้และสามารถ  
 นำไปประยุกต์เพิ่มเติมเพื่อใช้สำหรับการตรวจวินิจฉัยโรคหัวใจในอนาคต

สาขาวิชา: วิทยาศาสตร์นาโนและเทคโนโลยี

ปีการศึกษา: 2553

ลายมือชื่อนิสิต *K. Wank.*

ลายมือชื่อ อ. ที่ปรึกษาวิทยานิพนธ์หลัก *Oran Chaitan*

ลายมือชื่อ อ. ที่ปรึกษาวิทยานิพนธ์ร่วม *Oran Chaitan*

## 5087752020: MAJOR: NANOSCIENCE AND TECHNOLOGY

KEYWORDS: QCM/ CARDIAC TROPONIN/ SERS.

KRONGKAMOL WONG EK: DEVELOPMENT OF A QUARTZ CRYSTAL MICROBALANCE BIOSENSOR FOR CARDIOVASCULAR MARKER DETECTION. THESIS ADVISOR: ASSOC. PROF. ORAWON CHAILAPAKUL, Ph. D., THESIS CO-ADVISOR: ADISORN TUANTRANONT, Ph. D., 129 pp.

Cardiac Troponin T (cTnT) detection is drawing a great interest due to its role in myocardial infarction diagnosis. In this study, we report relatively two new techniques to detect cTnT. First is by using quartz crystal microbalance (QCM) sensor. A sensitive detection is achieved by introducing QCM surface with a carboxylic polyvinyl chloride (PVC-COOH) immobilization layer. The surface morphologies of this polymer film under varied deposition thickness have been investigated by a field-emission scanning electron microscopy (FE-SEM) and an atomic force microscopy (AFM). The cTnT detection result from a modified QCM surface can be obtained within a short response time by a direct detection of the immuno-reaction and a direct conversion of mass accumulation into a frequency shift, representing a measurable electrical signal. The relationship between the cTnT concentration and the response current from the QCM sensor shows the detectability at the concentration of cTnT as low as 5 ng/ml. The second technique of cTnT detection is developed using surface enhanced Raman substrate (SERS). In latter technique, the nanostructure of silver film is fabricated for detection of troponin T protein by recording the shift in laser excitation wavelength due to vibrational modulation of specimens. These results suggest that both developed techniques for cTnT sensor may be a promising tool for future research as well as clinical diagnostics for the risk evaluation for cardiovascular diseases related to elevated cTnT levels.

Field of Study : Nanoscience and Technology

Academic Year : 2010

Student's Signature *K. Wong*

Advisor's Signature *Orawon Chailapakul*

Co-Advisor's Signature *Adisorn Tuantranont*

## ACKNOWLEDGEMENTS

First of all, I would like to thank my supervisor, Associate Professor Dr. Orawon Chailapakul, for her advice and guidance, and for giving me an opportunity to undertake this thesis project. I would like to acknowledge the National Science and Technology for Development Agency (NSTDA) through the Thai Graduate Institute of Science and Technology (TGIST) for financial support during my Ph.D. course.

I would especially like to thank my advisor, Dr. Adisorn Tuantranont, for the interesting subject of my Ph.D. dissertation and giving me an opportunity to realize own ideas and to know the value of working, Dr. Anurat Wisitsorraat, Mr. Kata Jaruwongrungrsee and staffs of Nanoelectronics and MEMS Laboratory, Dr. Pongpun Jindaudom, Dr. Pitak Eiamchai and Dr. Mati Horprathum from Photonics and Thin film Technology Laboratory, National Electronics and Computer Technology Center, National Science and Technology for Development Agency, Ministry of Science and Technology, Thailand, who welcome me and always prepare to help.

I wish to thank Dr. Noppadon Nuntawong, who is my day to day supervisor, for his contribution to this project, comments and valuable time during my doctoral program.

I also would like to thank my friends from Nanoscience and Technology Program for their help and friendship.

Last but not least, I would like to thank my beloved family for giving me the endless love, eternal understanding and immeasurable care throughout my life.

# CONTENTS

	<b>PAGES</b>
<b>ABSTRACT (IN THAI)</b> .....	iv
<b>ABSTRACT (IN ENGLISH)</b> .....	v
<b>ACKNOWLEDGMENTS</b> .....	vi
<b>CONTENTS</b> .....	vii
<b>LIST OF TABLES</b> .....	xi
<b>LIST OF FIGURES</b> .....	xii
<b>LIST OF ABBREVIATIONS AND SYMBOLS</b> .....	xvi
<b>CHAPTER I INTRODUCTION AND OUTLINE OF THE THESIS</b> .....	<b>1</b>
1.1 Introduction.....	1
1.2 Objectives of the research.....	2
1.3 Scope of the research.....	2
<b>CHAPTER II LITERATURE REVIEW</b> .....	<b>6</b>
2.1 Cardiovascular Biomarker.....	7
2.2 Rationale for choosing the Troponins.....	8
2.2.1 Biology of the Troponins.....	10
2.2.2 Characteristics of the Troponin Complex.....	11
2.2.3 Active Sites.....	12
2.2.3.1 Troponin T.....	12
2.2.3.2 Troponin I.....	12
2.2.3.3 Troponin C.....	13

2.3 Biomarker characteristics of the Troponins.....	13
2.3.1 Specificity.....	13
2.3.2 Sensitivity.....	14
2.4 Enzyme Linked Immunosorbant Assay method (ELISA).....	15
2.5 Theory of Quartz Crystal Microbalance (QCM).....	17
2.6 Development of modified Quartz Crystal Microbalance (QCM) biosensors....	21
2.7 Surface Enhanced Raman Scattering (SERS).....	22
2.7.1 SERS instrumentation.....	23
2.7.2 SERS application.....	26
2.8 Fabrication of Surface-enhanced Raman Spectroscopy (SERS).....	28
2.9 Previous works from other groups.....	29
<b>CHAPTER III MATERIALS AND METHODS.....</b>	<b>34</b>
3.1 Quartz Crystal Microbalance Experiments.....	34
3.1.1 Instruments and Equipments.....	34
3.1.2 Chemical and Reagents.....	36
3.1.3 Preparation of solutions.....	36
3.1.3.1 1 M Phosphate Buffer.....	37
3.1.3.2 50 mM 1-Ethyl-3-(3-dimethylaminopropyl) carbodiimide (EDC).....	37
3.1.3.3 25 mM N-hydroxysuccinimide.....	37
3.1.3.4 Carboxylic polyvinyl chloride.....	37
3.1.3.5 0.025 µg/mL Protein G.....	37
3.1.3.6 0.1 % Casein.....	37
3.1.3.7 Monoclonal antibody 9G6 for cTnT.....	38



3.1.3.8 Stock standard Solution of cTnT.....	38
3.1.4 Preparation of Polymer film fabrication and characterization.....	39
3.1.5 Flow injection system and stability of coated polymers under liquid flow.....	41
3.1.6 Binding experiments.....	43
3.2 Surface enhanced Raman Spectroscopy Experiments.....	47
3.2.1 Instruments and Equipments.....	47
3.2.2 Chemicals and reagents.....	48
3.2.3 Preparation of the solution.....	49
3.2.3.1 Methylene Blue.....	49
3.2.3.2 0.3 M Oxalic acid.....	50
3.2.3.3 5 wt % H <sub>3</sub> PO <sub>4</sub> .....	50
3.2.3.4 Stock standard Solution of cTnT.....	50
3.2.4 Preparation of the substrate.....	51
3.2.4.1 Sputtering system.....	51
3.2.4.2 Preparation of AAO templates.....	52
3.2.4.3 Sputtering of silver nanoparticles.....	53
3.2.4.4 Surface characterizations and analysis.....	53
3.2.5 Raman scattering characteristics.....	55
3.2.6 Procedure of binding experiments of cTnT.....	56
<b>CHAPTER IV RESULT AND DISCUSSION.....</b>	<b>57</b>
4.1 Quartz Crystal Microbalance Experiments.....	57
4.1.1 Polymer film morphologies on quartz crystal.....	57
4.1.2 Stability of the polymer film under PBS flow.....	63

4.1.3 Reusability of QCM sensor.....	64
4.2 QCM Experiments of cTnT.....	66
4.3 Surface Enhanced Raman Spectroscopy Experiments.....	74
4.3.1 Physical characteristics of SERS substrate.....	75
4.3.2 Calculation of Raman enhancement factors.....	86
4.4 SERS Experiments of cTnT.....	90
<b>CHAPTER V CONCLUSION.....</b>	<b>95</b>
5.1 Quartz Crystal Microbalance Biosensors.....	95
5.2 Surface Enhanced Raman Spectroscopy Substrates.....	96
5.3 Future prospect.....	97
<b>REFERENCES.....</b>	<b>98</b>
<b>BIOGRAPHY.....</b>	<b>108</b>
<b>APPENDIX A.....</b>	<b>109</b>

## LIST OF TABLES

<b>TABLE</b>	<b>PAGE</b>
Table 2.1 Biomarkers used or proposed for use in the clinical diagnosis of AMI.....	7
Table 3.1 List of Chemicals and Reagents and their suppliers of QCM.....	36
Table 3.2 Compositions of cTnT Standards solutions.....	39
Table 3.3 List of Chemicals and Reagents and their suppliers of SERS.....	49
Table 3.4 Compositions of Methylene Blue Standard Solution.....	50
Table 3.5 Compositions of cTnT Standards solutions.....	51
Table 4.1 RMS roughnesses of PVC-COOH coated quartz surfaces after polymer films at various thicknesses are deposited.....	60
Table 4.2 The Standard deviation of the vary flow rate.....	64
Table 4.3 Calculated $\Delta m$ and mass deposition.....	70
Table 4.4 Overview over Cardiac Troponin assays and the used method with the detection limit and the reference.....	72
Table 4.5 Frequency shift relate to cTnT concentration.....	73
Table 4.6 Band assignments and enhancement factors calculated from SERS spectra c-f plotted in Figure 4.16.....	88

## LIST OF FIGURES

FIGURE		PAGE
2.1	The characteristics of the Troponin complex.....	12
2.2	ELISA method.....	16
2.3	Schematic of AT cut quartz crystal surface.....	19
2.4	Gold (left) and silver (right) electrode quartz crystal compare with Thai baht coin (middle).....	20
2.5	Schematic diagram of Raman surface.....	22
2.6	(a) The scattering effect of Raman and (b) effect in wavelength.....	24
2.7	Crystal structure of cardiac troponin complex completely saturated with Ca <sup>2+</sup> .....	27
3.1	Airbrush equipment for spray coating.....	40
3.2	The continuous flow QCM sensor system.....	41
3.3	(a) A microchannel flowcell (b) parts.....	42
3.4	A QCM with flow injection system.....	43
3.5	Schematic diagram of coating layers on quartz crystal.....	44
3.6	EDC and NHS coupling reaction.....	45
3.7	Magnetron sputtering system.....	52
3.8	Anodizing Aluminum Oxide (AAO) template.....	54
3.9	(a) Raman spectrometer system in the experiment before testing and (b) after exciting laser.....	55

<b>FIGURE</b>	<b>PAGE</b>
4.1 SEM images show surface morphologies of (a) uncoated and (b) PVC-COOH coated quartz surfaces.....	58
4.2 Hydrophilic property images of (a) 10 seconds (b) 20 seconds and (c) 30 seconds of coating time.....	59
4.3 AFM images show surface morphologies of (a) 10 seconds (b) 20 seconds and (c) 30 seconds of coating time.....	62
4.4 Frequency response of modified QCM sensor under continuous flow system at multiple flow rate steps.....	63
4.5 Frequency response of reusability steps of QCM sensor under flow system at flow rate 50 $\mu$ L/min (a) flow 0.1 M NaOH (b) rinse PBS buffer and (c) add antibody.....	65
4.6 Frequency response of modified QCM sensor under continuous flow system at multiple immobilization steps (a) introducing PBS flow (b) EDC/NHS adsorption, (c) Protein G coating, (d) cTnT Ab coating, (e) Casine blocking reagent coating (f) Ab-Ag complex and (g) PBS rinse (h) steady-state level of 50 ng/mL cTnT detection.....	66
4.7 QCM frequency shift of the modified QCM sensor as function of cTnT concentration in the log scale.....	69
4.8 Cross-sectional TEM images of the SERS substrates with the silver nanoparticles deposited by the magnetron sputtering for 8 seconds on AAO template.....	75
4.9 (a) SEM images of the surface topology of the anodized aluminum before etching.....	76

<b>FIGURE</b>	<b>PAGE</b>
4.9 (b) SEM images of the surface topology of the anodized aluminum after 30 minutes of H <sub>3</sub> PO <sub>4</sub> etching.....	77
4.10 SEM images of the surface topology of the SERS substrates with the silver nanoparticles deposited on the AAO template for (a) 8 seconds, and (b) 16 seconds.....	79
4.11 Schematic of the silver nanoparticles deposited on the AAO template previously fabricated on top of the silicon wafer.....	80
4.12 SEM images of the surface topology of the substrates with the silver nanoparticles deposited on the blank silicon wafers for (a) 8 seconds, and (b) 16 seconds.....	81
4.13 Raman spectra of dried methylene blue droplets on several types of the sample surfaces: (a) blank silicon surface, (b) blank AAO template on Si, (c) 16 seconds silver nanoparticles deposited on Si, (d) 8 seconds silver nanoparticles deposited on Si, (e) 16 seconds silver nanoparticles deposited on AAO template, and (f) 8 seconds silver nanoparticles deposited on AAO template.....	83
4.14 Raman spectrum of dried droplets of a solution of $1 \times 10^{-3}$ M pyridine and $5 \times 10^{-2}$ M HCl on the SERS substrate with 8 seconds silver nanoparticles deposited on the AAO template. The bottom spectrum indicates Raman intensity on blank Si surface.....	85
4.15 Illustration of the Developed SERS substrates.....	90

<b>FIGURE</b>	<b>PAGE</b>
4.16 Raman spectra of the cTnT droplets at the concentration of 50 ng/mL as left dried on (a) the Si substrate, and (b) the silver nanoparticles deposited on the AAO template.....	91
4.17 Raman spectra of the cTnT droplets at the concentration of 5 μg/mL as left dried on the silver nanoparticles deposited on the Si substrate at (a) partially dried, and (b) completely dried.....	92
4.18 Raman spectra of Buffer and cTnT with the concentrations varied from $5 \times 10^{-6}$ g/mL to $5 \times 10^{-9}$ g/mL on the fabricated SERS substrate...	94

## LIST OF ABBREVIATIONS AND SYMBOLS

Å	Armstrong
kDa	Kilo Dalton
Pa	Pascal
µg	Microgram
ng	Nanogram
nm	Nanometer
RH	Relative Humidity
EWG	The Expert Working Group
CK-MB	Creatinine Kinase – Muscle, Brain
cTnI	Cardiac troponin I
cTnC	Cardiac troponin C
cTnT	Cardiac troponinT
MB	Myoglobin
LDH	Lactase dehydrogenase
MLC	Myosin Light Chain
MHC	Myosin Heavy Chain
hFABP	Heart type Fatty Acid Binding Protein
Eno	Enolase
CRP	C-reactive protein
sccm	Standard Cubic Centrimeters per Minute
HV DC system	High Vacuum Magnetron Sputtering system
FT Spectrometers	Fourier Transform Spectrometers
S/N	Signal to Noise Ratio
Nd:YAG lasers	Neodymium-doped yttrium aluminium garnet/ Nd:Y <sub>3</sub> Al <sub>5</sub> O <sub>12</sub> lasers
Ar <sup>+</sup> ion lasers	Argon ion lasers



HeNe lasers	Helium-Neon lasers
3D crystal structure	Three dimension crystal structure
RF power	Radio Frequency Power
Al	Aluminum
Ag	Silver
Ca	Calcium
Mg	Magnesium
-NH <sub>2</sub>	Amide Group
-COOH	Carboxylic Group
SAM	Self Assembly Monolayer
PDMS	poly(dimethylsiloxane)
PVC	Polyvinyl Chloride

# CHAPTER I

## INTRODUCTION

### 1.1 Introduction

Cardiac Troponin complex is an important marker that has recently supplanted creatine kinase (CK), M (muscle) B (brain) as the analyses choice of acute myocardial infarction (AMI) diagnosis [1-9]. Cardiac Troponin T (cTnT) is one of the three proteins of the troponin complex [4, 7, 10-15], which mediates the calcium-activity elevated in patients with AMI, and recognized by World Health Organization (WHO) diagnostic criteria [1]. Multiple studies have demonstrated that cTnT is an important prognostic indicator in patients presenting chest pain, even when CK-MB fraction is not elevated [2, 6, 9, 14, 16-22]. Several methods have been used to detect cTnT [20, 23], such as Enzyme linked immunosorbant assay (ELISA) [24-25] or Radioimmunoassay (RIA) [26-27], and have now become standard analytical methods [28, 29]. Nonetheless, they suffer from a relatively slow process, a highly reagent consumption and a complicate procedure. In addition, these methods require an expensive analyzer system for a high sensitivity detection since the elevated cTnT concentration collected from a patient with heart damage could be as low as 5 ng/mL. These have hindered cTnT measurement from a daily clinical diagnostic.

Among the advances in biosensor technology is the development in protein detection. Two methods for cTnT detection which are Quartz Crystal Microbalance (QCM) and Surface - Enhanced Raman Spectroscopy (SERS) are selected. These

methods have made the advance technique for cTnT detection using two different nanotechnologies. Moreover, these methods could work well for detection of a low cTnT concentration level.

## **1.2 Objectives of the research**

There are two targets for this dissertation.

1. To develop a new Quartz Crystal Microbalance biosensor using polymer coated surface, combining with specificity of antibodies for cTnT detection.
2. To fabricate a novel Surface-Enhanced Raman spectroscopy substrate using magnetron sputtering by depositing Silver nanoparticles on AAO template for analysis of cTnT spectrum and calculation of Raman enhancement factor.

## **1.3 Scope of the research**

As a starting point, several important aspects of developing cTnT sensors are described in Chapter II. The physical and chemical properties of cTnT will be discussed. Then, a modified QCM biosensor, which has a high sensitivity and a specificity of the cTnT detection method, combined with Antigen – Antibody reaction and QCM by piezoelectric technique in which nanotechnology used is firstly described. The past developed quartz crystal biosensor is described. Many of researches in quartz crystal are allowed the sensor to be detected biomolecules such as Protein, Bacterial cells and Hormones. The significant parameters for improve surface of quartz crystal such as surface modifying, flow rate controlling, binding process will be analyzed. Following, the principles of SERS substrate for cTnT detection will be described. The fabrications of SERS, instrument and its applications

trend are investigated. The significant structure of cTnT is studied by observing the vibrational spectrum of molecules. Then, the use of SERS experiments to enhance Raman spectrum of cTnT molecules will be described.

In Chapter III, the use of Carboxylic polyvinyl chloride (PVC-COOH) in polymer film fabrication to improve the quartz crystal surface roughness for immobilization of protein and antibody is explained. The effect of the polymer coating has been investigated using several methods. Field emission scanning electron microscope (FE-SEM) is used to observe the roughness of overall surface. Atomic force microscopy (AFM) reveals how the polymer fabrication modifies the surface morphology and increases branches of carboxylic group. The continuous flow QCM sensor system is used in cTnT detection experiments. Latterly, the technique of cTnT detection by a surface enhanced Raman spectroscopy (SERS) method in combination with developed SERS substrate is also described. The fabrication process using thin film technology is described. A technique for verifying characteristics of SERS substrate has also reported by introducing Methylene Blue (MB) as a probe molecule. Pyridine is used for confirming the sensitivity of SERS substrate and finally cTnT is used for detecting experiment.

In Chapter IV, the results from two types of cTnT detection methods, QCM and SERS are described. First, the experimental results from two types of surface morphology on quartz crystals, uncoated and coated are described. The uncoated quartz crystal is studied on commercial quartz, which rinsed with methanol, preparing a clean quartz crystal surface. The coated quartz crystal surface is initiated with polymer (PVC-COOH) coating, which has a long chain of polymer and covalent

bonds with carboxylic groups. To investigate the polymer film morphologies on quartz crystal, SEM images are used to observe uncoated and coated quartz crystal with 200 nm thick PVC-COOH. For uncoated surface, which cannot immobilize protein, is compared its SEM image with coated surface. To study the stability of the polymer film under PBS flow, the result of both coated and uncoated quartz crystals under various flow rates is investigated. The results indicate that the negative frequency shift was almost linearly proportional to the flow rate due to increasing in mass loading from the fluid pressures. To measure the quantity of cTnT levels in standard cTnT samples, the varied concentrations by the conversion of electrical signal processing have been reported. The frequency shifts are found to be proportional to the cTnT concentration and can conclude that our system can detect diluted cTnT down to the detection limit at the concentration of 5 ng/mL without interference. For SERS experiments, the SERS substrates, which are fabricated by magnetron sputtering and then deposited with silver nanoparticles by anodization is described. The SEM and TEM images use to observe the porous of surface morphology of the substrates. The MB and Pyridine, which have definitely concentrations, are used as reference samples. For calculation of enhancement factors, which can be observed with MB spectrum, the band positions has been proposed to previous published results. To qualify the sensitivity of the substrate, the SERS spectrum of Pyridine has been reported. For cTnT detection, the spectrum spectra are studied with varied cTnT concentrations compared with background spectrum of Phosphate buffer. The result shows that cTnT band peaks can be clearly observed and some of vibrational peaks can still be able to detect at an ultra low concentration.

Finally, the conclusions of this dissertation are summarized and discussed the future prospect of cTnT antibody immobilization on polymer coated quartz crystal surface as well as cTnT detection by SERS substrate in Chapter V.

## **CHAPTER II**

### **THEORY AND LITERATURE SURVEY**

Cardiac troponins are part of the new definition of acute myocardial infarction (AMI) by the European Society of Cardiology and the American College of Cardiology (ESC/ACC). They are released into the blood circulation from injured heart muscle cells [1, 6, 9] during cardiac ischemia which is distinguishable from skeletal muscle troponins under normal conditions [2, 7-8, 11-14, 16, 29]. Multiple studies have demonstrated that both Cardiac Troponin I (cTnI) and Cardiac Troponin T (cTnT) are important prognostic indicators in patients presenting chest pain, even when Muscle-Brain (MB) fraction of Creatine Kinase (CK) is not elevated [3, 9]. Particularly, the cTnT is widely accepted as a tool to stratify patients with chest pain. Moreover the detection of Cardiac Troponin might also be useful prognosticator in high risk patients [4-23]. There are several methods being able to detect the cTnT such as Enzyme-Linked Immunosorbent Assay (ELISA) [24-25], Radioimmunoassay (RIA) [26-27]. These methods are normally used even though they are suffered from relatively low throughput, high reagent and sample consumption. Approach for cTnT detection which has more potential to be truly direct measurements, as well as rapid, specific and user-friendly should be explored.

## 2.1 Cardiovascular Biomarker

The diagnosis of acute myocardial infarction depends upon the patient's clinical history, the interpretation of the electrocardiogram (ECG) and measurement of serum levels of cardiac enzymes [22-23, 28]. Diagnostic uncertainty frequently arises because of a variety of factors. Many patients with acute myocardial infarction have atypical symptoms, and one half of patients with typical symptoms do not have acute myocardial infarction. One half of patients with acute myocardial infarction have non-diagnostic ECG, and some patients are unable to provide a history. Biochemical markers of cardiac injury are therefore commonly relied upon to diagnose or exclude acute myocardial infarction. Serum markers in current clinical use which are included with the MB isoenzyme of CK-MB, myoglobin, cTnT and cTnI are shown in Table 2.1. These various proteins are released from myocardial cells after an insult, such as ischemia or infarct, and can be detected in the serum within hours of myocardial injury. Currently CK-MB is the serum cardiac marker relied upon as the diagnostic reference standard for acute myocardial infarction [28].

The diagnostic utility of CK-MB is limited, however, because it lacks specificity for myocardial injury (rendering false-positive results). Also, CK-MB might fail to rise to abnormal levels in all patients with acute myocardial infarction, rendering false-negative results. The relatively brief duration of CK-MB elevation following acute myocardial infarction limits its value as a cardiac marker in patients who have delayed symptoms. The popular marker is cTnT will be used in utility and clinical application and discussed in regard to evaluating patients with chest pain.



**Table 2.1** Biomarkers used or proposed for use in the clinical diagnosis of AMI.

<b>Biomarker</b>	<b>Molecular Weight (Daltons)</b>	<b>Initial Elevation (Hours)</b>	<b>Peak Elevation (Days)</b>	<b>Time to return to baseline (Days)</b>
CK-MB	86,000	3–12	1	2–3
Cardiac troponin I	22,000	3–12	1	5–10
Cardiac troponinT	37,000	3–12	0.5–2	5–14
Myoglobin	17,800	1–4	0.5–0.6	1
LDH	135,000	10	1–2	10–14
MLC	19,000–27,000	6–12	2–4	6–12
MHC	400,000	48	5–6	14
hFABP	14,000–15, 000	1.5	0.4–0.9	1
Enolase	90,000	6–10	1	2

## 2.2 Rationale for Choosing the Troponins

A number of molecules have been employed to assess and/or predict cardiac toxicity resulting from chemical (drug or environmental) exposures as well as in response to various pathogenic processes, such as ischemia and congestive heart failure. As reviewed in this document, there are various forms of cardiac injury, each with its own characteristics of detection and predictivity. The objective of the Expert Working Group (EWG) is to identify useful biomarkers of each form of cardiac injury, both by reviewing evidence in the published literature and possibly by

proposing additional validation studies. The first form of drug-induced cardiac injury can be investigated by the EWG which is most commonly monitored in both preclinical and clinical studies such as cardiomyocyte integrity or cytolysis, wherein contents of the damaged cardiac muscle cell are released to the extracellular space and are detected in the circulating blood. Although a number of such markers have been used and are frequently incorporated into routine diagnostic protocols, validation studies reveal several shortcomings with these historical markers. Many of these are delineated in the preceding paragraphs. A significant advance in the field of biomarkers of cardiac injury has been the emergence from the clinical literature of the Cardiac Troponins as meaningful indices of myocardial infarction and related disorders. This clinical experience has recently been addressed by the Joint European Society of Cardiology in conjunction with the American College of Cardiology in a consensus document promoting the use of the Troponins as reliable indicators of AMI in humans. Joint discussions between the European and American cardiology societies have produced recommendations that there should be a redefinition of AMI with Cardiac Troponin measurement becoming the new “Gold Standard” for diagnosis. Cardiac Troponin is highlighted as the preferred biomarker given its nearly absolute myocardial tissue specificity, as well as high sensitivity, and capability to reflect microscopic zones of myocardial necrosis [22]. The recent acceptance by the clinical community of the Troponins as the biomarker of choice for assessing myocardial damage in humans highlighted the need to evaluate the utility of this biomarker for preclinical drug development and clinical drug-monitoring applications.

### 2.2.1 Biology of the Troponins

The sarcomere is the basic structural and functional unit of the myocardial cell. Each sarcomere is comprised of interdigitating thick and thin filaments that present a striated appearance via light microscopy, which is similar to that of skeletal muscle [2]. The thick filaments account for 60–70% of the total muscle cell protein and are composed primarily of myosin. Actin is the main constituent of the thin filaments. The actin proteins are threadlike structures composed of a double helical formation of G-actin monomers that extend from the Z bands (structures that separate sarcomeres) toward the center of the myosin. The smallest structural element of the thin filament is 7 actin monomers associated with a single tropomyosin-troponin complex [3]. The tropomyosin-troponin complex is located periodically along the actin thin filament strands at intervals of 3,850 nm within the sarcomeres of all types of striated muscles (fast twitch, slow twitch, and cardiac) but not smooth muscle, where calmodulin regulates contraction [4-7]. It is the interaction between the actin and myosin filaments that is the basis for striated muscle contraction [8]. The contractile process is controlled by tropomyosin and the troponin complex. Tropomyosin is a rigid rod-shaped protein (66 kDa) that lies in the long pitched grooves on either side of the actin filament. It is thought that at low calcium concentrations, tropomyosin sterically prevents the interaction of actin with myosin. The tropomyosin molecules shift their positions slightly when calcium concentrations are increased, which allows for the interaction of myosin and actin to produce the contractile response [9].

### 2.2.2 Characteristics of the Troponin Complex

The characteristics of the Troponin complex were elaborated when the purified form was separated into 3 distinct polypeptide proteins by SDS gel electrophoresis [10]. Based on functional properties, these subunit proteins were referred to as Troponin T (TnT is 37 kDa), troponin I (TnI is 22 kDa), and troponin C (TnC is 17 kDa) [11]. The troponin complex is about 2,650 nm long with a globular region that has a diameter of approximately 1,000 nm and an extended, rod like tail about 1,600 nm in length and 200 nm in width [5]. The globular head is made up of dumbbell-shaped TnC, globular TnI, and the carboxy-terminal portion of TnT. The rod like tail consists of the amino-terminal portion of TnT. The complex is located at 40-nm intervals along the tropomyosin peptide. In the figure 2.1, the troponin complex controls muscle contraction by suppressing the interaction between actin and myosin [4]. The inhibitory component within the troponin complex is the basic globular protein TnI, which in the absence of calcium binds to actin and tropomyosin to inhibit actinomyosin  $Mg^{+2}$  ATPase [14]. Once depolarization of the cell membrane (sarcolemma) occurs, calcium is released from the sarcoplasmic reticulum into the cytosol. Calcium binding to TnC changes the configuration of the tropomyosin/troponin complex causing TnI to dissociate from the myosin binding sites on the actin-tropomyosin complex. This action reduces inhibition of the myosin/actin interaction and thereby facilitates muscle contraction [14-15]. Troponin T is an asymmetric protein that serves to attach the troponin complex to tropomyosin. It is also thought to act as a complex signal amplifier, transmitting the inhibitory effect of TnI in the absence of calcium, attenuating the inhibition in the presence of calcium, and stimulating actinomyosin Mg-ATPase activity [13-14].

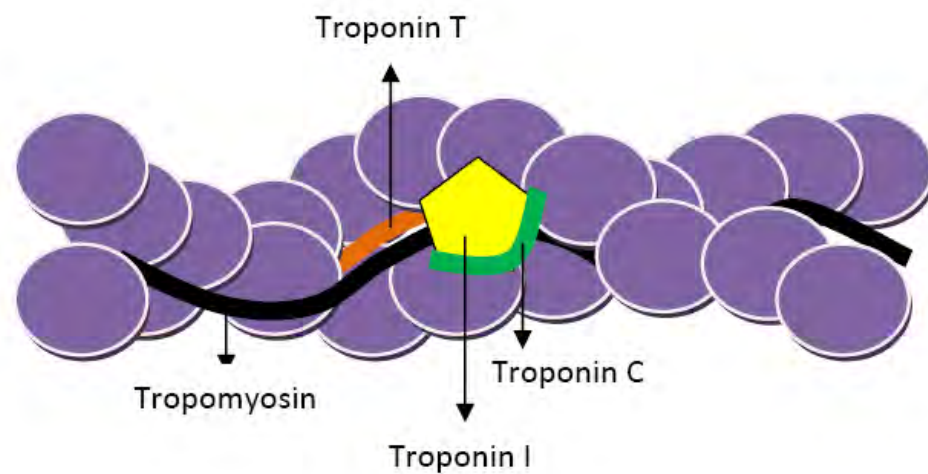


**Figure 2.1** The characteristics of the Troponin complex.

## 2.2.3 Active Sites

### 2.2.3.1 Troponin T

The globular head of the troponin complex includes the carboxy-terminal domain of TnT. This region contains binding sites for TnC, TnI, and the midsection of tropomyosin [13]. The rodlike tail of the troponin complex includes the amino-terminal portion of TnT. This site is thought to promote the head-to-tail polymerization of tropomyosin. Phosphorylation of the TnT aminoterminal serine residue may play a role in the regulation of actinomyosin  $Mg^{+2}$  ATPase activity [13].

### 2.2.3.2 Troponin I

Troponin I binds to actin, tropomyosin, TnT and TnC (2 binding sites) [13]. The strength of the interaction between TnI and TnC depends on the degree of saturation of the TnC binding sites for  $Ca^{+2}$ . There are multiple sites for phosphorylation of TnI, which serves an important role in regulating calcium

sensitivity and actinomysin ATPase activity [16-17]. A cAMP-dependent protein kinase (protein kinase A) and  $\text{Ca}^{+2}$ -phospholipid dependent protein kinase (protein kinase C) facilitate phosphorylation of the various TnI sites [18]. When protein kinase A phosphorylates serines 23 and 24 of cTnI, the  $\text{Ca}^{+2}$  sensitivity of troponin-regulated actinomysin  $\text{Mg}^{+2}$  ATPase is reduced [19].

### **2.2.3.3 Troponin C**

Troponin C is a dumbbell-shaped protein that forms part of the head region of the troponin complex. Two sites located on the C-terminal domain bind both  $\text{Ca}^{+2}$  and  $\text{Mg}^{+2}$ , but two N-terminal sites are specific for  $\text{Ca}^{+2}$  binding only [11]. The binding of calcium to TnC causes a conformational change leading to enhance affinity for TnI. This effect attenuates inhibition by causing cTnI to move away from actin-tropomyosin binding sites [13-14]. The structures of cardiac and skeletal TnC are identical, which prevents use of TnC as a specific marker of cardiac injury [20].

## **2.3 Biomarker characteristics of the Troponins**

### **2.3.1 Specificity**

The isoform expression patterns of TnT and TnI differ in cardiac, fast twitch, and slow twitch skeletal muscle. Different genes encode these isoforms with the cardiac isoforms having unique amino acid compositions and structures [20]. The cardiac form of Troponin I differs from the form found in skeletal muscle by an additional 31 amino acid sequence at its N-terminus. Antibodies specific to this N-terminal segment of cTnI provide a convenient and effective means to distinguish the

cardiac form from the skeletal form in immunoassays. Immunoreactive cTnI is localized exclusively in the heart and is not known to be expressed in skeletal muscle or any other tissue, even in diseased states. While cTnT isoforms are expressed in injured skeletal muscle, they cannot be detected by the current diagnostic assays. The detection of serum TnT during renal failure by the first generation cTnT assays in the absence of a detectable rise in the kidney expression of cTnI is attributed to lack of specificity of the anti-cTnT antibodies used at that time [23]. Where detection in the serum of cTnT in end stage, renal failure has been demonstrated with the current generation of cTnT immunoassays, it is suggested that this is indicative of myocardial damage that occurs secondary to the hemodynamic changes associated with kidney failure. This observation raises the important point that drug-induced cardiac damage may not necessarily reflect a direct action of the drug on the heart. Cardiovascular homeostasis is a complex and highly regulated process and there are numerous systems that influence cardiac function, including vascular volume and pressure, kidney and liver function, as well as neuroendocrine changes. Accordingly, while an increase in serum cTnI or cTnT may be an accurate reflection of damage to the myocardial tissues, the specific cause of that injury may require more extensive investigation.

### **2.3.2 Sensitivity**

The methods currently available to measure serum Cardiac Troponin concentrations have recently been reviewed [20]. The background concentration of cTnT and cTnI in serum is effectively undetectable. For cTnI assay methods, functional sensitivity of the assays ranges from 0.02  $\mu\text{g/mL}$  to 0.45  $\mu\text{g/mL}$  with linear

ranges up to 20 or 247  $\mu\text{g}/\text{mL}$ . For cTnT, the functional sensitivity of the electrochemiluminescent immunoassay is 0.01  $\text{ng}/\text{mL}$  with a linear range up to 2-5  $\mu\text{g}/\text{mL}$ . On the basis of current data it is reasonable to expect the methods to give extremely low or undetectable cTnT values in healthy people.

Troponin is a component of thin filaments (along with actin and tropomyosin), and is the protein to which calcium binds to accomplish this regulation. Cardiac and skeletal muscles are controlled by changes in the intracellular calcium concentration. When calcium concentration rises, the muscles contract, and when calcium concentration falls the muscles relax.

#### **2.4 Enzyme Linked Immunosorbant Assay method (ELISA)**

In 1971, Peter Perlmann and Eva Engvall at Stockholm University in Sweden, and Anton Schuurs and Bauke van Weemen in The Netherlands [25], independently published papers which synthesized the knowledge into methods to perform EIA/ELISA. ELISA is a biochemical technique which is used mainly in immunology to detect the presence of an antibody or an antigen in a sample. The ELISA has been used as a diagnostic tool in medicine and plant pathology, as well as a quality control check in various industries. In figure 2.2(a), an unknown amount of antigen is affixed to a surface figure 2.2(b), and from figure 2.2(c), 2.2(d) then a specific antibody is washed over the surface so that it can bind to the antigen. From figure 2.2(e), the antibody is linked to an enzyme. Figure 2.2(f), 2.2(g) and 2.2(h) are shown the final step which a substance is added and the enzyme can convert to some detectable signal. Thus in the case of fluorescence ELISA, when light of the appropriate



wavelength is shown upon the sample, any antigen/antibody complexes will fluoresce so that the amount of antigen in the sample can be inferred through the magnitude of the fluorescence.

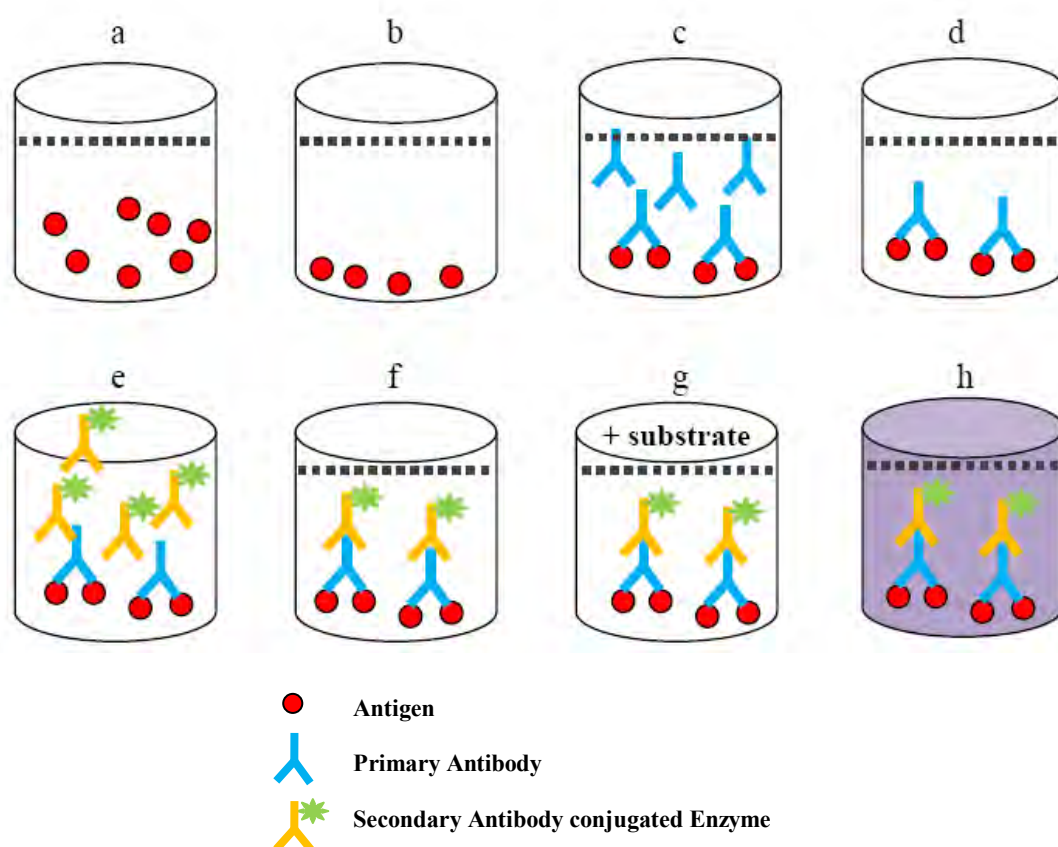


**Figure 2.2** ELISA Method.

Performing an ELISA involves at least one antibody with specificity for a particular antigen. The sample with an unknown amount of antigen is immobilized on a solid support (usually a polystyrene microtiter plate) either non-specifically (via adsorption to the surface) or specifically (via capture by another antibody specific to the same antigen, in a "sandwich" ELISA). After the antigen is immobilized the detection antibody is added, forming a complex with the antigen. The detection

antibody can be covalently linked to an enzyme, or can itself be detected by a secondary antibody which is linked to an enzyme through bioconjugation. Between each step the plate is typically washed with a mild detergent solution to remove any proteins or antibodies that are not specifically bound.

After the final wash step the plate is developed by adding an enzymatic substrate to produce a visible signal, which indicates the quantity of antigen in the sample. Older ELISAs utilize chromogenic substrates, though newer assays employ fluorogenic substrates enabling much higher sensitivity.

## **2.5 Theory of Quartz Crystal Microbalance (QCM)**

A QCM measures a mass per unit area by measuring the change in frequency of a quartz crystal resonator. The resonance is disturbed by the addition or removal of a small mass due to oxide growth/decay or film deposition at the surface of the acoustic resonator. The QCM can be used under vacuum, in gas phase and more recently in liquid environments. It is useful for monitoring the rate of deposition in thin film deposition systems under vacuum. In liquid, it is highly effective at determining the affinity of molecules (proteins, in particular) to surfaces functionalized with recognition sites. QCM has also been used to investigate interactions between biomolecules. Frequency measurements are easily made to high precision (discussed below). In addition to measuring the frequency, the dissipation is often measured to help analysis. The dissipation is a parameter quantifying the damping in the system, and is related to the sample's viscoelastic properties.

The relation between frequency shift of the quartz resonator and polymer in gas phase has been derived by Sauerbrey in 1959 (see equation 2.1). This relation is written as followed equation:

$$\Delta f = -\frac{2f_0^2}{\sqrt{\rho_q \mu_q}} \frac{\Delta M}{A} \quad (2.1)$$

Where  $\Delta f$  is the frequency shift of the resonator,  $f_0$  is the fundamental frequency,  $\rho_q$  is the density of quartz (2.648 g/cm<sup>3</sup>),  $\mu_q$  is the shear modulus of quartz (2.947 x 10<sup>11</sup> g/cm<sup>3</sup>),  $\Delta M$  is the mass deposited on the surface of electrode and  $A$  is piezoelectrically active area (for the  $2/(\rho_q \mu_q)$  can be expressed as a constant,  $k$  which is 2.26 x 10<sup>-7</sup>). Traditionally, the Sauerbrey's equation was developed for oscillation in the air and only applied to rigid masses attached to the crystal.

Quartz crystals are the most common type of single crystal materials used in analytical application due to their electrical, mechanical and chemical properties [30]. The resonant frequency of the quartz crystal depends on several parameters, for instance the size, the density, the shear modulus and also the cut. Quartz crystals have to be cut in a specific orientation with respect to the crystal axes. As represented in Figure 2.3, the quartz crystal cuts used belong to the Y-cut family and therefore the AT- and BT- cuts are the most important for commercial applications from International Crystal Manufacturing, 2006. The AT-cut which refers to a cut at +35<sup>1</sup>/<sub>4</sub>° angle is the mostly used quartz crystal for the majority of piezoelectric analytical chemistry applications. As shown in Figure 2.3, Piezoelectric Quartz

Crystal (PQC) is sliced wafers whereas the PQC is covered by the two electrodes. The electrodes are in general made of silver or gold as shown in Figure 2.4 and are produced by thermal evaporation onto the surface of the quartz crystal. Thereby, only the region between the electrodes or the seed is piezoelectric active and consequently the greatest sensitivity is in the centre of the crystal.

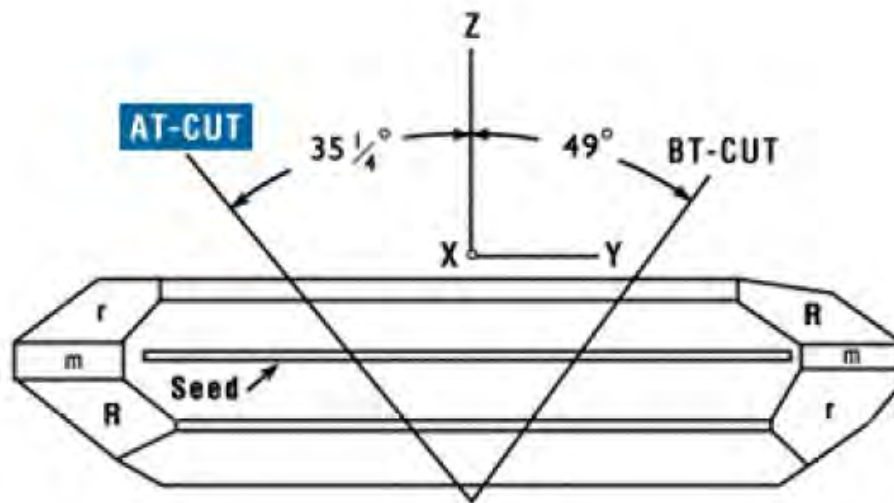


**Figure 2.3** Schematic of AT cut quartz crystal surface.

This research requires that the detector detect the change in frequency due to complex binding. It has been shown that quartz crystal microbalance measurements can be performed in liquid, in which case the viscosity-related reduction in resonant frequency will be observed as equation 2.2.

$$\Delta f = -f_u^{3/2} \sqrt{\frac{\eta_l \rho_l}{\pi \rho_q \mu_q}} \quad (2.2)$$

Where  $\Delta f$  = measured frequency shift,  $f_u$  = resonant frequency of the unloaded crystal,  $\rho_l$  = density of liquid in contact with the crystal,  $\eta_l$  = viscosity of liquid in contact with the crystal,  $\rho_q$  = density of quartz,  $2.648 \text{ g/cm}^3$ ,  $\mu_q$  = shear modulus of quartz,  $2.947 \times 10^{11} \text{ g/cm} \times \text{s}$ . Therefore, this equation is applied to a QCM sensor to evaluate changes in the mass of water deposited on the electrodes. This is because they are absorbed by the hygroscopic and gas sensing layer, which is rigidly deposited on the electrode surface. Figure 2.4 shows an example of Quartz crystals which surface are gold (left) and silver (right) compare with Thai baht coin.

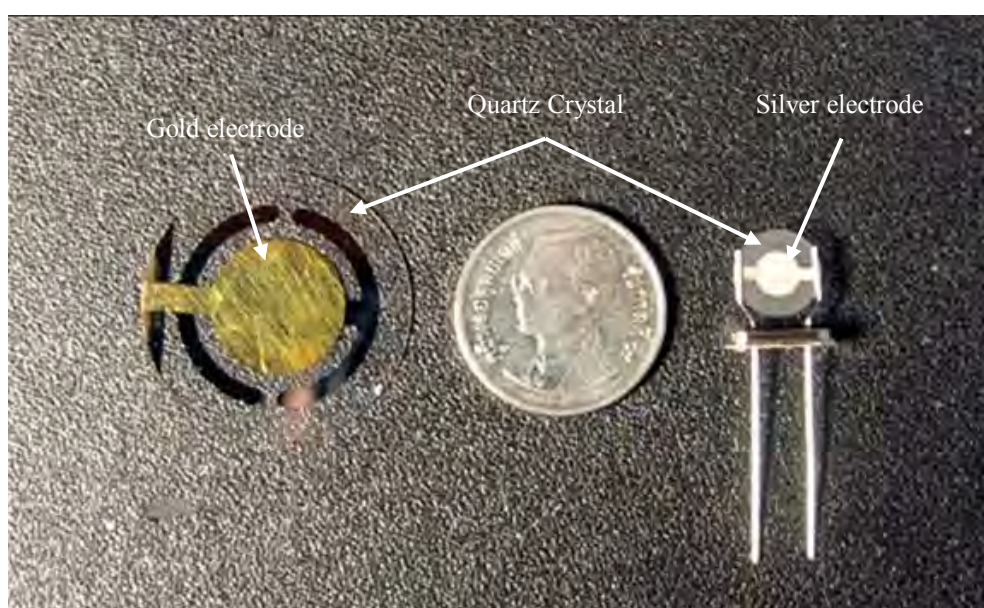


**Figure 2.4** Gold (left) and silver (right) electrode quartz crystal compare with Thai baht coin (middle).

The classical application of QCM is a thin film thickness monitoring system [31-35], in which a resonance frequency is inversely proportional to a total thickness of the thin film deposited on a quartz crystal surface. Monolayer sensitivity is easily

reached. The QCM is not only can be applied to rigid film, but also in humidity and gas sensing. Although the liquid and gas molecules deposited on the quartz surface are not rigid material, they can be immobilized by the hygroscopic and gas sensing layer, which is rigidly deposited on the electrode surface [36-39]. For applications in biosensors, a sensor can be used to detect an additive mass of a specific biomolecules by sensing an immuno-reaction on the immobilization layer of quartz surface [31].

## **2.6 Development of modified Quartz Crystal Microbalance (QCM) biosensors**

A developed Quartz Crystal Microbalance (QCM) biosensor, combining with the specificity of antibodies [30-32] with the sensitivity of the quartz crystal microbalance can provide a potentially rapid and direct measurement of cTnT concentration. The bioprobe on the silver sensor is expected to have high active region per antigen antibody reaction. The sensor is a mass sensitive detector based on an oscillating silver quartz crystal with some specific fundamental frequency [31]. Due to complex binding, crystal frequency will decrease and can be used to measure frequency change.

The QCM can provide a much simpler maneuver, relatively less expensive, and more stable than those conventional cTnT detection methods [33-45]. Surprisingly, QCM technique has been rarely reported in the study of cTnT detection. To date, there is only one demonstration of cTnT detection using this technique [45]. The use of QCM technique to detect cTnT may be a powerful parameter in AMI diagnosis, but has not been well studied.

## 2.7 Surface Enhanced Raman Scattering (SERS)

The application of Raman Spectroscopy is limited by the low scattering at cross section of the molecules and the correspondingly low intensities of their Raman bands. This situation can be substantially improved by use of so-called surface Enhanced Raman scattering. The Raman scattering of molecules adsorbed on rough metal surfaces results in a large Raman scattering enhancement, which can be explained by electromagnetic enhancement and chemical effects as shown in Figure 2.5. This large enhancement enables easy analysis of molecular monolayers at appropriate surface even 1% of a monolayer has been observed and the detection of single molecules on optimum metal particles was recently reported.

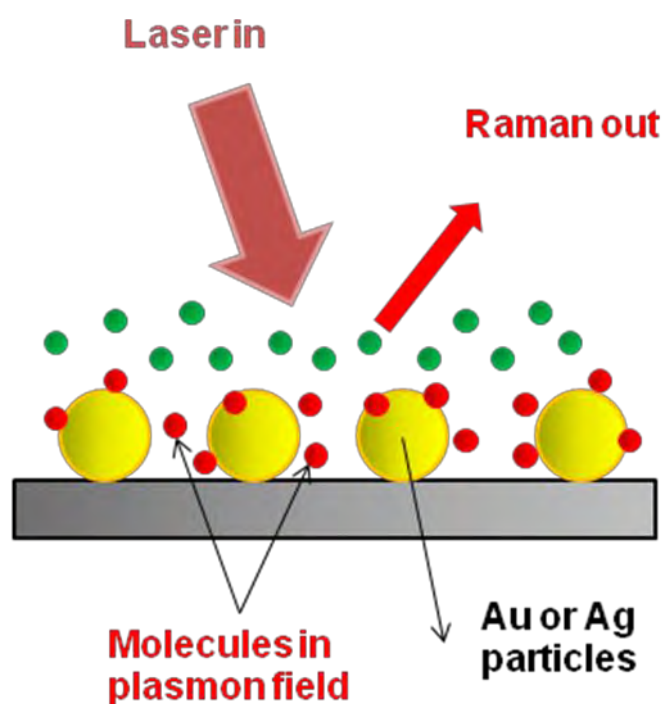


**Figure 2.5** Schematic diagram of Raman surface.

SERS is usually restricted to specially prepared “active” surfaces. A broad range of other surfaces also becomes accessible to SERS spectroscopy after special preparation techniques.

- Metal island films form spontaneously during slow evaporation of the metal onto supports with low adhesion. The metal islands can produce the surface enhancement required for Raman characterization of the surface of the support.
- Appropriate metal particles can be sputter-deposited on almost any support which can be exposed to vacuum.
- Ultrathin metallic, semiconductor, insulator, or organic overlayers can be deposited on SERS-active metal surfaces.

For overlayer thicknesses of a few atomic or molecular layers, the supporting metal can produce surface enhanced field at the surface of the overlayer. Then, composition and structure of the overlayer surface can be analyzed by SERS spectroscopy.

### **2.7.1 SERS Instrumentation**

The scattering effect was observed in 1928 by C.V. Raman, who used sunlight and complementary filters. Later, mercury vapor lamps were used for illumination of samples. Current Raman spectrometers use lasers as monochromatic light sources. Different types of laser can be used, depending on the wavelength, sensitivity, and spectral resolution required. Gas laser such as Ar<sup>+</sup> and HeNe lasers have been quite common because of their narrow, well-defined spectral lines, stability, and beam



quality. High intensity  $\text{Ar}^+$  ion lasers, in particular, are expensive to maintain, because they consume much electrical power and cooling water. Diode lasers are more convenient. Powerful diode lasers for Raman spectroscopy usually emit red wavelengths which are suitable for avoiding fluorescence and fit the sensitivity range of silicon detectors. Diode lasers must be frequency stabilized, because their emission frequency is not defined by narrow transitions. Spontaneous emission background and low intensity side-bands must, furthermore, be filtered out when diode lasers are used for high sensitivity Raman measurements. Solid state lasers emitting in the near-infrared such as Nd:YAG lasers are used in combination with Fourier-transform spectrometer.

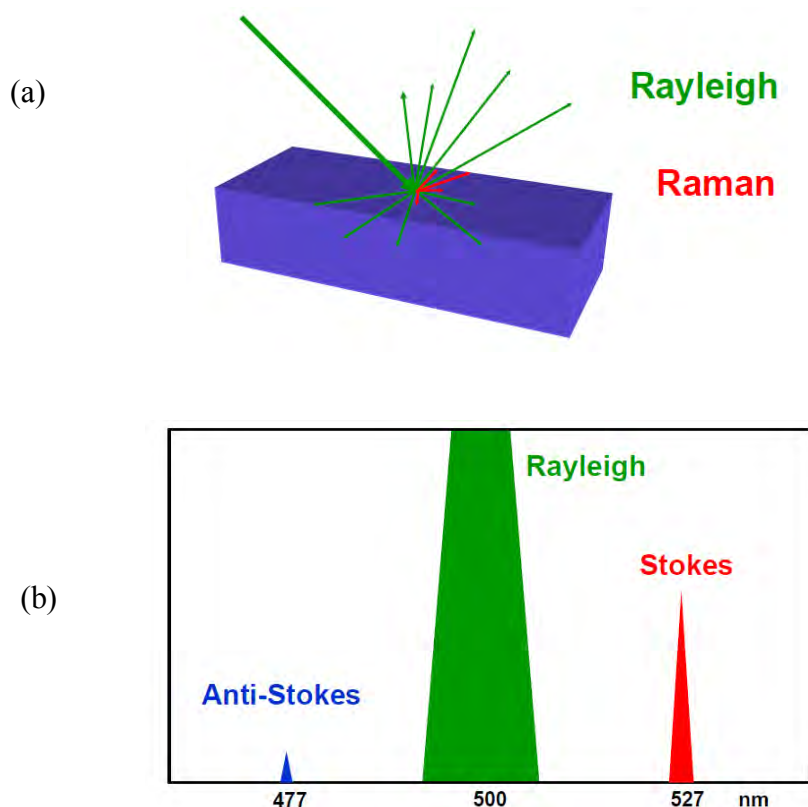


**Figure 2.6** (a) The scattering effect of Raman and (b) effect in wavelength.

Simple optics focuses the laser onto the sample and collect the Raman scattered light. In the widespread-back-scattering or  $180^\circ$  arrangement a single objective serves for both, focusing the laser and collecting the scattered light. This makes measurements easy, because only the distance between sample and objective has to be adjusted. Because transparency of the whole sample is not needed with a back-scattering arrangement, Raman spectroscopy is well suited for in-situ measurement at interface between gases, liquids, and solids with at least one transparent phase.

Elastically scattered laser light must be removed in front of spectrometer, because it is several orders of magnitude more intense than the Raman scattered radiation and would otherwise produce stray radiation at the detector shown in figure 2.6(a) and 2.6(b). Nowadays, holographic notch filters are usually used for this purpose, because of their high transmission of required wavelengths and strong suppression of unwanted wavelengths. Premonochrometers are preferable for measurements at low wavenumbers and for use of varying laser wavelengths.

Spectral analysis of the Raman scattered light is achieved by use of dispersive or Fourier-transform (FT) spectrometers. Dispersive spectrometers decompose the radiation according to its wavelength by means of a grating monochromator. FT spectrometers calculate the spectrum from an interference pattern (interferogram) produced by an interferometer with variable path-length within one of the interferometer arms. Monochromators are preferable in the visible spectral range. Compact and robust monochromators without moving parts can be used in rough environments, whereas larger high-resolution devices are mainly used in research.

In combination with array detectors, imaging monochromators can be used the multichannel advantage and thus enable large signal to noise (S/N) ratios for short measurement times. FT spectrometers also afford high S/N ratios because of their throughput advantages. The noise of their near-infrared detectors is, however, considerably larger than that of detectors operating in the visible region. Major advantages of FT spectrometers are strong suppression of fluorescence, as a result of their use of long wavelength excitation, and variable spectral resolution.

### **2.7.2 SERS application**

Because silver, gold and copper electrodes are easily activated for SERS by roughening by use of reduction-oxidation cycles, SERS has been widely applied in electrochemistry to monitor the adsorption, orientation, and reactions of molecules at those electrodes in-situ. Special cells for SERS Electrochemistry have been manufactured from chemically resistant materials and with a working electrode accessible to the laser radiation. The versatility of such a cell has been demonstrated in electrochemical reactions of corrosive, moisture-sensitive materials such as Oxyhalide electrolytes.

Langmuir-Blodgett films (LB) and self-assembles monolayer (SAM) deposited on metal surfaces have been studied by SERS spectroscopy in several investigations. For example, mono- and bilayers of phospholipids and cholesterol deposited on a rutile prism with a silver coating have been analyzed in contact with water. It can be studied that models of biological membranes which the second layer

is modified by the fluidity of the first monolayer. It is revealed the confirmation of the polar head close to silver.

SERS has also been applied as a sensitive, molecule-specific detection method in chromatography such as thin layer, liquid and gas chromatography. SERS-active colloids were deposited on the thin layer plates or mixed continuously with the liquid mobile phases. After adsorption of the analysts, characteristic spectra of the fractions were obtained and enabled unambiguous identification of very small amounts of substance.

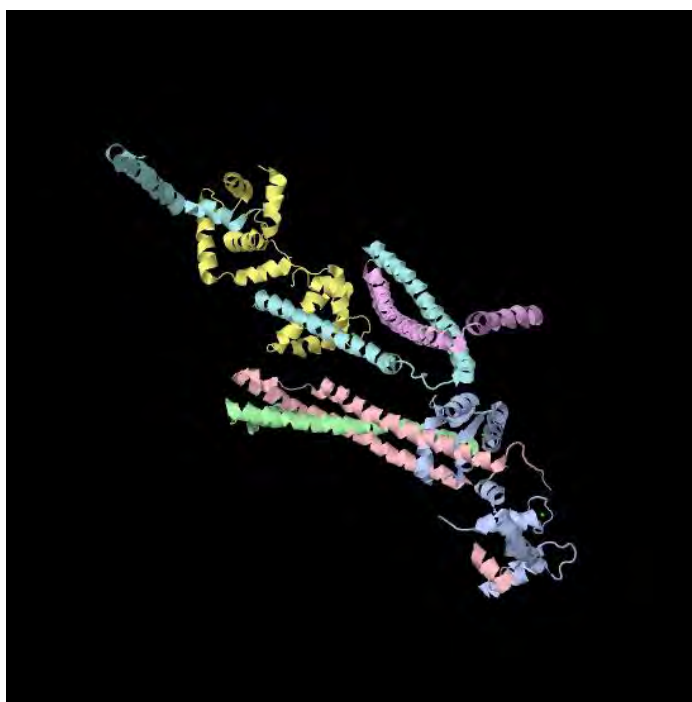


**Figure 2.7** Crystal structure of cardiac troponin complex completely saturated with  $\text{Ca}^{2+}$  [20] (PDB code 1J1D, 1J1E). The figure was produced by the Jmol program.

The figure 2.7 shows the 3D crystal structure of Cardiac Troponin latest found with Takeda et al., in year 2003 (Nature 424; 35-41). The data on the three-

dimensional structure and a detailed structure with 2.60 Å resolution is the structure of the core domain of human Cardiac Troponin in the  $\text{Ca}^{+2}$  saturated form. From the bonding, the structure with hydrogen bond shows a strong coupling between carbon and hydrogen atoms. The vibration of spectrum of molecules can change approximately 5% in Raman shift by Rayleigh scattering as shown in figure 2.6 (a). This is because the accumulated localized bonding angle in molecules affects the change in spectrum of molecules. By counting the number of intensity of Raman shift spectrum as shown in figure 2.6(b), the probability of highest intensity in SERS sample is obtained.

## **2.8 Fabrication of Surface-enhanced Raman Spectroscopy (SERS)**

The label-free detection of biomolecules such as cTnT is one of the promising field for SERS spectroscopy application. Tiniest amounts of these molecules can be absorbed by specific interactions with receptors immobilized on SERS-active surfaces [46-51]. They can then be identified by their spectra, or specific interactions can be distinguished from unspecific interactions by monitoring characteristic changes in the confirmation sensitive SERS spectra of the receptors.

Coating of metal SERS substrates with organic receptor layers such as Aluminum (Al) and Silver (Ag) makes SERS suitable for highly sensitive chemo-optical sensors for organic trace analysis in water and air [56-57]. The combination of selective adsorption the receptor with measurement of molecule-specific SERS spectra can reduce cross sensitivities considerably. SERS bands of the receptor were used as internal standards for the surface concentration of the protein compounds like

“signature”. The intensity ratios of the bonding compound such as C-C, amide (-NH<sub>2</sub>) and C-H gave a measure of the concentration of the solution of the protein compounds with a dynamic range of two orders of magnitude.

## **2.9 Previous works from other groups**

There had been few published reports of protein based QCM and fabrication technology of quartz crystal surface. Other study was studying of Cardiac Troponin [23-29] which effect to cardiovascular disease and effect of other biomarker such as Myoglobin and CK-MB. As well as study in attenuation of the QCM oscillation by the liquid leads to a broadening of the resonance frequency which could be found the protein multilayers formed by successive incubations with a biotin-albumin conjugate and streptavidin [36-40]. Designing which could evaluate the efficiency of a newly developed Troponin T enzyme immunoassay for the detection of acute myocardial infarction was also studied [6-7].

In general, improvement of quartz crystal surface was a limiting factor in QCM system. For frequency of oscillation, the thickness at which the roughness started developing the change in frequency. As mass was deposited on the surface of the crystal, the thickness increased mean consequently the frequency of oscillation which was decreased from the initial value. It was important to obtain an appropriate immobilization approach to ensure high sensitivity and stability responses in practical QCM applications. In general, physical immobilization or chemical approaches such as, chemisorption based self assembly monolayer (SAM), Polymerization by electrochemical method and Polymer coating were employed to insolubilize protein

on QCM surface [32-36, 38]. Although these approaches were commonly adopted in the processing of a QCM electrode. The most of them were required complex procedures that became laborious in case of QCM mass production. Therefore, developing a simple and convenient way to carry out the protein immobilization on QCM surface, with large-scale production potential, while maintaining its activity for detection, was interesting.

After it was found out that an excessive viscous loading would not prohibit use of the QCM in liquids and that the response of the QCM was still extremely sensitive to mass changes at the solid-liquid QCM had been used in direct contact with liquids and/or visco-elastic films to assess changes in mass and visco-elastic properties. Even in air or vacuum, where the damping of layers had been considered to be negligible or small the QCM had been used to probe dissipative processes on the quartz crystal. This was especially true for soft condensed matters such as thick polymer layers deposited on the quartz surface.

The developments of the surface modification techniques had been widely studied [11, 15-16, 21, 29]. In this technique, the quartz crystal microbalance (QCM) sensor was coated with selected polymer that adsorbs the proteins and other biomolecules through an immobilization process. Because of the difference in physical properties of each polymer, choice of polymers and fabrication method were critical factors in enhancing an amount of the absorbed molecules on quartz crystal surface [7, 18, 20, 26, 30]. Observing the results of coating could be seen the increasing of surface roughness which could enhance the sensitivity of binding reaction of protein. Then, it could motivate the immuno-reaction and accumulate the

loading mass from conjugated protein into frequency shift data. By modifying the quartz crystal surface, the process significantly induced the binding complex while maintaining high detection sensitivity.

A piezoelectric immunosensor was described which consisted of a gold filmed quartz crystal, which surface was modified with a thin nafion layer entrapping known amounts of the specific antibody [41]. The layer was applied by droplet evaporation on the gold surface of a mixture prepared by mixing a stock ethanol solution of nafion with a stock antibody suspension in aqueous phosphate buffer. The coatings thus obtained could be easily and quickly removed by simple soaking in ethanol in an ultrasonic bath and renewed by repeating the procedure above, which resulted in quite reproducible coatings.

A microfluidic analysis system [42-44] and electrochemical impedance spectroscopy [45] based on mass sensitive detection which was used with a poly(dimethylsiloxane) (PDMS) were also reported. It consisted of a miniaturized quartz crystal microbalance (QCM) and a flow cell made of PDMS which was bonded to the quartz substrate. Protein A was used for the immobilization and the functionality of this undercoating was tested by accumulation of anti-protein A and anti-C-reactive protein (CRP) antibody [44]. The sensor system was operated in a flow-through mode and the results were compared with measurements using an injection method, where a definite amount of solution was injected into a reservoir mounted on the QCM. The conducted measurements provided the excellent performance of the new flow system.



For Raman spectroscopy, which was based on an inelastic scattering of photons, had been used to identify a wide variety of chemical and biological molecules by their Raman spectra. However, a conventional Raman spectroscopy suffered from a small scattering cross section. The problem could be solved by a surface-enhanced Raman scattering (SERS) technique which greatly enhanced the sensitivity of the conventional Raman spectroscopy [46-50]. This powerful technique hence was applicable to detect molecular species and had recently drawn a considerable attention in researches in chemical and biological analyses. In addition, SERS offered several potential advantages over other spectroscopic techniques because of its measurement speed, high sensitivity, portability, and simple maneuverability.

Despite a considerable number of researches in the SERS technique, its mechanism was still under debated [46-51]. In general, enhancement factors for the SERS substrates were reported between  $10^6$  to  $10^8$  [51-55]. Note that, an extraordinarily high enhancement factor ( $\sim 10^{14}$ ) was reported on an active SERS system using colloidal silver molecules [56-57]. However, metal colloid suffered from its aggregation states. Although different analyses produced different aggregation states, they equally imposed unreliable Raman intensity and difficulty for standardization. Lithography was another ideal method for producing uniform and reproducible SERS substrates [58-60]. Although their enhancement factor could be achieved up to  $\sim 10^9$  [60], the lithographic technique was very expensive in a large-area production of the SERS substrates. In this work, a fabrication process of low-cost and highly sensitive SERS substrates, based on a magnetron sputtering system was reported. The magnetron sputtering technique had a primary advantage in an

easy adaptation to a large-scale production. The magnetron sputtering system was used to deposit silver nanoparticles on top of a thin AAO template which was previously coated on each silicon substrate. The presence of the AAO template helped increase the surface area and prevent coalescence of the deposited silver nanoparticles. The AAO template thus maintained a high density of the silver nanoparticles to obtain a large SERS enhancement factor. Note that the silicon-based support made the SERS substrates easier to handle than those fabricated on fragile porous alumina foils as previously reported [61].

# CHAPTER III

## MATERIALS AND METHODS

### 3.1 Quartz Crystal Microbalance Experiments

The feasibility of applying PVC-COOH to immobilize protein on QCM surface as an immunosensor is investigated. The QCM process in associating with PVC-COOH approach in morphology and its adsorption including with flow-injection analysis immunoassay is, to our knowledge, the first-time mentioned in the literature.

This chapter has provided the information of instruments and equipments, apparatus, chemicals and reagents, and sample preparation employed in this work.

#### 3.1.1 Instruments and Equipments

The following is the lists of apparatus used in QCM experiment.

3.1.1.1 An airbrush equipment is used for spray coating in preparation of quartz crystal surface roughness with PVC-COOH solution.

3.1.1.2 Veeco Dektak 150 step profiler is used to measure the depth of polymer coating which is related to deposition rate and time.

3.1.1.3 Hitachi's S-5200 field emission scanning electron microscope (FE-SEM) is used to investigate surface morphologies of polymer films deposited on quartz surface under varied deposition thickness.

3.1.1.4 Seiko Instrument SPA 400 atomic force microscopy (AFM) is used to verify the RMS roughness and surface morphology of each sample.

3.1.1.5 Ramé-Hart instrument model 250 is used to evaluate the hydrophilicity by a water contact angle measurement), which is performed in ambient temperature at 25°C, and relative humidity (RH) 50%.

3.1.1.6 The continuous flow QCM sensor system which is developed by Nanoelectronics and MEMS Laboratory (Thailand) is used for the cTnT detection experiments.

3.1.1.7 A homemade microchannel flowcell which is developed by Nanoelectronics and MEMS Laboratory (Thailand) is equipped with the QCM device and then connected to the syringe pump on one edge in order to collect the liquid flow.

3.1.1.8 NE-1000 programmable syringe pump from New Era Pump system, Inc. is used to continuously deliver a carrier solution into the flow system.

3.1.1.9 Universal frequency counter (Agilent 53131A) is used to record the change in mass loading of QCM sensor and directly measured through the quartz frequency shift.

3.1.1.10 Silver-surface AT-cut quartz crystal with a fundamental resonance frequency of 12 MHz from Stanford Research System Inc. is used for a based device.

3.1.1.11 An electrochemiluminescence detection (Elecsys) from Roche Co., Ltd. is used to measure the prepared cTnT solution concentration.

3.1.1.12 High-precision 780 Metrohm pH meter is used to measure the pH of prepared buffer solution.

3.1.1.13 Mettler AT 200 Balance analytical is used for weighing the solid stock chemicals in the preparation of reagent solution.

### 3.1.2 Chemical and Reagents

All chemicals are of analytical grade or better and are used without further purification. Deionized-distilled water obtained from a Milli-Q-system is used for the preparation of chemical and reagent solutions. The following table is the lists of chemical and their suppliers used in QCM experiment.

**Table 3.1** List of Chemicals and Reagents and their suppliers of QCM.

Chemicals/ Reagents	Formula	Suppliers
Carboxylic polyvinyl chloride (PVC-COOH)	$-\text{[CH}_2\text{CHCl]}_n-$	Sigma-Aldrich
1-Ethyl-3-(3-dimethylaminopropyl) carbodiimide (EDC)	$\text{C}_8\text{H}_{17}\text{N}_3$	Sigma-Aldrich
N-hydroxysuccinimide (NHS)	$\text{C}_4\text{H}_5\text{NO}_3$	Sigma-Aldrich
Tetrahydrofuran (THF)	$\text{C}_4\text{H}_8\text{O}$	Merck
Phosphate buffer saline (PBS, pH 7.4)	$\text{Na}_2\text{HPO}_4, \text{NaH}_2\text{PO}_4$	Sigma-Aldrich
Methanol	$\text{CH}_3\text{OH}$	Merck
Nitric acid	$\text{HNO}_3$	Merck
Protein G	-	Sigma-Aldrich
Casein	-	Sigma-Aldrich
Monoclonal antibody 9G6 for cTnT	-	Abcam
cTnT	-	Abcam

### 3.1.3 Preparation of solutions

These successive parts include the preparation procedures of standard solution employed for this works.

### **3.1.3.1 1 M Phosphate Buffer**

Stock solution of solid 1 M Phosphate buffer pH 7.4 is dissolved to required concentration by dilution with 1000 mL of deionized-distilled water and confirmed pH value by pH meter.

### **3.1.3.2 50 mM 1-Ethyl-3-(3-dimethylaminopropyl) carbodiimide (EDC)**

4.7925 mg of EDC are dissolved in 500  $\mu$ L of distilled water just before used into 1.5 mL microtube to give a solution of 50 mM.

### **3.1.3.3 25 mM N-hydroxysuccinimide**

5.7545 mg of NHS are dissolved in 500  $\mu$ L of distilled water just before used into 1.5 mL microtube to give a solution of 25 mM.

### **3.1.3.4 Carboxylic polyvinyl chloride**

1 mg of solid PVC-COOH is dissolved in 1 mL of THF with constant stirring for 10 minutes at room temperature.

### **3.1.3.5 0.025 $\mu$ g/mL Protein G**

2.5 mg/mL of the Protein G is diluted with 1 mL of 1 M Phosphate buffer pH 7.4 into 1.5 mL sterilized microtube to concentration at 0.025  $\mu$ g/mL.

### **3.1.3.6 0.1 % Casein**

0.1 mg of Casein blocking reagent is dissolved in 1 mL of Phosphate Buffer (pH 7.4) into 1.5 mL sterilized microtube to give a stock of 0.1 % Casein.

### **3.1.3.7 Monoclonal antibody 9G6 for cTnT**

0.025 mg/mL of cTnT antibody is diluted with 1 mL M Phosphate buffer pH 7.4 into 1.5 mL sterilized microtube to give concentration of 0.025  $\mu$ g/mL antibody for stock solution. The cTnT antibody stock solution has been kept in cool place at -20°C until used.

### **3.1.3.8 Stock standard Solution of cTnT**

The standard solution of cTnT solution at various concentrations can be prepared by appropriately diluting of 5 mg/mL stock cTnT solution with 1 M Phosphate buffer (pH 7.4). The concentration and volumes required for these preparations are shown in Table 3.2. In this work, the bench-top instrument of electrochemiluminescence detection technique is performed to verify cTnT concentrations before using cTnT solution in QCM and SERS experiments. The achieved concentrations of cTnT which were 5, 50, 500, 5,000 and 50,000 ng/ml have been kept in cool place at -20°C until used. Then, the verify cTnT concentrations are used in this experiment.

**Table 3.2** Compositions of cTnT Standards solutions.

<b>Final concentration of cTnT solution (ng/mL)</b>	<b>Concentration of cTnT solution (ng/mL)</b>	<b>Volume of stock solution (<math>\mu</math>L)</b>	<b>Volume of cTnT solution (<math>\mu</math>L)</b>	<b>Volume of 1M Phosphate buffer (<math>\mu</math>L)</b>
5	50	50	5	45
50	500	50	5	45
500	5,000	50	5	45
5,000	50,000	50	5	45
50,000	500,000	50	5	45

### 3.1.4 Preparation of Polymer film fabrication and characterization

Fabrication of the polymer film on quartz crystal surface consists of a multiple preparation steps. First, the quartz crystal is cleaned by Methanol. Then an airbrush system equipped with a 0.3 mm diameter nozzle as shown in Figure 3.1 is used to spray the solutions of PVC-COOH on the active zone of the quartz crystal surface. The spraying pressure of 1 bar is controlled during the deposition of the polymer precursors. The deposition rate is determined by the polymer thickness using a Veeco Dektak 150 step profiler. A series of samples is prepared with deposition thickness of 100, 200, and 300 nm. Then the quartz crystal is washed five times in HNO<sub>3</sub> solution to eliminate excess of unbound polymer. Finally, the coated quartz crystal is rinsed with the PBS buffer to normalize the pH of polymer surface. The quartz crystal is dried under nitrogen gas (N<sub>2</sub>) prior to measurements.





**Figure 3.1** Airbrush equipment for spray coating.

Surface morphologies of polymer films deposited on quartz surface under varied deposition thickness are investigated by the Hitachi's S-5200 field emission scanning electron microscope (FE-SEM). The Seiko Instrument SPA 400 atomic force microscopy (AFM) is used to verify the RMS roughness and surface morphology of each sample. The hydrophilicity is evaluated by a water contact angle measurement (Ramé-heart) which is performed in ambient temperature at 25°C, and relative humidity (RH) 50%.

### 3.1.6 Flow injection system and stability of coated polymers under liquid

flow

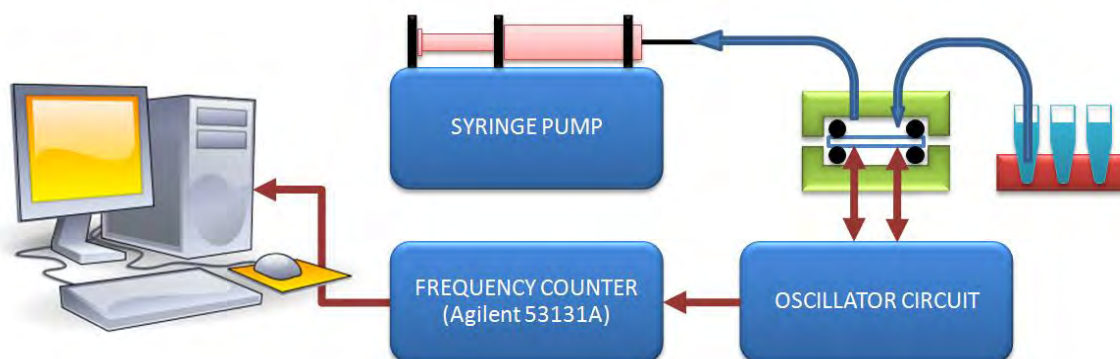


**Figure 3.2** The continuous flow QCM sensor system.

From Figure 3.2, the continuous flow QCM sensor system developed by Nanoelectronics and MEMS Laboratory (Thailand) is used for the cTnT detection experiments shown in Figure 3.2. This system consists of a NE-1000 programmable syringe pump. In Figure 3.3(a) and (b), a microchannel flowcell equipped with the QCM device is connected to the syringe pump on one edge in order to collect the liquid flow. The liquid passes through the surface of QCM and draw off on the opposite edge. The change in mass loading of QCM sensor is directly measured through the quartz frequency shift using a universal frequency counter (Agilent 53131A) connected to the device via an oscillator circuit. The measuring frequency shift data is transmitted to computer via a GPIB port. The complete QCM with flow injection system shows in Figure 3.4.

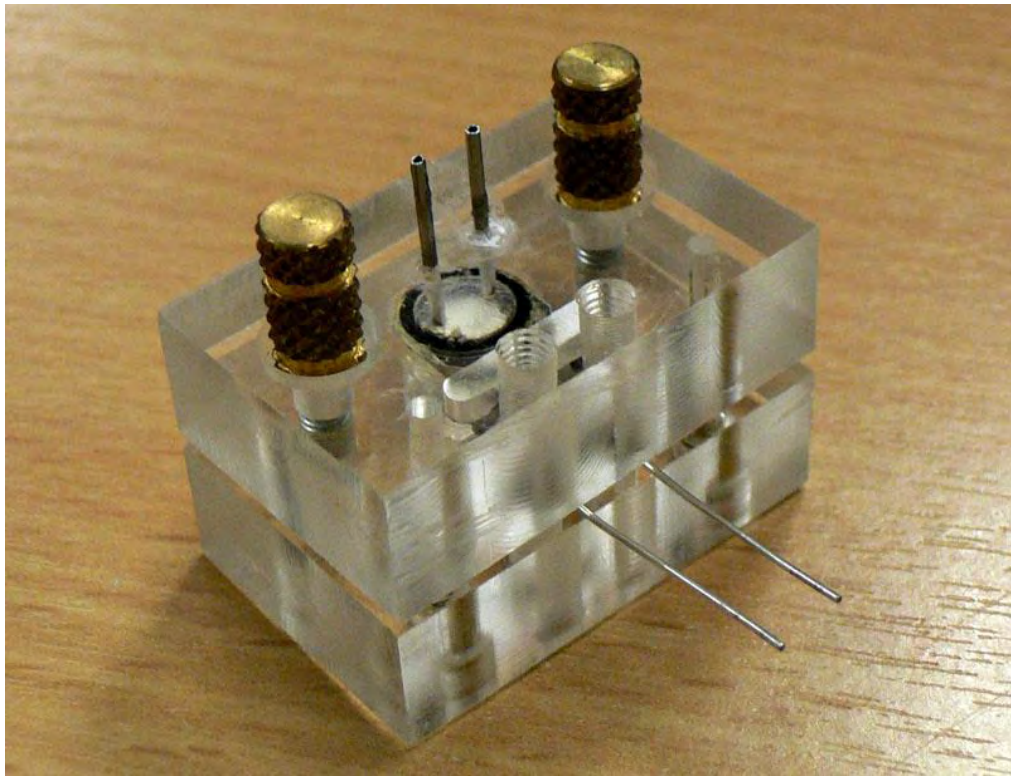


**Figure 3.3** (a) A microchannel flowcell (b) parts.

Prior to the cTnT detection, the stability of PVC-COOH coated QCM under flow injection system is investigated. This is done by injecting the PBS to the system at various flow rates ranged from 50  $\mu\text{L}/\text{min}$  to 500  $\mu\text{L}/\text{min}$ . The QCM frequency shift results from liquid flow are then observed. At this step, the flow rate that delivered the most stable frequency shift is determined. Subsequently, the polymer-coated QCM is tested under this flow rate for the rest of experiment.

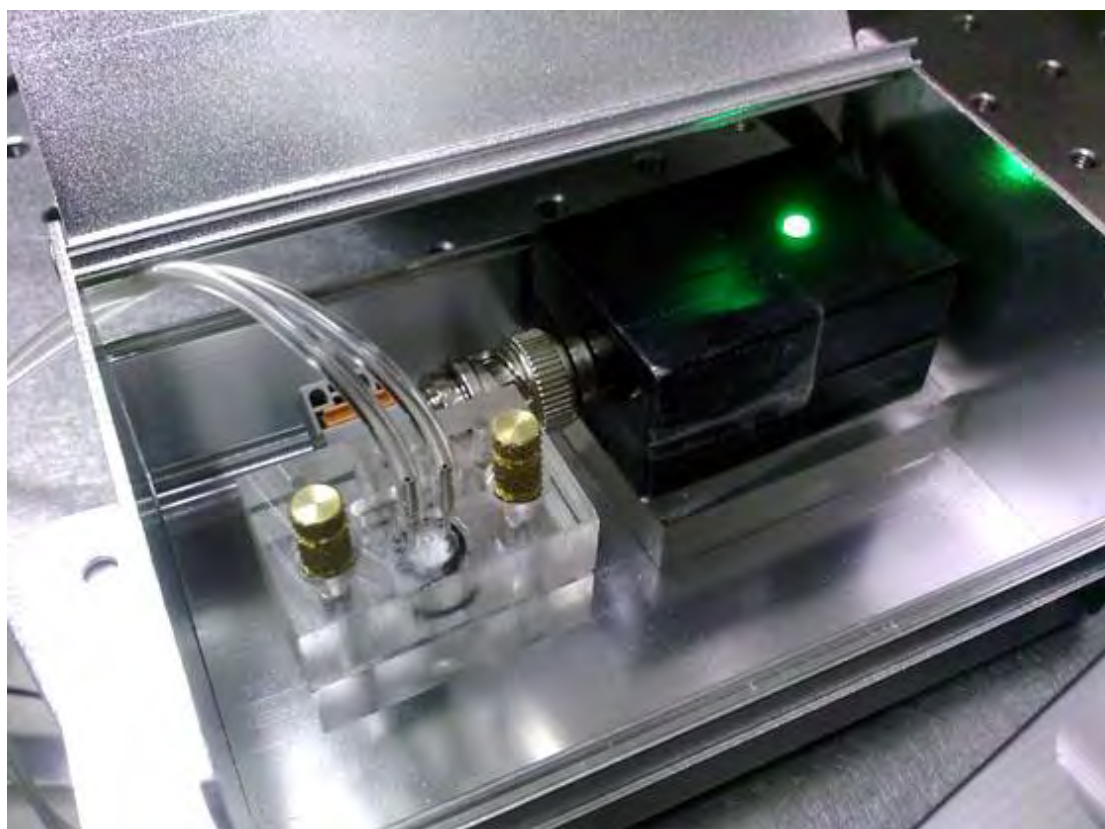


**Figure 3.4** A QCM with flow injection system.

### **3.1.6 Binding experiments**

During immobilization, the flow injection system was kept under a constant PBS flows. The immobilization sequence consisted of a multiple reagent injection

steps. A schematic diagram of the cTnT immobilization principle is concluded in Figure 3.5.

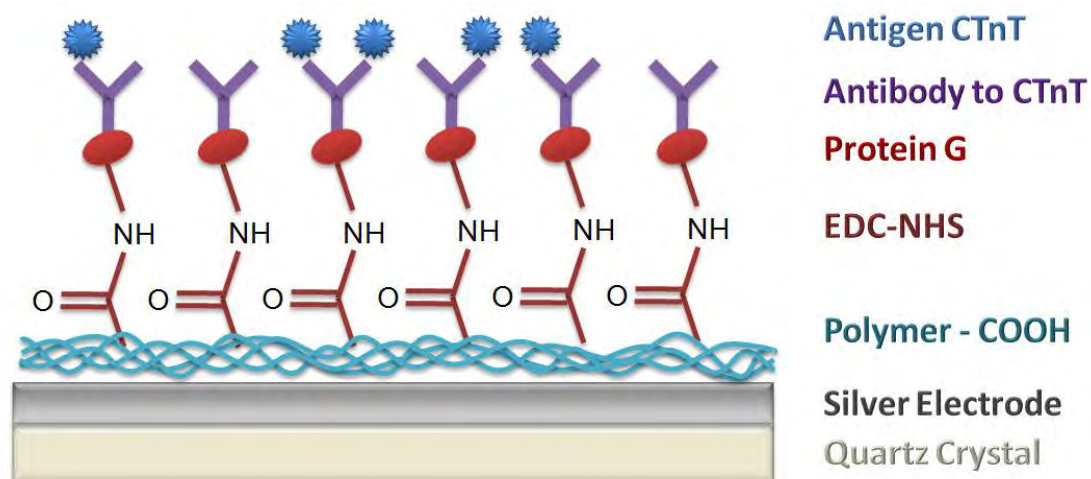


**Figure 3.5** Schematic diagram of coating layers on quartz crystal.

All reagents are injected into the system as the following steps. First, a mixer of 500  $\mu\text{l}$  EDC and 500  $\mu\text{l}$  NHS is injected into the flow system to activate the polymer-coated surface in order to immobilize Protein G via covalent bonds between a carboxyl group and an amine group. EDC react with carboxylic group on polymer surface and NHS is stabilized amide reactive intermediate as shown in Figure 3.6, thus increasing EDC- mediated coupling reaction with protein. Next, the Protein G coating is performed by injecting 1 mL of 0.025  $\mu\text{g}/\text{mL}$  protein G into the system in order to initiate binding reaction to the Fc regions of cTnT antibodies. The Protein G coating should considerably improve response of sensor at the antibody-antigen binding step. After that, 1 mL of 0.025  $\mu\text{g}/\text{mL}$  cTnT antibody is injected and followed by 1 mL of 0.1 % Casein blocking reagent. The blocking reagent is used to prevent nonspecific reaction of antigen to the excess dangling bonds. For antigen-

antibody binding step, 1 mL of cTnT antigen at fixed concentrations (5, 50, 500, 5,000 and 50,000 ng/mL) is injected into the chamber, and allows flowing for 20 minutes (loop system). The cTnT antigen is rinsed off with PBS to remove excess conjugated product. During the course of the experiment, the QCM frequency is recorded. Combined with the cTnT antigen-antibody binding, the frequency shift can now be correctly determined.

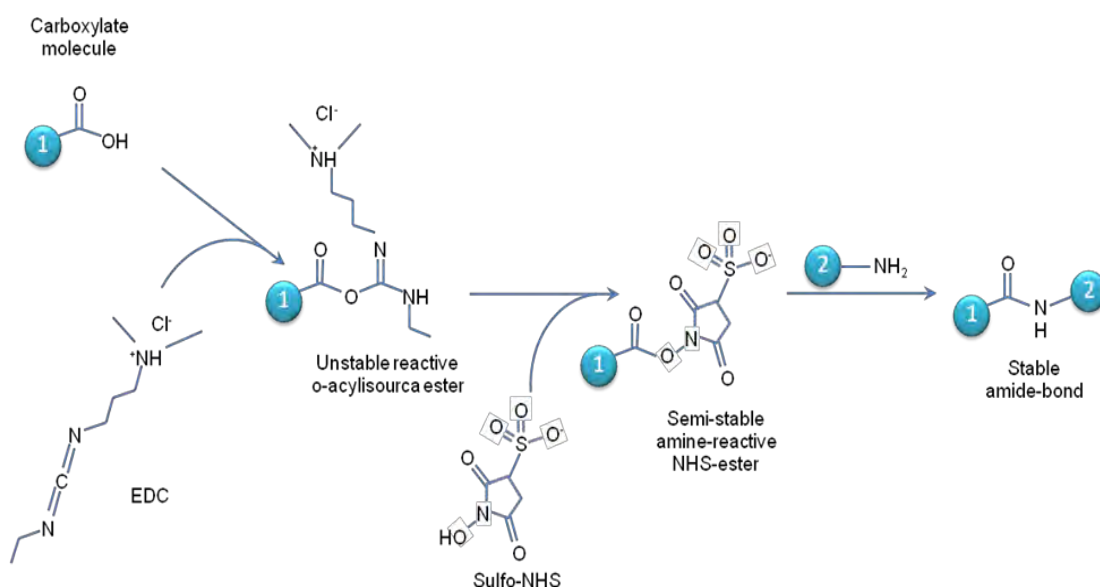


**Figure 3.6** EDC and NHS coupling reaction.

Due to the great potentials in biosensors applications QCM method could offer, the developments of the surface modification techniques have been widely studied. In this technique, the quartz crystal microbalance (QCM) sensor is coated with selected polymer that adsorbs the proteins and other biomolecules through an immobilization process. Because of the difference in physical properties of each

polymer, the choices of polymer and fabrication method are critical factors in enhancing an amount of the absorbed molecules on quartz crystal surface. In this work, the cTnT detection using QCM system is achieved by using Polyvinyl Chloride doped with carboxylic group coated on quartz surface as an immobilization layer. This polymer is used to improve the cTnT immobilization by introducing a carboxyl group between surface of a quartz crystal and the 1-Ethyl-3-(3-dimethylaminopropyl) carbodiimide (EDC), N-hydroxysuccinimide (NHS) crosslinker. The thicknesses of this polymer film under varied deposition thickness have been controlled using a step profiler. The surface morphologies are investigated using a field-emission scanning electron microscopy (FE-SEM) and an atomic force microscopy (AFM). Prior to the cTnT detection, a stability of polymer coated QCM under fluid flow is investigated by injecting the fluid into the continuous flow system at various flow rates. The stability of polymer film is analyzed by recording the frequency fluctuation due to changes in velocity/viscosity of the fluid. For the cTnT detection experiments, multiple immobilization steps are performed including adsorption of EDC and NHS crosslinker on polymer film, followed by protein G adsorption. Then the cTnT with controlled concentration is injected into the flow system. Using the modified QCM sensor, the presence of cTnT can be detected within a short response time by the direct detection of the immuno-reaction converted into the measurable acoustic resonant frequency shift. The experiments are repeated with cTnT at various concentrations ranged between 5 ng/mL to 50,000 ng/mL or 50  $\mu$ g/mL

The quartz crystal in the cell can be covered with 200  $\mu$ L PBS treated water and stored overnight in the fridge at 4°C for short-term storage. The measurements can be started again after the signal of sensor has stabilized in room temperature.

## **3.2 Surface enhanced Raman Spectroscopy Experiments**

Despite a number of extensive researches focused on the SERS technique, its mechanism is still under debated. It has now been widely recognized that for a given metal nanoparticle system, the SERS activity occurs for nanoparticles between 10-100 nm in size [51]. The most effective SERS substrates to date are colloidal silver or gold clusters widely used in the bulk-volume solution-based detections [52-55]. However, these nanoparticles fabricated from a chemical reduction usually lose effectiveness from residual organics. This may have an adverse influence in the work that requires a highly selective detection. In contrast, a fabrication of metal nanostructures by physical vapor deposition has relatively clean surfaces. The assembly of the nanostructural arrays on silicon substrate can be used as a SERS-active on a chip. The efforts in fabricating metal nanopillars [56], nanoclusters [57] and nanogrooves [58] as a SERS-active layer on silicon substrates have been extensively studied and demonstrated. Nonetheless, the sample fabrication of such reports requires significantly serious and expensive efforts that hinder their applications beyond a laboratory scale.

### **3.2.1 Instruments and Equipments**

3.2.1.1 Homemade high vacuum (HV) DC magnetron sputtering system which is developed by Photonics Laboratory (Thailand) is used to prepare the metal nanoparticles in the SERS substrates.



3.2.1.2 Hitachi's s-5200 field emission scanning electron microscope (FE-SEM) is used to verify the film thickness and also used to examine the lateral features of the AAO nanopores and the silver nanoparticles deposited on their matrix.

3.2.1.3 JEOL 2010 (200 kV) transmission electron microscope (TEM) is used to characterize the crosssectional details of the SERS structures.

3.2.1.4 NT-MDT NTEGRA Raman spectrometer equipped with a confocal optical microscopy system is used to characterize the Raman spectra.

3.2.1.5 Motech's LPS-305 digital power supply is used to precisely control the anodizing current.

3.2.1.6 A spectroscopic Elipsometer (HS-190) manufactured by J.A. Woollam is used to calibrate the deposition rate.

3.2.1.7 Milli-Q water system, model Millipore ZMQS 5 VOOY, Millipore, USA. is used to produce deionized-distilled water for preparing chemical and reagent solution.

### **3.2.2 Chemicals and reagents**

All chemicals are of analytical grade or better and are used without further purification. Deionized-distilled water obtained from a Milli-Q-system is used for the preparation of chemical and reagent solution. List of chemicals and their suppliers is summarized in Table 3.3.

**Table 3.3** List of Chemicals and Reagents and their supplier of SERS.

<b>Chemicals/ Reagents</b>	<b>Formula</b>	<b>Suppliers</b>
Methylene Blue	C <sub>16</sub> H <sub>18</sub> N <sub>3</sub> SCl	Sigma
0.3 M Oxalic acid	C <sub>2</sub> H <sub>2</sub> O <sub>4</sub> ·2H <sub>2</sub> O	Merck
Ortho-Phosphoric acid	H <sub>3</sub> PO <sub>4</sub>	Merck
cTnT	-	Abcam

### 3.2.3 Preparation of the solution

These successive parts included with the preparation procedures of standard solution employed in this work.

#### 3.2.3.1 Methylene Blue

The MB solutions are prepared with deionized-distilled water. The weight of MB solution is prepared from 1 M of 10 mL of Methylene Blue to concentration at 10<sup>-10</sup> M. The concentration and volumes required for these preparations are shown in Table 3.4.

**Table 3.4** Compositions of Methylene Blue Standard Solution.

<b>Final Concentration of Methylene Blue (M)</b>	<b>Concentration of Methylene Blue (M)</b>	<b>Volume of stock Solution (mL)</b>	<b>Volume of stock MB Solution (mL)</b>	<b>Volume of DI water (mL)</b>
$10^{-10}$	$10^{-8}$	10	1	9
$10^{-8}$	$10^{-6}$	10	1	9
$10^{-6}$	$10^{-4}$	10	1	9
$10^{-4}$	$10^{-2}$	10	1	9
$10^{-2}$	1	10	1	9

**3.2.3.2 0.3 M Oxalic acid**

37.8 g of Oxalic acid dehydrate is weighed and dissolved in deionized-distilled water with final volume 1 litre of solution to give a stock solution of 0.3 M.

**3.2.3.3 5 wt % H<sub>3</sub>PO<sub>4</sub>**

0.8622 M of H<sub>3</sub>PO<sub>4</sub> is diluted in deionized-distilled water with final volume 1 litre of solution to give a stock solution of 5 wt % H<sub>3</sub>PO<sub>4</sub>.

**3.2.3.4 Stock standard Solution of cTnT**

The standard solution of cTnT solution at various concentrations can be prepared by appropriately diluting of 5 mg/mL stock cTnT solution with 1 M Phosphate buffer (pH 7.4). The concentration and volumes required for these

preparations are shown in Table 3.5. The achieved concentrations of cTnT which were 5, 50, 500, 5,000 and 50,000 ng/ml have been kept in cool place at -20°C until used. Then, the verify cTnT concentrations are used in this experiment.

**Table 3.5** Compositions of cTnT Standards solutions.

<b>Final concentration of cTnT solution (ng/mL)</b>	<b>Concentration of cTnT solution (ng/mL)</b>	<b>Volume of stock solution (μL)</b>	<b>Volume of cTnT solution (μL)</b>	<b>Volume of 1M Phosphate buffer (μL)</b>
5	50	50	5	45
50	500	50	5	45
500	5,000	50	5	45
5,000	50,000	50	5	45
50,000	500,000	50	5	45

### **3.2.4 Preparation of the substrate**

The fabrication process of a SERS substrate consists of several steps that can be concluded in Figure 3.7 and 3.8.

#### **3.2.4.1 Sputtering system**

All of the metal nanoparticles in the SERS substrates are prepared by a homemade High Vacuum (HV) DC magnetron sputtering system. The deposition chamber reaches a base pressure at approximately  $1 \times 10^{-3}$  Pa. During the film deposition, an operating pressure is maintained at 0.4 Pa by a throttle valve. Plasma

cleaning is performed for 5 minutes prior to the metal deposition on the silicon surface using 70 watts of an RF power, 16.25 MHz of an RF frequency, and 5 sccm of an argon flow. The metal deposition is then followed with a DC sputtering power of 34 watts. The Magnetron sputtering system is shown in figure 3.7.



**Figure 3.7** Magnetron sputtering system.

#### **3.2.4.2 Preparation of AAO templates**

For each AAO template, a 120 nm thick aluminum film is first deposited on a (100) silicon substrate. In an anodizing step, the substrate is connected to a power supply of an anodic electrode, and subsequently immersed in 0.3 M oxalic acid. A gold plate on the silicon substrate is used as a cathodic electrode. The anodizing

current is precisely controlled by a Motech's LPS-305 digital power supply at the current of 10 mA with the voltage limit of 40 volts. During this step, a large fraction of the aluminum film will be transformed into nanopores confined to 5-10 nm  $\text{Al}_2\text{O}_3$  side walls. The substrate is then submerged in 5 wt %  $\text{H}_3\text{PO}_4$  for 30 minutes in order to remove the  $\text{Al}_2\text{O}_3$  layer, thus opening cylindrical nanochannels along the top surface of the AAO film toward the silicon surface.

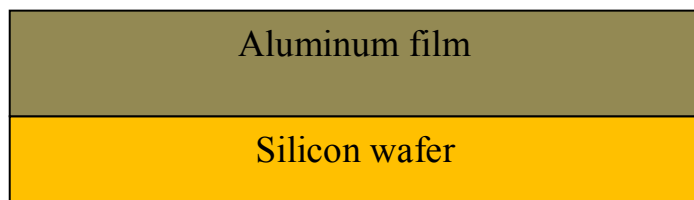
#### **3.2.4.3 Sputtering of silver nanoparticles**

The silver nanoparticles are deposited on each AAO template by the DC magnetron sputtering system. The sputtering target is a 3-inch high-quality pure (99.99%) silver manufactured by K.J. Lesker. The deposition rate is approximately 1 nm/s as calibrated by a spectroscopic ellipsometer (HS-190) manufactured by J.A. Woollam.

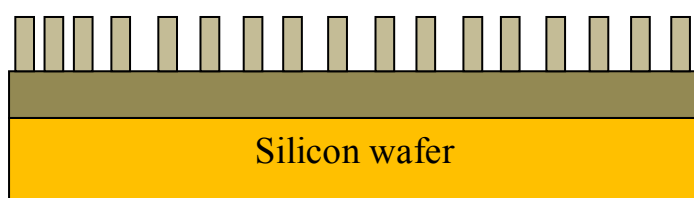
#### **3.2.4.4 Surface characterizations and analyses**

The film thickness is verified by Hitachi's s-5200 field emission scanning electron microscope (FE-SEM). The FE-SEM is also used to examine the lateral features of the AAO nanopores and the silver nanoparticles deposited on their matrix. The crosssectional details of the SERS structures are characterized by JEOL 2010 (200 kV) transmission electron microscope (TEM).

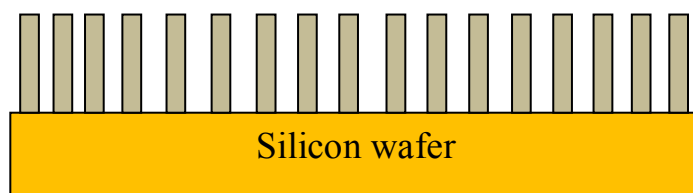
1. Sputtering Aluminum film



2. Anodizing



3. Nanochannel open



4. Silver nanoparticles deposition

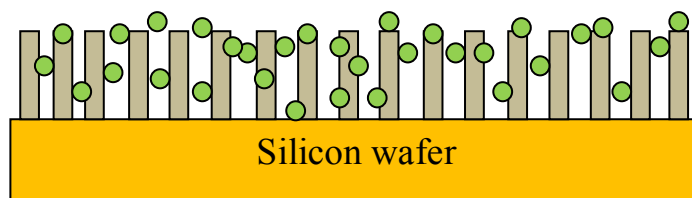
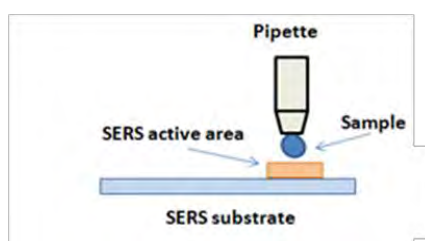


**Figure 3.8** Anodizing Aluminum Oxide (AAO) template.

### 3.2.5 Raman scattering characteristics

The fabricated SERS substrates are cut into several  $5 \times 5 \text{ mm}^2$  pieces. Each of these samples will be one time used to characterize reference molecules. In this report, Methylene Blue is selected as probing molecules on the fabricated substrates in order to determine the SERS activities and cTnT is tested for determining SERS quality which show the step of detection in Figure 3.9. Figure 3.9(a) shows the analyzed sample which is dropped onto the SERS surface. Figure 3.9(b) shows a sensitive NT-MDT NTEGRA Raman spectrometer equipped with a confocal optical microscopy system which is used to characterize the Raman spectra. The Laser which is spotted on monolayer of sample can be emitted Raman scattering and then collected by laser detector.

(a)



(b)

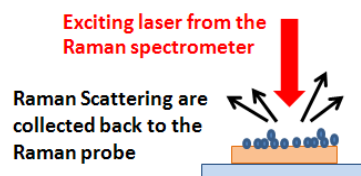


**Figure 3.9** (a) Raman spectrometer system in the experiment before testing and (b) after exciting laser.



### **3.2.7 Procedure of binding experiments of cTnT**

Prior to the measurements, 2.5  $\mu\text{L}$  in volume of Troponin T at varied concentrations are deposited on each SERS surface. The sample with the Troponin T droplet is left to dry at room temperature in an air atmosphere, and is immediately measured for the Raman spectra using a 785 nm He-Ne laser excitation. In this study, the Raman scattering characteristics are conducted as the Troponin T concentration varies between  $5 \times 10^{-9}$  g/mL (5 ng/mL) and  $5 \times 10^{-6}$  g/mL (5  $\mu\text{g/mL}$ ).

# CHAPTER IV

## RESULTS AND DISCUSSION

This chapter results and extensively discusses the results obtained from the experiments which are based on the Quartz Crystal Microbalance (QCM) system and the Surface-Enhanced Raman scattering (SERS) substrates.

### 4.1 Quartz Crystal Microbalance Experiments

In this work, the use of PVC-COOH in polymer film fabrication was studied to improve the quartz crystal surface roughness for immobilization of protein and antibody. The flow injection system which was used in cTnT detection experiments was tested. The stability of flow rate to control the pressure factor was investigated. The successful plot obtained from modified QCM with flow system for cTnT detection was also described.

#### 4.1.1 Polymer film morphologies on quartz crystal

The surface feature of uncoated and coated quartz crystal with 200 nm thick PVC-COOH were investigated with a field-emission scanning electron microscope (FE-SEM) as shown in Figures 4.1(a) and 4.1(b), respectively. Changes in surface morphology of quartz crystal after PVC-COOH film deposition can be obviously observed. A step-like surface of the quartz crystal was smoothed by existence of PVC-COOH film. From Figure 4.2(a)-(c), the water contact angles of quartz crystal show more adhesions from the fabricated polymer at the surface. The Figures show

the hydrophilic properties of films coated at deposition time of 10, 20 and 30 seconds, respectively. These images were taken after depositing a 20  $\mu\text{l}$  droplet of DI water. It was observed that the film deposited at 30 seconds provided a smaller contact angle ( $45.4^\circ$ ) than the deposition time at 10 and 20 seconds ( $70.3^\circ$  and  $95.7^\circ$ ).

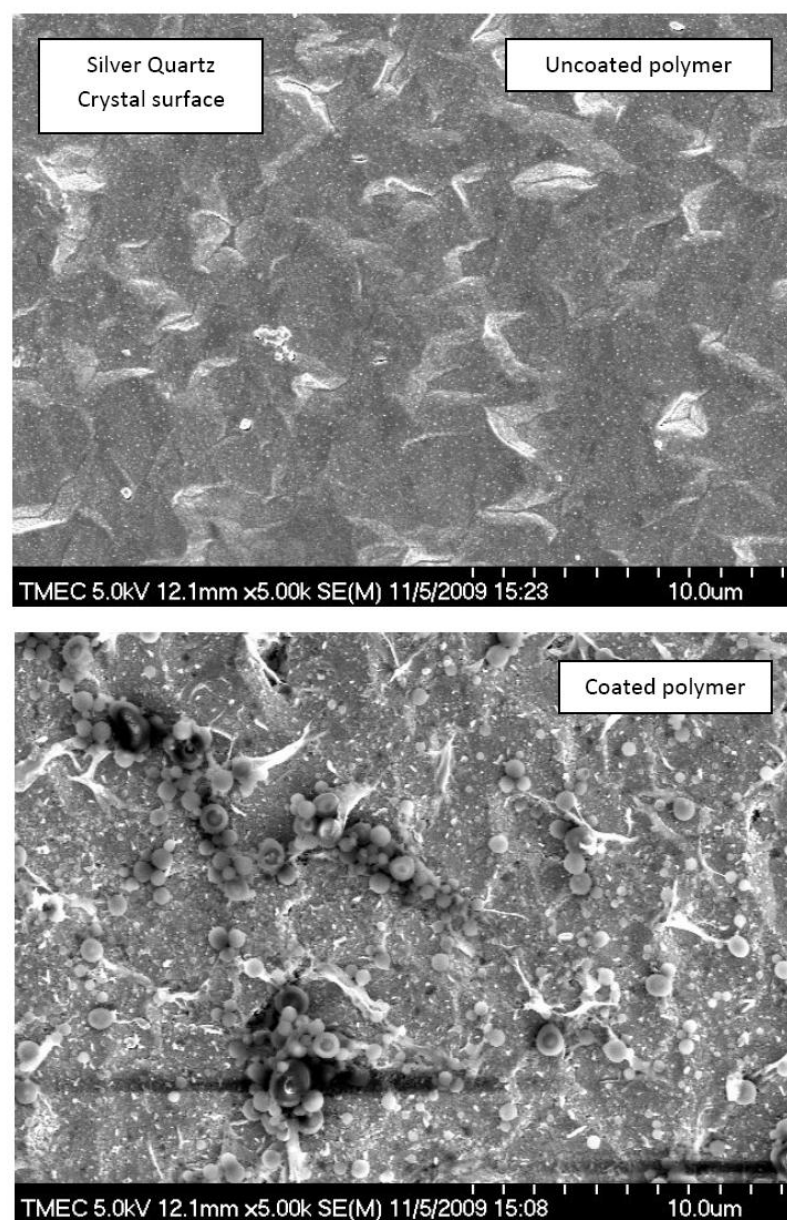


**Figure 4.1** SEM images show surface morphologies of (a) uncoated and (b) PVC-COOH coated quartz surfaces.

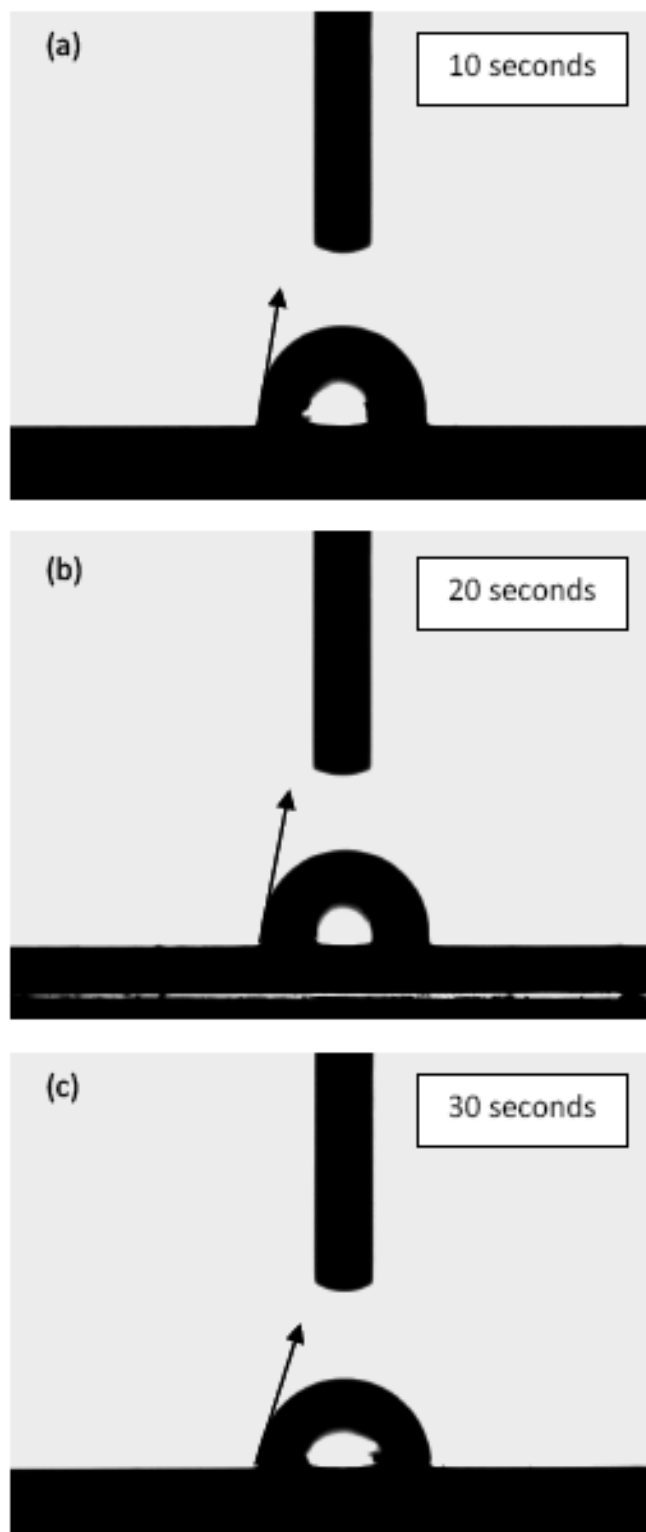


**Figure 4.2** Hydrophilic property images of (a) 10 seconds (b) 20 seconds and (c) 30 seconds of coating time.

Note that the Contact angle is defined by Young's equation, the roughness surfaces ( $r$ ) is defined by  $r = \text{true area} / \text{projected area}$ . For a rough surface, the contact angle is defined by Wenzel equation.

$$\cos \theta_{\text{apparent}} = r \cos \theta_{\text{true}} \quad (4.1)$$

In general, the decrease in the water contact angles implies the decrease in the films' surface roughness. It can hence deduce that the films in Figure 4.2(b) and (c), which have smaller contact angles, should have smoothed surface. This is in agreement with the results from FE-SEM images, where the surface of coated PVC-COOH consist of long polymer chains crisscrossing along the entire area. These experiments result in high-density micropores, which assist the adsorption of proteins in next QCM step experiment. The end result proves that the film deposited at 30 seconds is superior than those at 10 and 20 seconds in attracting polar, i.e., biomolecular molecules.

Further investigations by AFM, the root-mean-square (RMS) roughness can be related to the film thickness, as shown in Table 4.1.

**Table 4.1** RMS roughnesses of PVC-COOH coated quartz surfaces after polymer films deposited at various thicknesses.

<b>Thickness (nm)</b>	<b>0</b>	<b>100</b>	<b>200</b>	<b>300</b>
<b>RMS roughness (nm)</b>	95.72	6.72	56.87	44.76

The result in Table 4.1 indicates that an uncoated quartz surface consists of a rough surface with RMS roughness of 95.72 nm. The roughness decreases to 6.72 nm with a presence of 100 nm thick PVC-COOH film. The RMS roughness then increases to value of 56.87 nm with an increase in deposition thickness to 200 nm. At 300 nm thick, a polymer surface became flatter with RMS roughness value of 44.76 nm, which is most likely due to coalescence of polymer film. The optimum value of RMS roughness at 200 nm thick film could be benefit for immobilization of protein due to the largest surface area available in this series of film coating. From this reason, the PVC-COOH polymer film at a thickness of 200 nm was selected to be used as an immobilization layer of the QCM system. As quantified by the contact angles, the dispersive adhesion of PVC-COOH to the quartz crystal surface were held together by Van der Waals forces.

The AFM images are shown in Figure 4.3(a-c) for active regions of quartz crystal surfaces coated at 10 seconds, 20 seconds and 30 seconds, respectively. As the coating time of polymer increased from 20 to 30 seconds, the decrease in roughness can be observed. This was the result of 2.5% PVC-COOH which adhered on surface by the increase of coating time. The roughness of microscopic image increased with polymer thickness from 100 nm to 300 nm. After coating time of 30 seconds, the thickness was begun to decrease. The decrease in roughness associated with the thickness of polymer layers can be attributed to polymer suspension and polymer density.

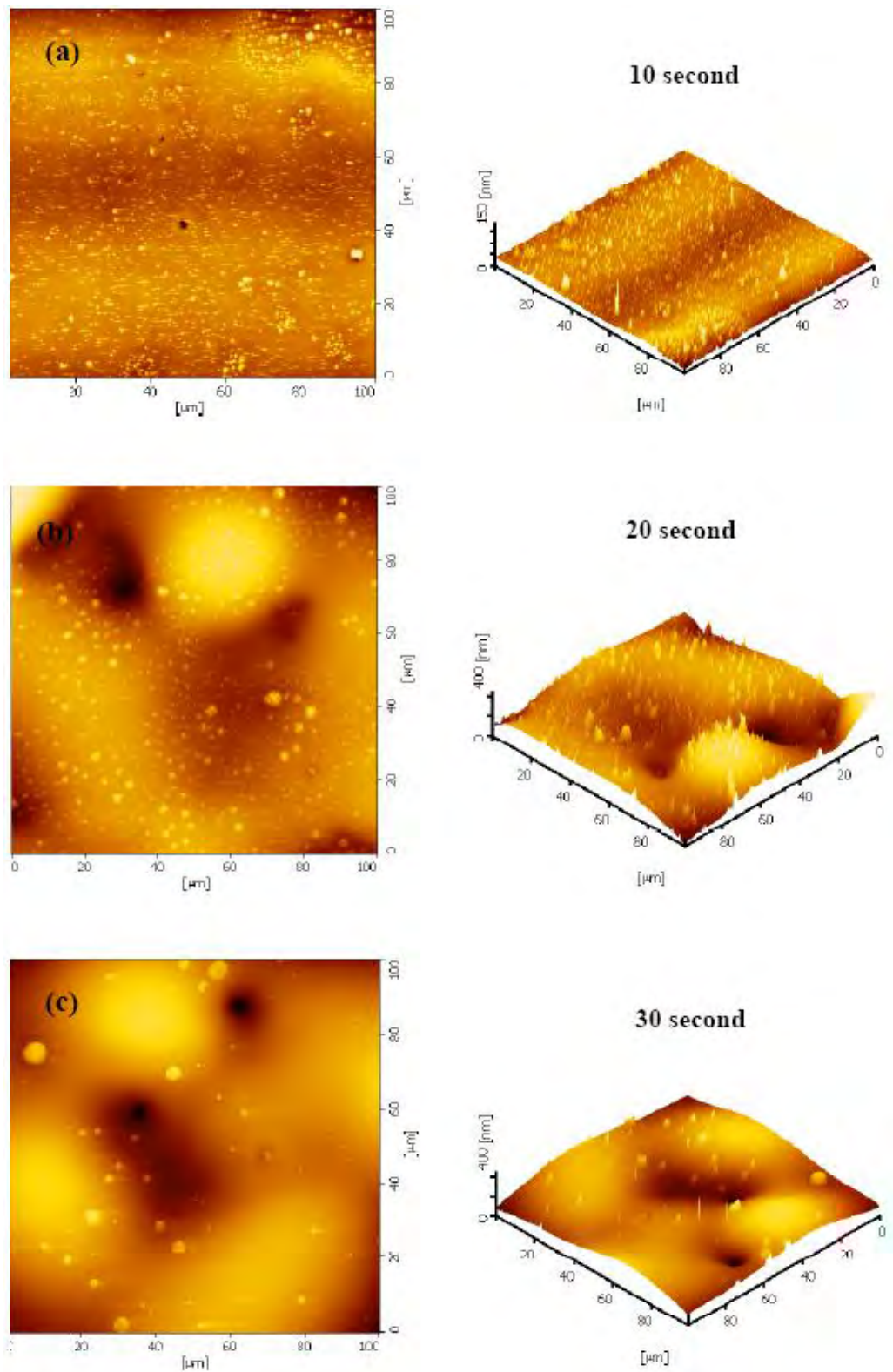


**Figure 4.3** AFM images show surface morphologies of (a) 10 seconds (b) 20 seconds and (c) 30 seconds of coating time.

#### 4.1.2 Stability of the polymer film under PBS flow

The results of an uncoated quartz crystal under various flow rates at 50, 100, 200, 300, 400 and 500  $\mu\text{L}/\text{min}$  indicated that the negative frequency shift was almost linearly proportional to the flow rate due to the increase in mass loading from the fluid pressures.

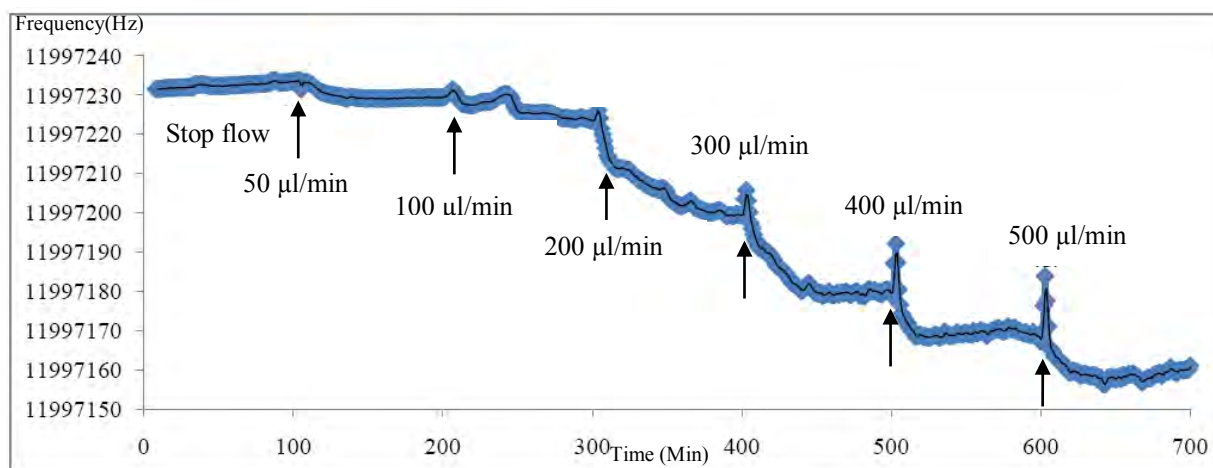


**Figure 4.4** Frequency response of modified QCM sensor under continuous flow system at multiple flow rate steps.

At higher flow rates a fluctuation of the frequency, which was due to the pressure surge of the pump, could be detected. Figure 4.4 shows the influence of the flow rate on the measured frequency. An increase of the fluctuation of frequency was measured with higher flow rates. The lowest standard deviation in the range of 5Hz could be measured with PBS buffer at flow rates ranging from 50 to 500  $\mu\text{L}/\text{min}$ . The frequency shift started from about 120 Hz with flow rate of 50  $\mu\text{L}/\text{min}$  to around 700 Hz at flow rate of 500  $\mu\text{L}/\text{min}$ . However, the flow rates only at 50 and 400  $\mu\text{L}/\text{min}$  which rendered a stability of frequency shift within 5 minutes were found after the



injection. The unstable frequency shift at other flow rates were most likely due to fluctuation in the fluid velocity after interacting with polymer coated surface. From this reason, the flow of 50  $\mu\text{L}/\text{min}$  was maintained for the rest of the experiments.

**Table 4.2** The Standard deviation of the varying flow rate.

<b>Flow rate (<math>\mu\text{L}/\text{min}</math>)</b>	50	100	200	300	400	500
<b>Standard deviation (Hz)</b>	1.14	4.77	5.45	4.03	3.98	1.56

Table 4.2 shows the standard deviation of several flow rates. The increase in the standard deviation with higher flow rates was expected due to the pressure fluctuation of the quartz crystal surface. A drop of the frequency at higher flow rates and higher hydrostatic pressure could be observed as well. The increase of the frequency shift can be explained by total frequency shift. The result of the mass deposition and the frequency shift were done by hydrostatic pressure at higher flow rates.

#### **4.1.3 Reusability of QCM sensor**

A modified QCM was regenerated as its quartz surface was rinsed with 0.1 M sodium hydroxide after the previously discussed experiment. The protein layer was removed from surface by changing the pH-value to alkaline. Then the cross-linker layer was rearranged by changing environment to pH 7.4. The frequency response was shown in Figure 4.5. With this procedure, the PVC-COOH coated QCM was successfully reactivated to collect new experimental data up to 3 times.

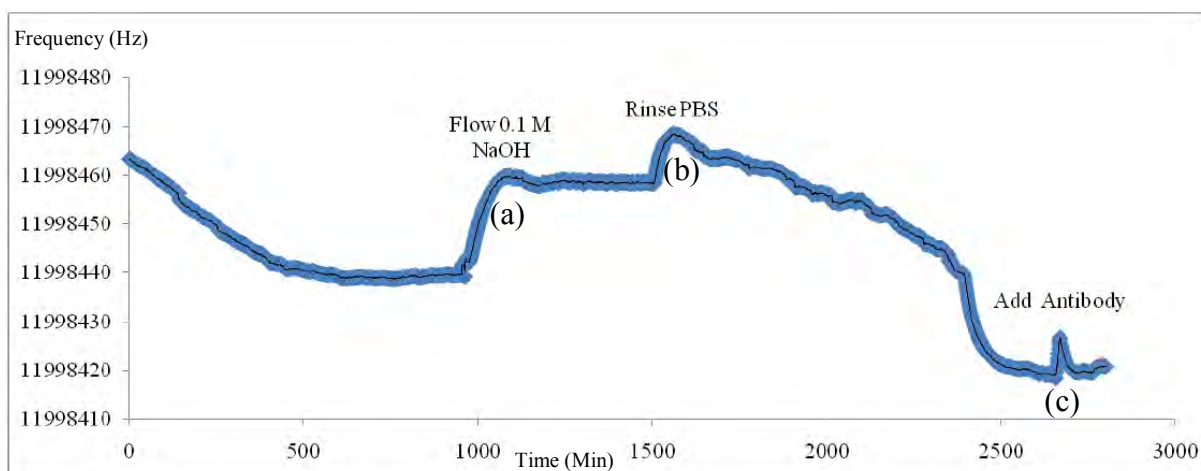


**Figure 4.5** Frequency response of reusability steps of QCM sensor under flow system at flow rate  $50 \mu\text{L}/\text{min}$  (a) flow  $0.1 \text{ M NaOH}$ , (b) rinse PBS buffer, and (c) add antibody.

The reactivation or reuse process consisted of several steps on the quartz crystal in the exact order. First, the PBS buffer was rinsed under flow rate  $50 \mu\text{L}/\text{min}$  for 10 minutes. Next, the  $0.1 \text{ M}$  sodium chloride was introduced to the quartz crystal and then flowed for 5 minutes. Then the quartz crystal was rinsed again with PBS buffer for 10 minutes. After washing step, antibody of cTnT was added for other experiments and the quartz crystal can be tested again.

Several regeneration solutions for different applications had been reported, for examples,  $0.05 \%$  SDS [79] and harsh solution such as  $1 \text{ M HCl}$  were rinsed to unfold the protein [80]. Due to the sensitivity of the protein-sensor to the ionic strength [81-82], several experiments were performed with the regeneration solution. The solution containing  $0.6 \text{ mM NaOH}$  mixed with  $0.6 \%$  Ethanol [83] was also used to denature protein bonding resulted in a complete regeneration of the sensor in one step without any significant loss of sensitivity of cTnT antibody. This offered the advantage that

the developed sensor was usable for more experiments due to the less aggressive regeneration solution.

## 4.2 QCM Experiments of cTnT

The frequency shift response of PVC-coated QCM sensor including all immobilization procedures, which started from initial PBS flow to antibody-antigen binding step on QCM sensor surface, was shown in Figure 4.6 as time progresses.

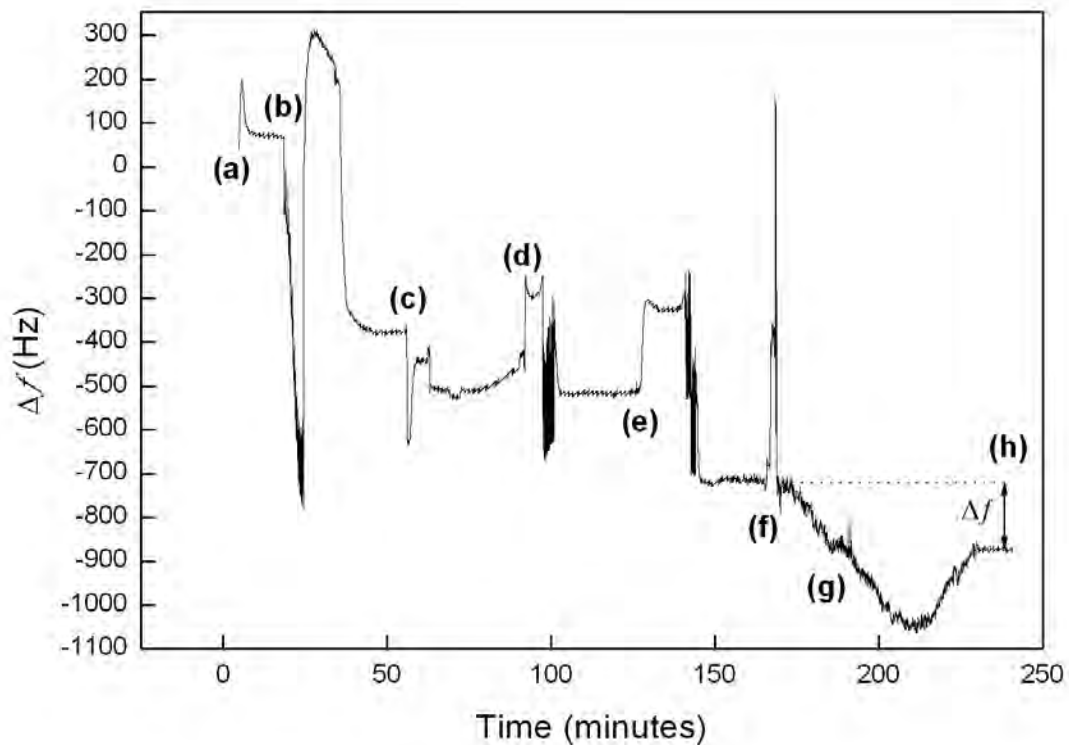


**Figure 4.6** Frequency response of modified QCM sensor under continuous flow system at multiple immobilization steps (a) introducing PBS flow (b) EDC/NHS adsorption, (c) Protein G coating, (d) cTnT Ab coating, (e) Casine blocking reagent coating (f) Ab-Ag complex and (g) PBS rinse (h) steady-state level of 50 ng/mL cTnT detection.

In step (a), the PBS flow was introduced into the system resulted in frequency fluctuation at about 200 Hz. After 15 minutes, the frequency shift became stable and the mixer of EDC/NHS was injected into the flow system as shown in step (b). At this step, the frequency fluctuated down and up at frequency range at about 1 kHz due to an abrupt change in viscosity. This type of fluctuation was expected for every injection step. The EDC/NHS was injected at continuous rate for 15 minutes. After the flow stops, the frequency dropped and became stable at frequency shift of about 440 Hz below the previous step. This indicated an increase in mass loading from adsorption of EDC/NHS on PVC-coated QCM surface. In step (c), diluted Protein G was injected into the system also resulted in another frequency fluctuation. After Protein G was injected for 10 minutes, the frequency shift was about 150 Hz below the previous step. The plot shown that the resonant frequency gradually increased within the range of 50 Hz when cTnT antibody was introduced into the system at step (d). The increases in this frequency suggested that Protein G can be adsorbed on QCM surface and was partially dissolved by PBS buffer. At step (d), the cTnT antibody was injected into the system for 10 minutes resulted in a stable frequency shift of about 50 Hz from the binding activity between protein G and antibody. The frequency was stable under PBS flow for 30 minute until the Casein blocking reagent was introduced in step (e). After this step, the frequency dropped about 200 Hz due to additional mass from Casein.

The Ab-Ag binding activity can be seen after cTnT antigen was injected into the system for 2 minutes at step (f). It can be observed that QCM responded well to the controlled concentration of the cTnT at 50 ng/mL under 20 minutes of the loop

flow between step (f) and (g). At step (g), the loop flow was disconnected and the PBS rinse was performed. After this step, the plot shown that resonant frequency still decreased for another 25 minutes, then increased from a removal of the excessive binding. The frequency became stable after 20 minutes, where the steady state of the frequency shift was found at  $\Delta f = 150$  Hz. The noise level of this measurement was less than  $\pm 5$  Hz. The total time for the preparation step (a) to (f) was 2 hours and 40 minutes. This experiment took 1 hour for response time in cTnT antibody-antigen reaction from step (f) to steady state in step (h).

To calculate the relation of  $\Delta f$  and mass deposition, the Sauerbrey is first demonstrated the effect written by

$$\Delta f = - C_f \Delta m \quad (4.2)$$

In this research, consideration of simultaneous mass and liquid loading by Kanazawa and Martin shows the frequency shift relates to adsorbed mass and the density and viscosity of the contact liquid written below

$$\Delta f = C_f \Delta m - C_f (\Delta \rho \eta / 4\pi f_0)^{1/2} \quad (4.3)$$

Where  $\Delta f$  is the differentiate of frequency shift between after and prior mass deposited on quartz crystal,  $\rho$  is density of quartz,  $2.648 \text{ g/cm}^3$ ,  $\eta$  is shear modulus of quartz,  $2.947 \times 10^{11} \text{ g/cm} \times \text{s}^2$  and  $f_0$  is resonant frequency of the unloaded crystal.

The effect of concentrations on quartz crystal related to mass deposition by Kanazawa equation which was relied on mass loading in the same conditions. It had

been studied as a function of higher concentration of Cardiac Troponin including 5, 50, 500, 5,000, 50,000 ng/mL. Table 4.3 was calculated using  $\rho_L = 998.2 \text{ kg/m}^3$ ,  $\eta_L = 1.002 \times 10^{-3} \text{ N} \times \text{sec/m}^2$  and the surface area of quartz crystal in an oscillation range of 12 MHz =  $0.071 \text{ cm}^2$  which can be determined by

$$\Delta f = -f_q^{3/2} \sqrt{\frac{\eta_L \cdot \rho_L}{\pi \cdot \mu_q \cdot \rho_q}} \quad (4.4)$$

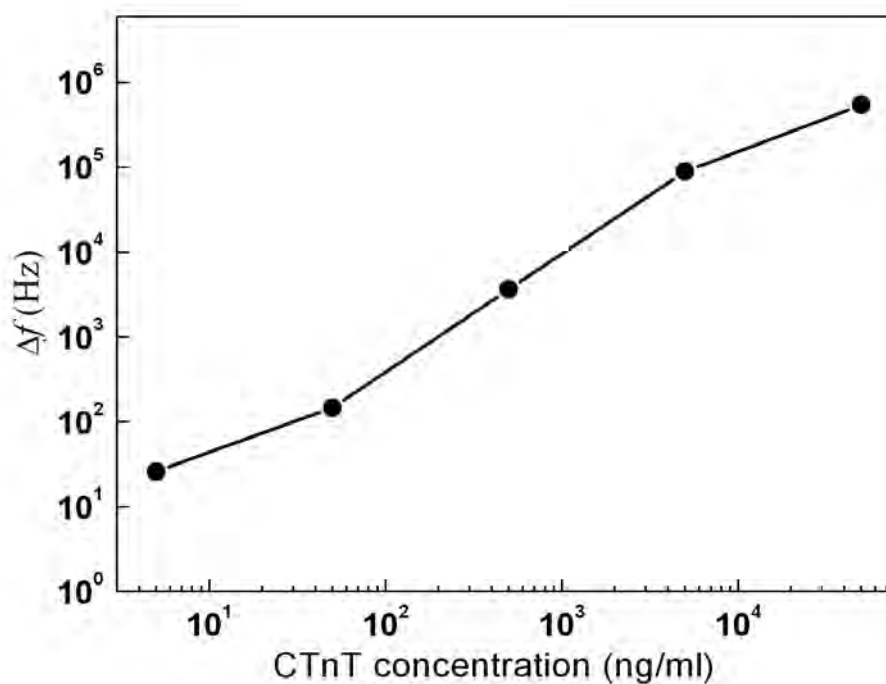


**Figure 4.7** QCM frequency shift of the modified QCM sensor as function of cTnT concentration in the log scale.

It can be calculated  $\Delta m$  and mass deposition from data of all results. The average frequency shift changes were observed between 0 to 12,000 Hz. The lower concentration was attributed to increase in percent of precision from 500 to 5 ng/mL

and induced the fabricated surface of crystal to be bound with protein molecules specifically. The decrease of precision percentage which was associated with no antibody receptor for Troponin was most likely caused by specific binding ligand from antigen antibody reaction.

**Table 4.3** Calculated  $\Delta m$  and mass deposition.

<b>cTnT concentration (ng/mL)</b>	<b>Frequency shift (Hz)</b>	<b><math>\Delta</math> Mass (ng/cm<sup>2</sup>)</b>	<b>Mass on QCM</b>	<b>Precision (%)</b>	<b>Average concentration</b>
5	17	52.1	3.70	85.7	4.285
50	150	460	32.66	82.126	41.063
500	1,701	5,217	370.40	85.64	428.2
5,000	8,590	26,348	1,870.7	37.24	1862
50,000	11,114	37,160	2,638.36	5.509	2,754.6

The experiment was repeated with the cTnT at other concentrations ranged between 5 ng/mL to 50  $\mu$ g/mL as plotted in Figure 4.7 with the values of cTnT concentration and average frequency shift data shown in the Table 4.3. The frequency shifts were found to be proportional to the cTnT concentration, which started from 23 Hz at the cTnT concentration of 5 ng/mL. The frequency shift increased drastically to 3.7 kHz while the cTnT concentration reached to 0.5  $\mu$ g/mL. At concentration of 50  $\mu$ g/mL, the frequency shift increased to 542 kHz. This value was close to the upper delectability limit of QCM, which was around 1 MHz for 12 MHz QCM. This Figure indicated that the developed QCM system can detect diluted cTnT concentrations down to the detection limit at the concentration of 5 ng/mL. At the lower concentration, the frequency shift was embedded under the noise level (around  $\pm 5$  Hz) and cannot be calculated.

Although the sensitivity of this report was lower than other recent methods in clinical measurements, the use of developed QCM sensors can be beneficial to an alternative screening diagnosis for disposable, low cost and reliable cTnT immunosensors. The ultrahigh sensitivity can be achieved from the increase of frequency range and combined surface modification techniques [62-68]. From Table 4.4, the measurement of cardiac Troponin T with a antibody based biosensor was limited to 0.1 ng/mL (Roache<sup>®</sup> Diagnosis). Another commercially available assays such as Abbott and Stratus were limited to 0.001 mg/mL of cardiac troponin I (cTnI) detection. Other studies reported the detection reach limit of cTnI at 0.03 ng/mL (RAMP<sup>®</sup>) and 0.02 ng/mL (PATHFAST<sup>®</sup>), respectively. Other methods, cardiac Troponin can be found to detect by monoclonal antibodies with Surface Plasmon Resonance (SPR) [69-70]. Although, the clinical ELISA assay can also be performed with a detection limit of 0.5 ng/L as described in Chapter II, the developed cTnT-sensor for the detection of cTnT offered the possibility of a new assay with a lower detection limit. Otherwise, the signal of 542 Hz for 50 ng/mL of cTnT was also indicated that the serum samples can be diluted which would also offered advantages due to the sensitivity of the cTnT-sensor on the ionic strength of the solutions.

The lists of result using different concentration of cTnT in Table 4.5 shown the records of standard deviation from each concentration which were in the same range in lower cTnT concentration. At 5, 50, and 500 ng/mL resulted in a smaller value of S.D. when compared with 5000 and 50000 ng/mL of cTnT. It can be caused by the limited of binding receptors of cTnT antibody on quartz crystal surface at immobilization step from surface preparation. Furthermore, the higher level of cTnT concentration shown an increase of S.D., which was not related to the cTnT. It can be



caused by cTnT antigen which cannot be bound to antibody. Then it was removed by a rinse of PBS buffer .

**Table 4.4** Overview over Cardiac Troponin assays and the used method with the detection limit and the reference.

Assay	Assay Type	Specimen	Time (min)	Assay range
Stratus <sup>®</sup> CS STAT (Dade Behring Inc)	Bench top two- site Immunometric assay	Heparinised plasma	15	cTnI : 0.001-50 ng/mL
i-STAT <sup>®</sup> (Abbott)	Handheld two-site Immunometric assay	Whole blood or plasma	10	cTnI : 0.001-50 ng/mL
Triage Cardiac <sup>®</sup> Panel (Biosite)	Bench top two- site Flow-through immunometric assay	Plasma or EDTA whole blood	10-15	cTnI : 0.04-50 ng/mL
RAMP <sup>®</sup> (Response Biomedical Corp)	Bench top Lateral flow immunoassay	EDTA whole blood	8-15	cTnI : 0.03-32 ng/mL
Cardiac Reader <sup>™</sup> (Roche)	Bench top Lateral flow immunoassay	150 $\mu$ L heparinised whole blood	8 12	cTnT : 0.1-2 ng/mL
PATHFAST <sup>®</sup> (Mitsubishi Chemical Europe GmbH)	Bench top two- site Chemiluminescent analyzer	Whole blood or Heparin/EDTA/ citrate plasma	17	cTnI : 0.02-50 ng/mL

To increase the stability and reproducibility of the signal obtained from the binding experiments, the common additive Casein at a concentration of 0.1 % was added to the binding buffer. The cross linking of a low molecular weight protein such as Casein should increased the level of antigen binding to the antibody. It was the positive effects of Casein that had been shown in several studies [44]. However, the reproducibility and stability of the measurements were not increased. Moreover, the detection limit for cTnT was significantly increased due to the shift of 200 Hz for Casein.

**Table 4.5** Frequency shift related to cTnT concentration.

<b>Concentration (ng/mL)</b>	5	50	500	5000	50000
<b>Average Frequency shift (Hz)</b>	17	150	1,701	8,590	11,114
<b>S.D. (Hz)</b>	0.5018	5.2328	18.63237	327.8449	174.2099

An immunoassay using the reaction of antibodies to its antigen took advantage of the specific binding of an cTnT-antibody to cTnT. Monoclonal antibodies were used as they usually bound to one site of a particular molecule of cTnT. They therefore provided a more specific and accurate test, which were less easily confused by the presence of other molecules. The cTnT-antibodies can be delivered a high affinity for the cTnT-antigen.

Another parameter that was varied to increase the stability of the signals was the temperature during the measurements. It can result in positive as well as negative effects on binding experiments. However, for this study, an increase from 25°C up to 37°C had an adverse effect rather than a positive influence and the signal obtained was more unstable by protein degradable.

The increase of the longer injection time of 30 min did the result in higher baseline shifts and therefore more cTnT appeared to be bound to the surface. It can be resulted in a higher maximum relative response. However, the better results obtained from the experiments were disproportionate to the increase of consumption of cTnT. Moreover, the longer injection time were not agreed with the idea of a quick and simple analysis method.

### 4.3 Surface Enhanced Raman Spectroscopy Experiments

In this work, a method to fabricate highly sensitive, cost effective SERS substrates can be achieved. The magnetron sputtering system, which benefited from an easy adaptation to a large-scale production, was used to deposit silver nanoparticles on top of a thin anodic aluminum oxide (AAO) template. The presence of the AAO template, which had previously been fabricated by a simple anodizing process on a silicon substrate, aimed to increase the surface area and prevent coalescence of the deposited silver nanoparticles. By maintaining a high density of the silver nanoparticles deposited on the prepared substrates, a large SERS enhancement activity can now be obtained.

The structural details of the SERS substrates were further investigated by cross-sectional TEM images. One of the images had been selected and shown in Figure 4.8. The TEM image verified that the nanopores were completely opened from the aluminum top-surface down to the silicon substrate interface. In addition, the image revealed the prepared silver nanoparticles which embedded on the bottom of the nanochannels and on the top of the AAO surface. The TEM image also indicated the difference in size distribution between the nanoparticles embedded on each layer. The silver nanoparticles on the bottom of the nanochannels ranged between 10 to 20 nm in size, while those on the top of the AAO ranged between 20 to 30 nm in size. The size difference was most likely due to a shadowing effect of sputtered material between these two locations [50-51, 54].

### 4.3.1 Physical characteristics of SERS substrates

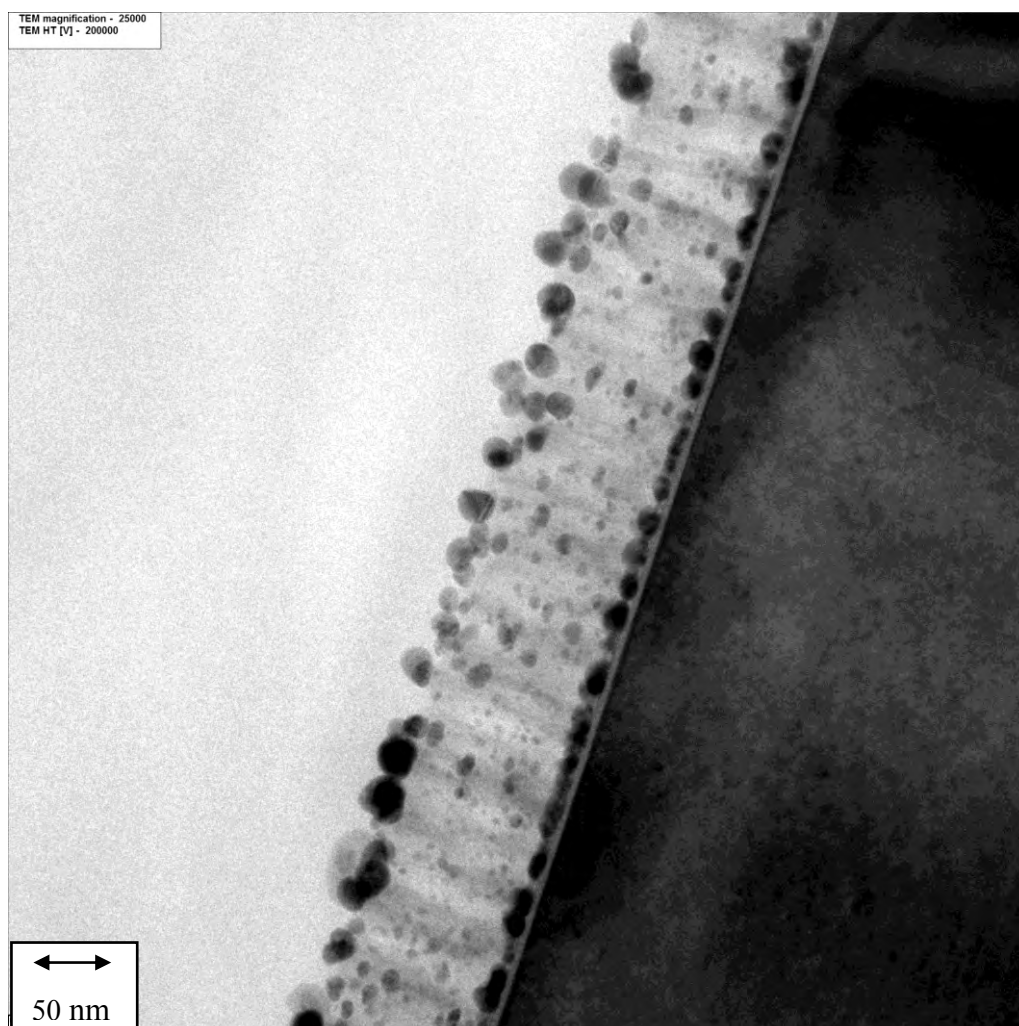


**Figure 4.8** Cross-sectional TEM images of the SERS substrates with the silver nanoparticles deposited by the magnetron sputtering for 8 seconds on AAO template.

The Figure 4.9 (a) and (b) show a uniform nanopore array with a pore size distribution between 30 and 40 nm, and an interpore distance around 80 to 100 nm. The silver nanoparticles with the diameter size around 10-30 nm were observed both on the inside and outside of the AAO nanochannels. The density of the silver nanoparticles on this particular sample was about half of the nanopore array at

approximately  $1 \times 10^{10} \text{ cm}^{-2}$ . Without the AAO template, these nanoparticles migrated along the substrate surface and coalesced to form a larger island. The coalescence resulted in the decrease in the density and the surface area of silver nanoparticles that can be bounded by the probing molecules. The coalescence hence reduced the coupling effect between the silver nanoparticles and degraded the Raman enhancement factor.

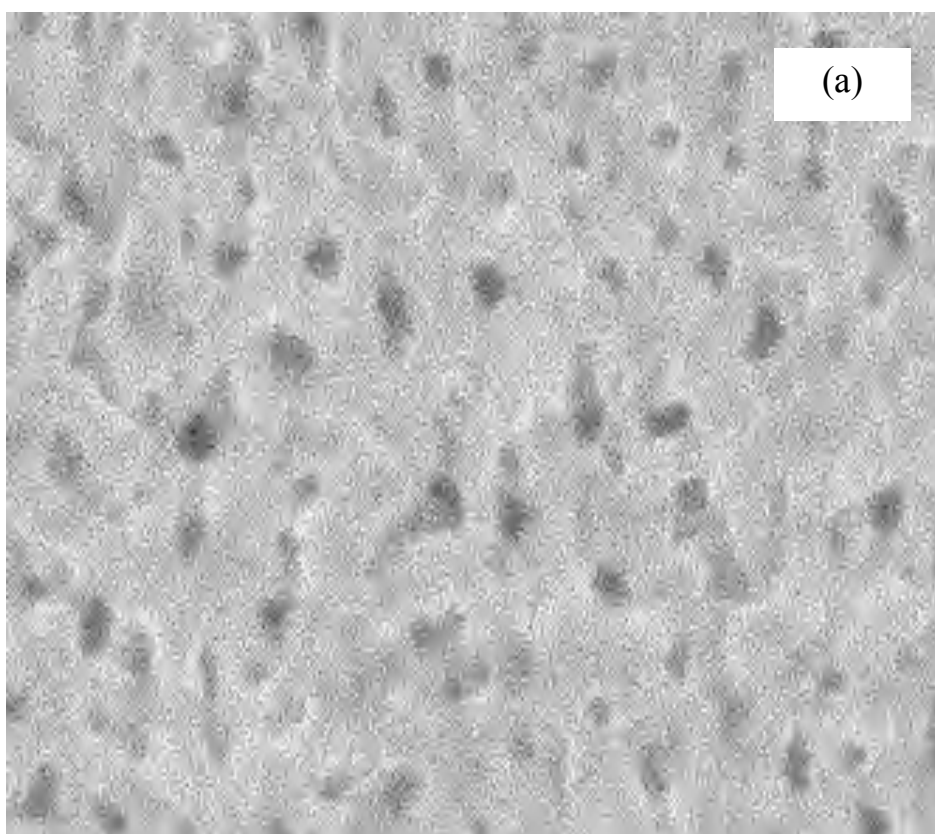


**Figure 4.9** (a) SEM images of the surface topology of the anodized aluminum before etching.

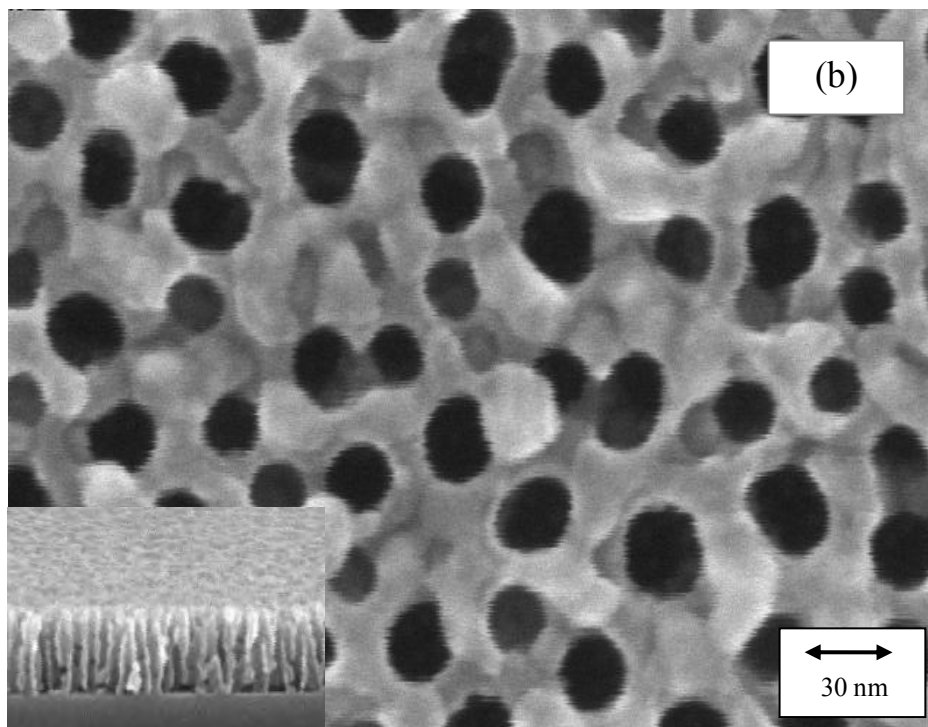


**Figure 4.9 (b)** SEM images of the surface topology of the anodized aluminum after 30 minutes of H<sub>3</sub>PO<sub>4</sub> etching.

Figure 4.9(a) shows the surface topology of the aluminum film after the anodization for 15 minutes. It can be seen a large fraction of aluminum film which was transformed into Al<sub>2</sub>O<sub>3</sub> shallow nanoholes with the diameter of 10 nm. The compound of Al<sub>2</sub>O<sub>3</sub> was dissolved from the obtained sample in 5 wt % H<sub>3</sub>PO<sub>4</sub> for 30 minutes to widen up the pore size. An increase of the pore size can be observed in Figures 4.9(b) which illustrated the nanoholes with diameter of 30-40 nm on the aluminum surface. A small figure in Figure 4.9(b) shown a cross-sectional image. It can suggest that the pore was completely opened from the top surface of the aluminum film to the silicon substrate interface. From a simple calculation, the density of the nanoholes in the fabricated AAO template was approximately  $2 \times 10^{10}$  cm<sup>-2</sup>.

After fabrication of the AAO template on the silicon wafer with the optimized conditions, the silver nanoparticles were deposited for 8 and 16 seconds on the prepared template. The SEM images for the surface topology of the deposited samples were illustrated in Figure 4.10. In Figure 4.10(a), the deposition for 8 seconds resulted in the silver nanoparticles with a diameter size of 10-30 nm clearly observed inside the pore of the AAO template. With a filling probability of approximately 50 percents, the density of the embedded silver nanoparticles inside the nanopores was approximately  $1 \times 10^{10} \text{ cm}^{-2}$ . For the deposition time of 16 seconds, a narrower pore size was observed in Figure 4.9(b) when compared with Figure 4.10(a). Figure 4.10(b) also indicated an observable coalescence of silver nanoparticles along the sidewalls and the top of the AAO template. For a pictorial description, the schematic of the silver nanoparticles deposited on the AAO template was illustrated in Figure 4.11. The Figure depicted the early stage of the sputter deposition, where the silver nanoparticles filled both inside the nanopores and on top of their sidewalls.

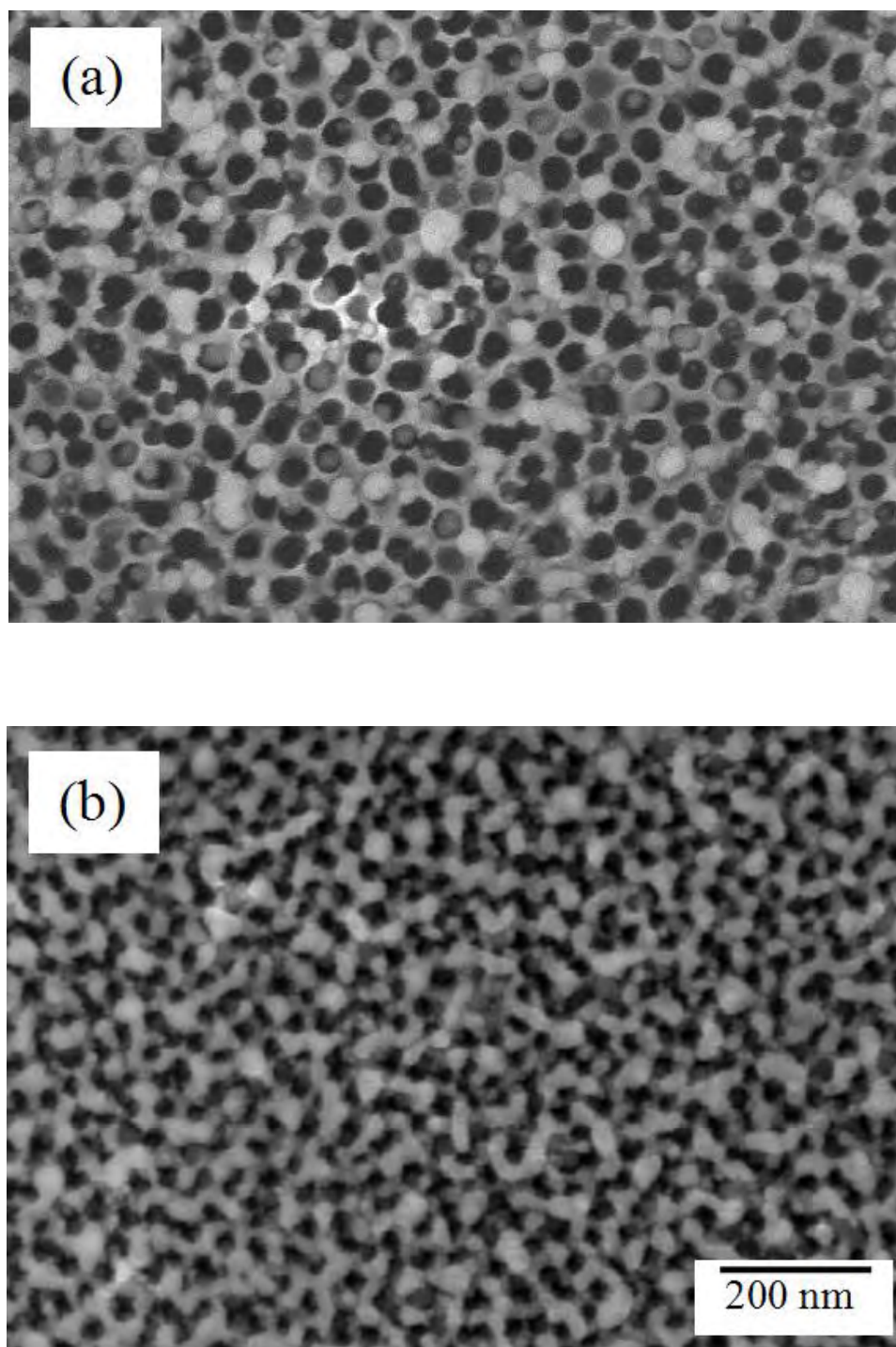


**Figure 4.10** SEM images of the surface topology of the SERS substrates with the silver nanoparticles deposited on the AAO template for (a) 8 seconds, and (b) 16 seconds.



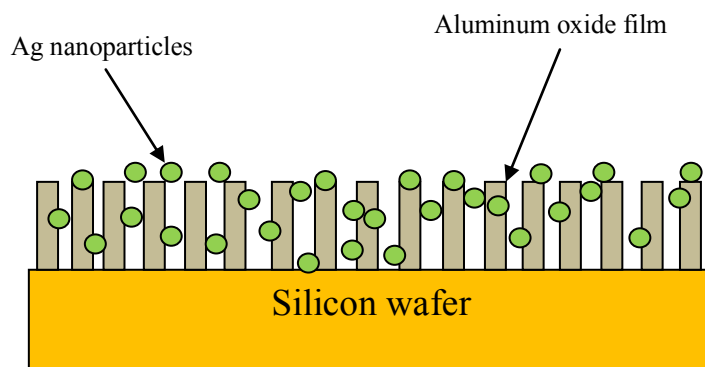


**Figure 4.11** Schematic of the silver nanoparticles deposited on the AAO template previously fabricated on top of the silicon wafer.

For comparison, a similar process for preparing the previous mentioned silver nanoparticles was conducted on the blank silicon wafers without the AAO template. The SEM images for the surface topology of these deposited samples were illustrated in Figure 4.12. Without the AAO-template layers, the nanoparticles deposited for 8 seconds appeared to migrate along the substrate surface and coalesce to form a larger island as shown in Figure 4.12(a). The coalescence of Ag clusters resulted in the decrease in the density and the surface area of the silver nanoparticles that can be bounded to an analyzed molecule. For the deposition time of 16 seconds, the silver nanoparticles began to form crystallites which appeared as sharp-edge grain boundaries as shown in Figure 4.12(b). The crystalline formation of the silver film from the Figure had been confirmed by x-ray diffraction in a glancing incident mode. The coalescence and the crystallization of the smoother surface resulted in the reduction of the silver surface area that can deteriorate the electromagnetic coupling effect between the silver nanoparticles.

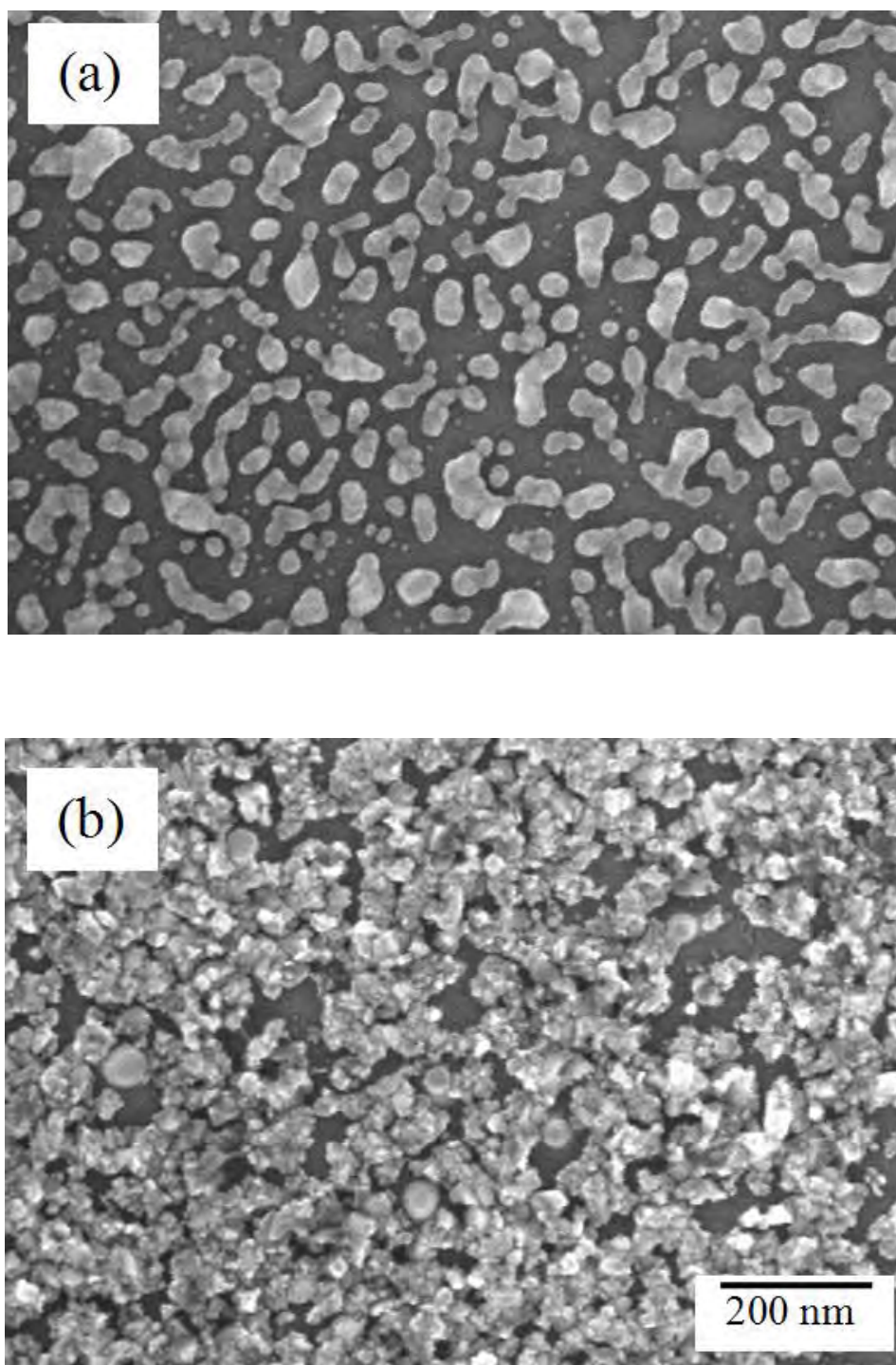


**Figure 4.12** SEM images of the surface topology of the substrates with the silver nanoparticles deposited on the blank silicon wafers for (a) 8 seconds, and (b) 16 seconds.

With several types of Raman-active substrates available, their Raman sensitivity with tiny droplets of the MB solution was first examined. The Raman spectra of MB adsorbed on the different SERS substrates were presented in Figure 4.13. Spectrum (a) indicated the Raman spectrum of MB adsorbed on the blank silicon substrate without the SERS structure. The peak at  $520\text{ cm}^{-1}$  corresponded to the typical Raman shift of the crystalline silicon substrate. From this spectrum, the Raman scattering intensity originated from MB adsorbed on this type of surface was not strong enough to be observed. Spectrum (b) presented the Raman spectral intensity of MB adsorbed on the blank AAO, which increased a broad spectrum for the silicon peak. This broad-spectral region was most likely a result of interactions between MB and the AAO nanopores due to the increase of surface area combined with the capillary effect. The combination eventually led to an increase in the background scattering. Spectra (c) and (d) presented the effects of the silver nanoparticles coated for 16 and 8 seconds, respectively, on the silicon substrate surfaces without the AAO templates. These substrates contained with the silver nanoparticles promoted some characteristic Raman peaks of MB to become visible. The results indicated the enhancement activity from the silver nanoparticles although they were deposited on the smooth surface. The Raman intensity of the spectrum (c) can be seen in the half of the spectrum (d) indicated that the coalescence of the silver nanoparticles was an important factor that limited the Raman enhancement of these prepared substrates. Next, spectra (e) and (f) shown the spectral Raman intensities of the prepared SERS substrates which consisted of the silver nanoparticles, deposited at 16 and 8 seconds, respectively, in the AAO templates. The spectrum (e) verified that the SERS substrate prepared with 8 seconds of the silver deposition on the AAO

template yielded the maximum SERS enhancement factor as a result of a high density of an isolate silver nanoparticle as discussed above.

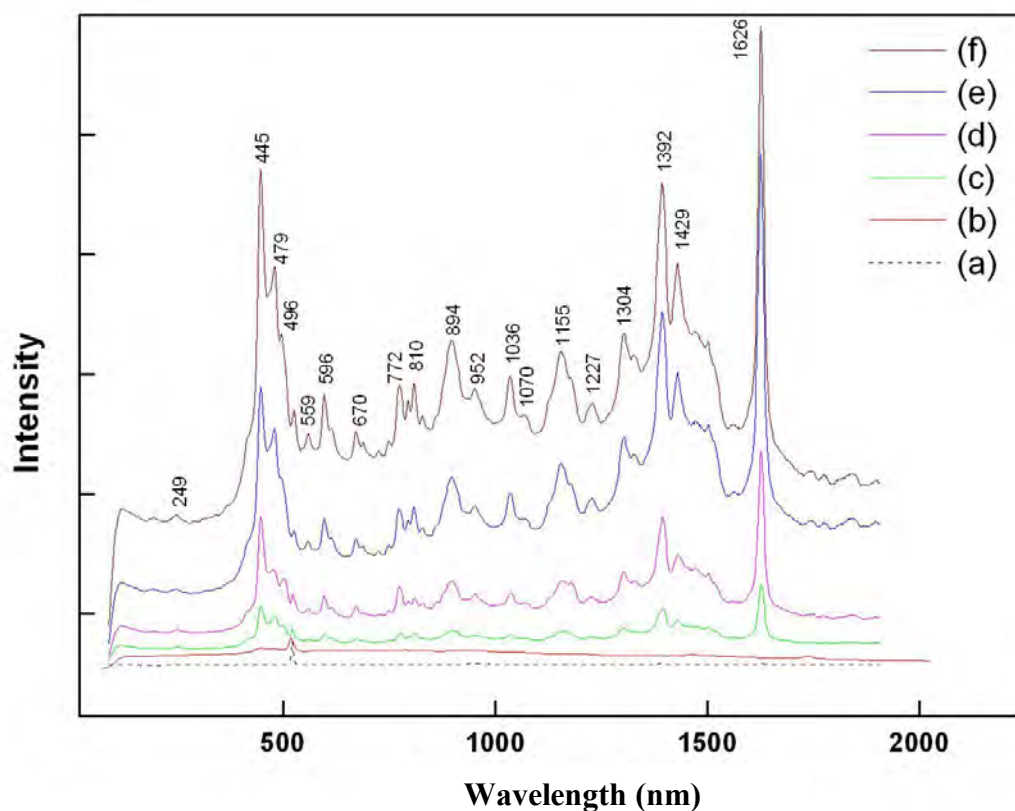


**Figure 4.13** Raman spectra of dried methylene blue droplets on several types of the sample surfaces: (a) blank silicon surface, (b) blank AAO template on Si, (c) 16 seconds silver nanoparticles deposited on Si, (d) 8 seconds silver nanoparticles deposited on Si, (e) 16 seconds silver nanoparticles deposited on AAO template, and (f) 8 seconds silver nanoparticles deposited on AAO template.

The SERS spectrum from this sample also revealed several molecular details of MB adsorbed on the SERS substrate. For example, the peak at  $249\text{ cm}^{-1}$  was originated from the Silver-N stretching of the Silver-(MB) complex [59-60]. This peak cannot be observed in normal Raman spectra measured from the other types of the prepared substrates. In addition, two main characteristic peaks of MB at 445 and  $1626\text{ cm}^{-1}$  corresponded to the C-N-C skeleton bending and the C-C stretching, respectively [59, 61, 74]. The relatively strong intensity and the sharp details of these peaks indicated that the MB molecules were tightly adsorbed on the SERS surface. The final results were the highly enhanced Raman signal. Apart from the aforementioned Raman peaks, the other band assignments for the MB molecular structures were summarized in Table 4.6. It can be seen that all assigned bands were in good agreement with the references [61, 74-75], although the bands without proper assignments at  $894$  and  $1304\text{ cm}^{-1}$  were also reported in the previous study by another group [59].

To confirm the SERS activity of the optimized SERS substrates, the pyridine was used as the other probing molecules because they were less sensitive than the MB molecules. The intense spectrum of pyridine adsorbed on the optimized SERS substrate can be observed as shown in Figure 4.14. This spectrum had shown the molecular details that resembled previously reported SERS spectra which was obtained from silver colloids [77-78] and indicated a highly effective SERS enhancement. The broad peak at around  $235\text{ cm}^{-1}$  can again be assigned to the stretching mode of the Silver-N bond. The most intense bands in the spectrum at  $1005$  and  $1021\text{ cm}^{-1}$  corresponded to a symmetric ring breathing mode and a trigonal ring breathing mode, respectively.

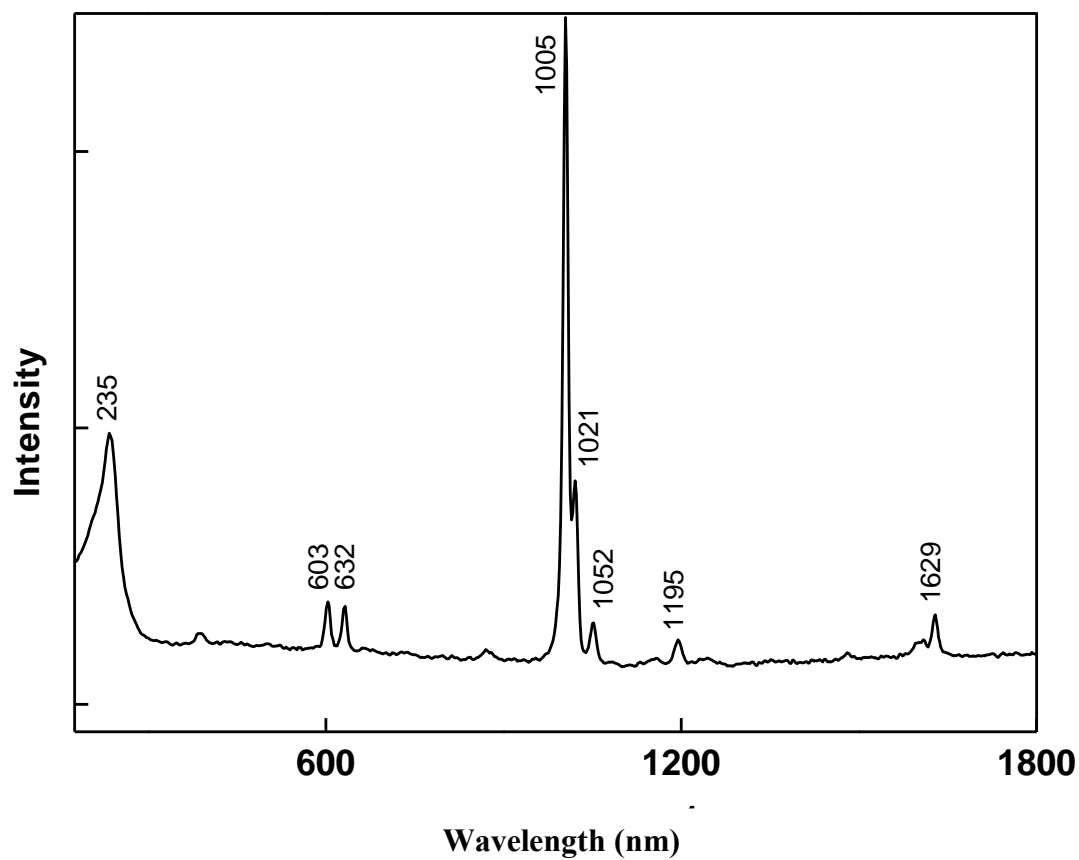


**Figure 4.14** Raman spectrum of dried droplets of a solution of  $1 \times 10^{-3}$  M pyridine and  $5 \times 10^{-2}$  M HCl on the SERS substrate with 8 seconds silver nanoparticles deposited on the AAO template. The bottom spectrum indicates Raman intensity on blank Si surface.

### 4.3.2 Calculation of Raman enhancement factors

The observed Methylene Blue (MB) band positions as a reference sample were in general agreement with the previously published results [74-79]. For quantitative comparison, the Raman enhancement factor is used to define the ratio of the elastic scattering intensity per molecule between the presence and the absence of SERS. The Raman enhancement factor is written as [60-61, 74-77].

$$G = \frac{I_{SERS}}{I_{Ref}} \times \frac{N_{Ref}}{N_{SERS}} \quad (4.5)$$

In this formula,  $I_{SERS}$  is the enhanced intensity of the adsorbed molecules on the SERS substrate.  $I_{Ref}$  is the spontaneous Raman scattering intensity from the bulk molecules under the laser spot on the blank Si substrate.  $N_{Ref}$  is defined as the number of the bulk molecules excited by the laser without Raman enhancement effect. For a scattering volume of  $1000 \mu\text{m}^3$ ,  $N_{Ref}$  is approximately  $3.3 \times 10^{11}$  molecules.  $N_{SERS}$  is the number of molecules uniformly spreading on SERS substrate under laser spot. Using a 100x objective lens, the area of laser spot is around  $1 \mu\text{m}^2$  with laser power at 50 mWatt. As the maximum SERS intensity was obtained from cTnT at concentration of  $5 \times 10^{-6}$  g/mL, which was corresponding to  $10^4$  monolayers of MB, the value of  $N_{SERS}$  under laser excitation is therefore  $5 \times 10^9$  molecules. A monolayer of molecules was assumed for the value of  $N_{SERS}$  as reported previously [77-78], the enhancement factor of these SERS was on the order of  $10^8$ . However, there was still no consensus that the SERS signal mainly arose from a single molecule layer covering on nanoparticle array.

Finally, the Raman enhancement factor from the spectra was calculated and shown in Figure 4.13. The enhancement factor was defined as the ratio of inelastic scattering intensity per molecule between the presence and absence of the SERS structure. The Raman enhancement factor can be written as [59-60, 78].

$$G = \frac{I_{\text{SERS}}}{I_{\text{Ref}}} \cdot \frac{N_{\text{Ref}}}{N_{\text{SERS}}}. \quad (4.6)$$

$I_{\text{SERS}}$  was the enhanced intensity of the adsorbed MB molecules on the SERS substrate. The value of  $I_{\text{SERS}}$  mainly arose from a single molecule layer covering a nanoparticle array, from which other additional molecules layers of analyzed molecules on the SERS substrate, as previously reported [59], did not contribute in Raman gain and can be neglected.  $I_{\text{Ref}}$  was the spontaneous Raman scattering intensity from the bulk MB molecules under the laser spot on the blank silicon substrate.  $N_{\text{SERS}}$  was the number of the single-layer molecules covering the SERS substrate under the laser spot.  $N_{\text{Ref}}$  was the number of the bulk molecules excited by laser on the surface of the regular substrate.



**Table 4.6 Band assignments and enhancement factors calculated from SERS spectra c-f plotted in Figure 4.12.**

<b>Band assigne</b>	$\delta(\text{C-N-C})$	$\delta(\text{C-S-C})$	N/A	$\beta(\text{C-H})$	$\nu(\text{C-N})$	N/A	$\alpha(\text{C-H})$	$\nu_{\text{asym}}(\text{C-N})$	$\nu(\text{C-C})$ ring	Average
<b>Raman shift</b> ( $\text{cm}^{-1}$ )	445	612	894	1036	1155	1304	1392	1429	1626	
	c	$8.9 \times 10^6$	$1.1 \times 10^7$	$8.7 \times 10^6$	$1.1 \times 10^7$	$9.1 \times 10^6$	$9.0 \times 10^6$	$1.2 \times 10^7$	$7.4 \times 10^6$	$9.4 \times 10^6$
<b>G factor</b>	d	$2.3 \times 10^7$	$2.5 \times 10^7$	$2.1 \times 10^7$	$2.6 \times 10^7$	$2.3 \times 10^7$	$2.1 \times 10^7$	$2.9 \times 10^7$	$2.0 \times 10^7$	$2.3 \times 10^7$
	e	$4.2 \times 10^7$	$5.3 \times 10^7$	$4.7 \times 10^7$	$6.3 \times 10^7$	$5.6 \times 10^7$	$5.6 \times 10^7$	$7.7 \times 10^7$	$4.7 \times 10^7$	$5.5 \times 10^7$
	f	$7.6 \times 10^7$	$9.8 \times 10^7$	$8.1 \times 10^7$	$1.1 \times 10^8$	$8.7 \times 10^7$	$8.2 \times 10^7$	$6.8 \times 10^7$	$1.1 \times 10^7$	$5.8 \times 10^7$

Data reference from K. Wong-ek et al. [58]

In order to obtain the values of these four parameters, the same procedures were followed which based on the published literatures [59-60, 77]. The area of the laser spot size at around  $1 \mu\text{m}^2$  was determined by using the 100x objective lens. The area of a single molecule of MB was also calculated to be approximately  $2 \text{ nm}^2$  [78-79]. Thus, the value of  $N_{\text{SERS}}$  under the laser excitation was approximately  $5 \times 10^5$  molecules. To assume a uniform distribution of MB over the droplet area of  $2 \text{ mm}^2$ , the value of  $N_{\text{Ref}}$  was approximately  $7.5 \times 10^{10}$  molecules. Therefore, from Equation (4.5), the enhancement factor G was simply  $(1.5 \times 10^5) \times (I_{\text{SERS}}/I_{\text{Ref}})$ . The enhancement factors of each assigned Raman peak as measured from different SERS substrates were also shown in Table 4.6. The results were shown that the highest enhancement factor can be achieved at the average value of  $8.5 \times 10^7$  from the spectrum (f), which obtained from the optimized SERS substrate.

#### 4.4 cTnT detections on the SERS substrates.

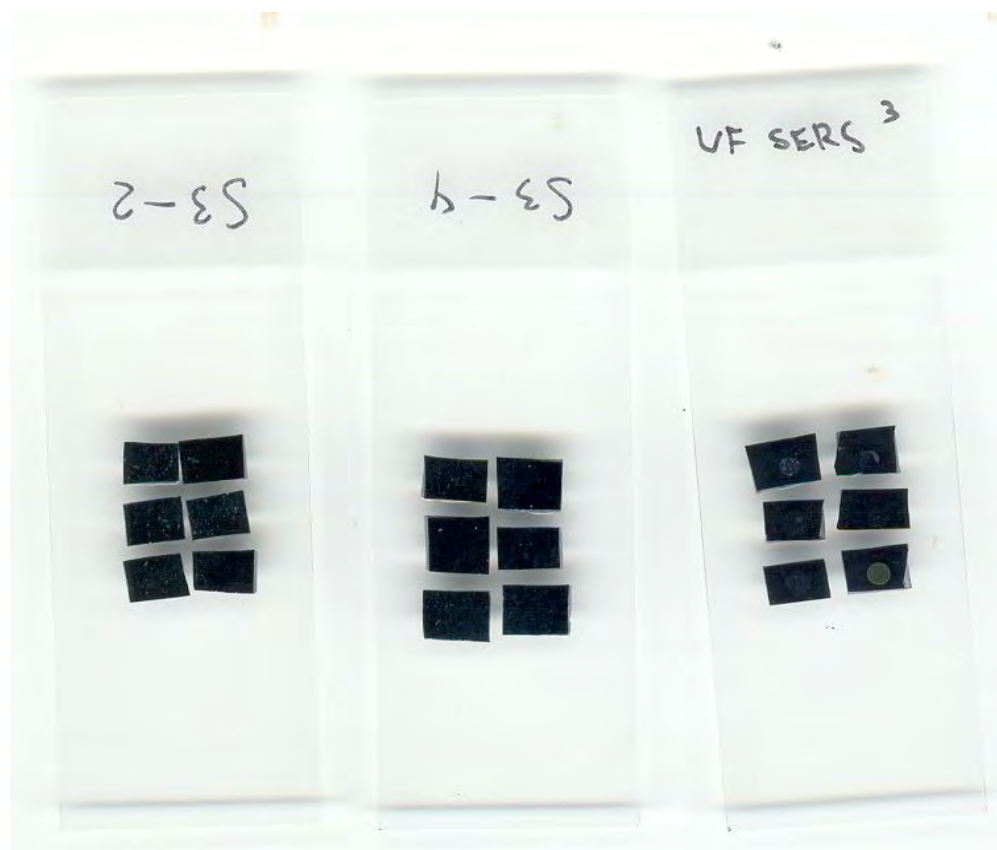


**Figure 4.15** Illustration of the Developed SERS substrates.

Two types of aqueous solution, Methylene Blue (MB) and Pyridine, were used to provide probing molecules in order to evaluate SERS activities of the fabricated SERS substrates. The analyzed molecules were conducted with cTnT in several concentrations. The developed SERS substrates which were deposited on glass slides demonstrated in Figure 4.15.

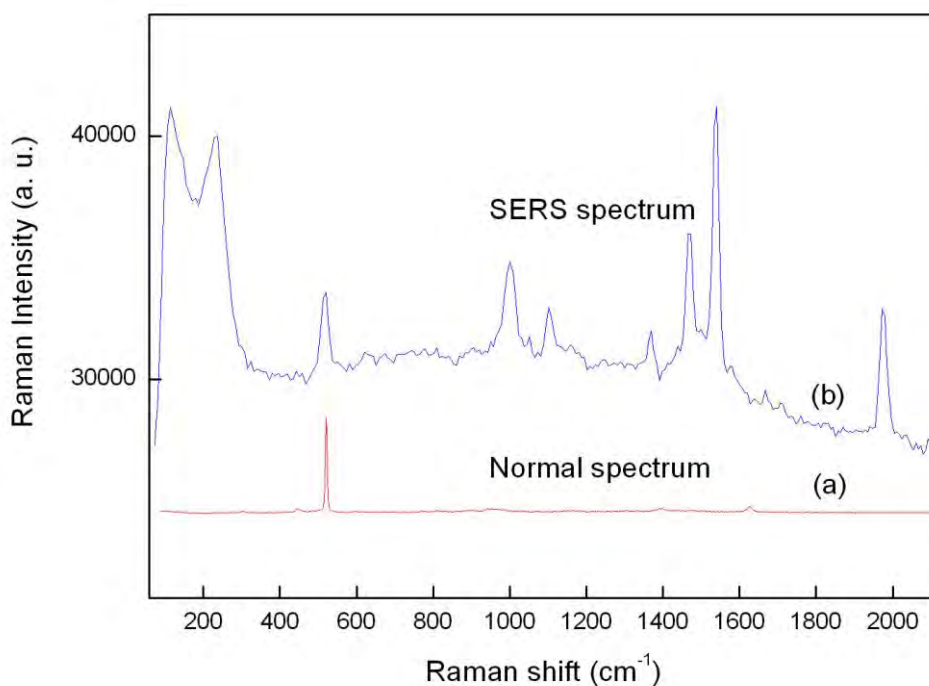


**Figure 4.16** Raman spectra of the cTnT droplets at the concentration of 50 ng/mL as left dried on (a) the Si substrate, and (b) the silver nanoparticles deposited on the AAO template.

The normal Raman spectrum of solid cTnT molecules which were adsorbed on the silicon substrate without the SERS structure was shown in spectrum 4.16(a). The peak at  $520\text{ cm}^{-1}$  corresponded to the Raman scattering of the crystalline Si substrate. The spectrum indicated that the Raman signal of cTnT on the normal substrate can be not strong enough to be observed due to small amount of Raman scattering from the material which was deposited on the Si surface. Spectrum 4.16(b) presented the enhancement effect on the Raman scattering of the silver nanoparticles coated directly on the silicon wafer. With this sample, characteristic Raman peaks of cTnT at concentration of 50 ng/mL became visible which indicated enhancement

activity from the silver nanoparticles. For the SERS substrate with the silver nanoparticles embedded in the AAO template, the Raman intensities increased drastically as shown in Figure 4.16(b). This plot suggested that the coalescence of the silver nanoparticles was an important factor that limited the Raman enhancement factor of these substrates. It can show that the presence of nanochannels can increase the surface area for the deposition of the silver nanoparticles and suppress the coalescence. This deposition method resulted in further enhancement of the SERS intensities and thus allowed the SERS substrates to reveal several molecular details of the cTnT molecules which were adsorbed on their surface.

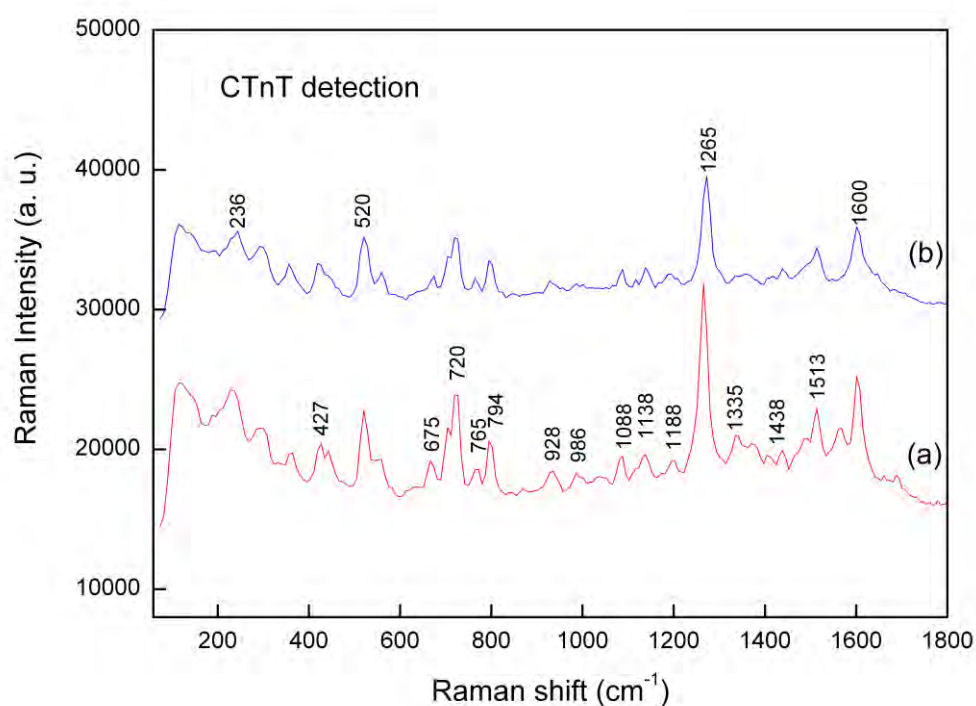


**Figure 4.17** Raman spectra of the cTnT droplets at the concentration of 5  $\mu\text{g/mL}$  as left dried on the silver nanoparticles deposited on the Si substrate at (a) partially dried, and (b) completely dried.

The Raman spectra of cTnT at the concentration of 5  $\mu\text{g/mL}$  on the different time of absorption onto the substrates were presented in Figure 4.17. The solution which partially dried cTnT had more details of vibration on Raman spectra than completely dried solution. However, it can also show the Raman spectra in related shift. Since the main absorption peaks of cTnT solution were located at 675 which was from beta sheet, 720 was from adenine which was part of amino acid residues. The bond of carbon atom between molecules and the amide bond were 928 and 1265, respectively, which were both compound of beta sheet and alpha helix of protein molecules. The peak of water band was 1600 nm and other peaks at 1068 and 1138 were from buffer. The results of spectral peak were shown that the resonant Raman effect from the excitation wavelength can partially improve the Raman intensities. However, this resonant effect was expected to be smaller than results from the SERS effect.

Figure 4.18 shows the Raman spectra of cTnT with the concentrations varied from 5  $\mu\text{g/mL}$ , 500  $\text{ng/mL}$ , 50  $\text{ng/mL}$ , to 5  $\text{ng/mL}$  and PBS buffer on the fabricated SERS substrate. One of the interesting features that should be pointed out was the comparison in the SERS intensities between cTnT with the concentrations of 5  $\mu\text{g/mL}$  and 5  $\text{ng/mL}$ . At this point, the SERS intensity was increase instead of decrease, with a decrease in the cTnT concentration. This was indicated that the enhanced Raman signal was generated only from a thin layer of analyzed molecules embedded close to the metal nanoparticles. Other additional layer of analyze molecules were weaken in the scattering signal, instead of strengthen.

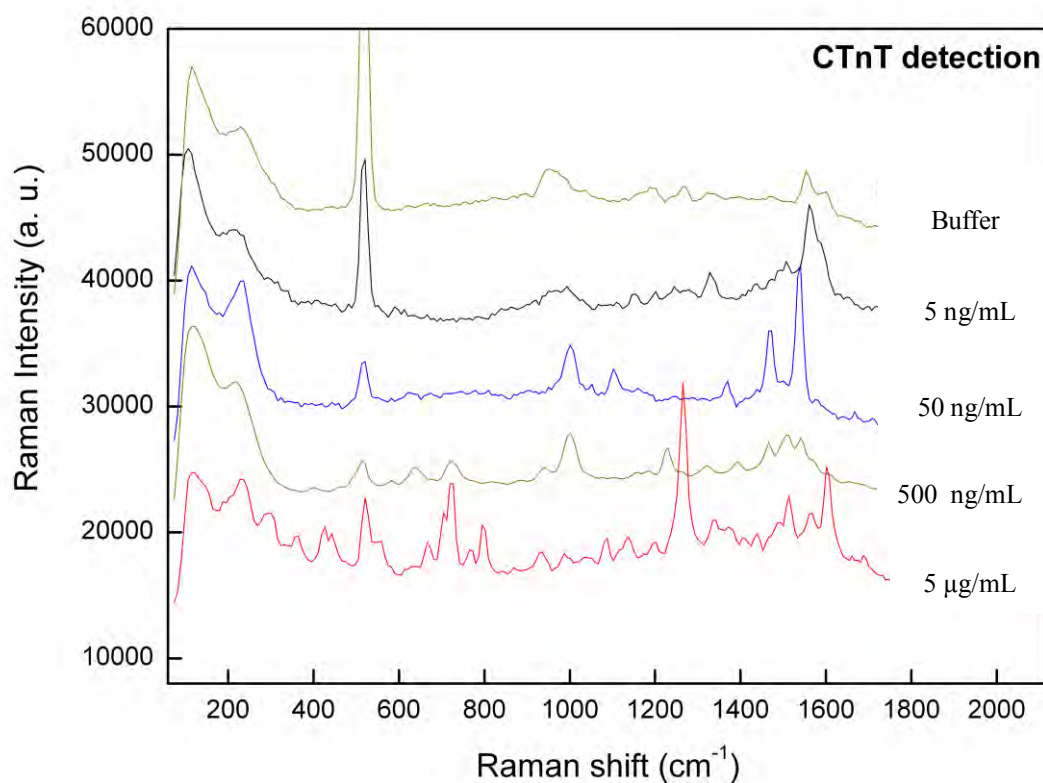


**Figure 4.18** Raman spectra of Buffer and cTnT with the concentrations varied from  $5 \times 10^{-6}$  g/mL to  $5 \times 10^{-9}$  g/mL on the fabricated SERS substrate.

The Raman scattering intensities were decrease at concentrations below 5  $\mu\text{g/mL}$ , which indicated reduction in cTnT monolayer film deposited on the SERS substrates. The Raman intensity almost disappeared for cTnT at 5 ng/mL concentration compared to the higher cTnT concentrations and buffer line. Figure 4.18 shows that some of cTnT band peaks can still be able to observe at this ultra low concentration. This result verified a high sensitivity of this fabricated SERS substrate.

# CHAPTER V

## CONCLUSIONS AND FUTURE PROSPECT

This dissertation investigated the development of biosensors and cTnT detection, based on QCM biosensors and SERS substrates, as discussed separately.

### 5.1 Quartz Crystal Microbalance Biosensors

In conclusion, a high sensitive cTnT detection method was developed by using a surface-modified QCM. The quartz surface of a commercial QCM was coated with a 200 nm thick PVC-COOH using the spray coating technique. To initiate surface capability of antibody-antigen binding complex, a flow injection system with attachments of cross linker reagents onto the modified quartz surface was also used. The PVC-COOH coated quartz surface demonstrated an effectiveness of cTnT detection. The frequency shift was found to be proportional to the cTnT concentrations. The sensitivity limit of the developed QCM system for the cTnT detection was 5 ng/ml with the noise level less than  $\pm 5$  Hz. The PVC-coated QCM was successfully reused to collect new experimental data up to three times without any loss of functionality and specificity for cTnT antibody.

From Chapter IV, the results of cTnT detection from developed QCM sensor shown that the cTnT antibody immobilization on a polymer coated quartz crystal surface provided a viable new method for the detection of cTnT. In comparison with other detection methods, such as ELISA or antibody-based biosensors, the developed cTnT-sensor offered a low detection limit at less than 5 ng/mL. Although, this



method provided a lower performance than commercially available and expensive automation system used in clinical diagnosis, the use of QCM in this technique was effectively advantageous at a short analysis times and low reagent consumption. To sum up, this new cTnT-sensor offered the possibility of the detection of cTnT with the disposable, low cost and reliable cTnT immunosensor, in addition to a quicker measurement in alternative screening analysis. However, the behavior of the new cTnT-sensor for the measurements of cTnT cannot be completely predicted and therefore required more experiments with serum samples. Other important factors also included the assay of precision, the sensitivity or matrix effects, and the standardization of more experiments. These factors led to the ultimate use of the new cTnT-sensor in a commercially available assay for clinical diagnostics. Nonetheless, development of the commercial quartz crystal microbalance (QCM) system offered a new opportunity to a rapid, low-cost and highly sensitive cTnT sensor. By combining QCM system with immunoassay method, the quantification of cTnT protein can be done within a short period of time and with a minimum amount of sample and reagent consumptions.

## **5.2 Surface Enhanced Raman Spectroscopy Substrates**

This part of the dissertation discussed the fabrication process of the low-cost and highly sensitive SERS substrates which were prepared by the deposition of the silver nanoparticles on the AAO templates based on the magnetron sputtering system as shown in Chapter III. Using the AAO templates, the coalescence of the silver nanoparticles can be suppressed, while without the AAO templates the silver

nanoparticles tend to gather in a highly clustered feature. The density of silver nanoparticles deposited on the SERS substrates can be optimized to be more than  $1 \times 10^{10} \text{ cm}^{-2}$ . The SERS substrates allowed an excellent observation of the cTnT molecular details and offered the enhancement factor more than  $1.71 \times 10^4$  by using cTnT in the experiment. In addition, the SERS substrates fabricated in this dissertation had detectability to cTnT at the ultra low concentration of  $10^{-9}$ . From Chapter IV, in part of cTnT detection by SERS, these results suggested that the developed SERS substrates were suitable to be used in applications of chemical detections and screening diagnosis. The cTnT spectra from SERS substrate and band assignment of cTnT protein indicated several peaks of vibrational mode. The plot showed bonding of amide (R-NH<sub>2</sub>), C-C stretching and C-H bonding spectra.

### **5.3 Future prospect**

The QCM and SERS techniques both have their own strengths for the development of cardiovascular marker detection biosensor for the detection of cTnT. SERS is most likely used in the development of new commercial sensors than QCM with the components device due to its simplicity in fabrication and inexpensive required materials. Due to the difficulties report in Chapter IV with the piezoelectric crystals, the SERS is used for the optimization process of the cTnT-binding surface. The nanochannel size and thickness of the AAO arrays are expected to optimize which would further increase the SERS enhancement factors. Since both involve direct affinity sensing on a silver surface, many parallels exist between the two approaches and methods developed are to a large extent transferable.

## REFERENCES

- [1] Joint European Society of Cardiology/American College of Cardiology Committee. Myocardial Infarction Redefined a Consensus Document of the Joint European Society of Cardiology/American College of Cardiology Committee for the Redefinition of Myocardial Infarction. J. Amer. Coll. Cardiol. 36 (2000): 959–68.
- [2] Amos, L. Structure of Muscle Filaments Studied by Electron Microscopy. Ann Rev. Biophys. Chem. 14 (1985): 291–313.
- [3] Dean, K. J. Biochemistry and Molecular Biology of Troponin I and T. Cardiac Markers. (1998).
- [4] Farah, C. S.; Reinach, F. C. The Troponin Complex and Regulation of Muscle Contraction. FASEB J. 9 (1995): 755–67.
- [5] Flicker, P. F.; Phillips Jr., G. N.; Cohen C. Troponin and its Interactions with Tropomyosin: An Electron Microscopic Study. J. Mol. Biol. 162 (1982): 495–501.
- [6] Katus, H. A.; Remppis, A.; Scheffold, T. K.; Diederich, W.; Kuebler, W. Intracellular Compartmentation of Cardiac Troponin T and its Release Kinetics in Patients with Reperfused and Nonreperfused Myocardial Infarction. Am. J. Cardiol. 67 (1991): 1360–1367.
- [7] Katus, H. A.; Scheffold, T.; Remppis, A.; Zehlein, J. Proteins of the Troponin Complex. Lab. Med. 23 (1992): 311–317.
- [8] Cook, R. The Mechanisms of Muscle Contraction. CRC Crit. Rev. Biochem. 21 (1986): 53–118.

- [9] Mair, J. Progress in Myocardial Damage Detection New Biochemical Markers for Clinicians. Crit. Rev. Clin. Lab. Sci. 34 (1997): 1–66.
- [10] Ebashi, S.; Wakabayashi, T.; Ebashi, F. Troponin and its Components. J. Biochem. (Tokyo) 69 (1971): 441–445.
- [11] Greaser, M.; Gergely, J. Purification and Properties of the Components from Troponin. J. Biol. Chem. 248 (1973): 2125–2133.
- [12] Flicker, P. F.; Phillips Jr., G. N.; Cohen, C. Troponin and its Interactions with Tropomyosin an Electron Microscopic Study. J. Mol. Biol. 162 (1982): 495–501.
- [13] Farah, C. S.; Reinach, F. C. The Troponin Complex and Regulation of Muscle Contraction. FASEB J. 9 (1995): 755–767.
- [14] Zot, A. S.; Potter, J. D. Structural Aspects of Troponin-Tropomyosin Regulation of Skeletal Muscle Contraction. Ann. Rev. Biophys. Chem. 16 (1987): 535–559.
- [15] Lodish, H.; Berk, A.; Zipursky, L.; Matsudaira, P.; Baltimore, D.; Darnell J. Molecular Cell Biology. 3<sup>rd</sup>ed, WH Freeman, New York, 1995.
- [16] Karczewski, P.; Bartel, S.; Krause, E.-G. Protein Phosphorylation in the Regulation of Cardiac Contractibility and Vascular Smooth Muscle Tone. Curr Opin Nephrol Hypertens 2 (1993): 33–40.
- [17] Kitsis, R. N.; Scheuer, J. Functional Significance of Alterations in Cardiac Contractile Protein Isoforms. Clin. Cardiol. 19 (1996): 9–18.
- [18] Venema, R. C.; Kao, J. F. Protein Kinase C Mediated Phosphorylation of Troponin I and C-Protein in Isolated Myocardial Cells is Associated with Inhibition of Myofibrillar Actinomysin Mg ATPase. J. Biol. Chem. 268

- (1993): 2705–2711.
- [19] Quirk, P. G.; Patchell, V. B.; Gao, Y. B.; Levine, A.; Perry S. V. Sequential Phosphorylation of Adjacent Serine Residues on the n-Terminal Region of Cardiac Troponin-I Structure Activity Implications of Ordered Phosphorylation. FEBS Lett. 370 (1995): 175–178.
- [20] Collinson, P. O.; Boa, F. G.; Gaze, D. C. Measurement of Cardiac Troponins. Ann. Clin. Biochem. 38(2001): 423–49.
- [21] Jaffe, A.S.; Ravkilde, J.; Roberts, R.; Naslund, U.; Apple, F.S.; Galvani, M.; Katus, H. It's time for a change to a troponin standard. Circulation 102 (2000) 1216-1220.
- [22] Tunstall-Pedoe, H.; Kuulasmaa, K.; Amouyel, P.; Arveiler, D.; Rajakangas, A.M.; Pajak, A. Myocardial infarction and coronary deaths in the World Health Organization MONICA Project. Circulation 90 (1994): 583-612.
- [23] Apple, F.S.; Wu, A.H.B. Myocardial Infarction Redefined: Role of Cardiac Troponin Testing. Clin. Chem. 47 (2001): 377–379.
- [24] Katus, H.A.; Remppis, A.; Looser, S.; Hallermeier, K.; Scheffold, T.; Kubler, W. Enzyme linked immuno assay of cardiac troponin T for the detection of acute myocardial infarction in patients. Mol. Cell. Cardiol. 21 (1989): 1349–1353.
- [25] Muller, B.M.; Hallermayer, K.; Schröder, A.A. Improved troponin T ELISA specific for cardiac troponin T isoforms assay development and analytical and clinical validation. Clin. Chem. 43 (1997): 458–466.
- [26] Cummins, B.; Auckland, M.L.; Cummins, P. Cardiac-specific troponin-I radioimmunoassay in the diagnosis of acute myocardial infarction. Am.

- Heart J. 113 (1987): 1333–1344.
- [27] Reimhult, K.; Yoshimatsu, K.; Risveden, K.; Chen, S.; Ye, L.; Krozer, A. Cardiac-specific troponin-I radioimmunoassay in the diagnosis of acute myocardial infarction. Biosens. Bioelectron. 23 (2008): 1908–1914.
- [28] Katus, H.A.; Remppis, A.; Neumann, F.J.; Scheffold, T.; Diederich, K.W.; Vinar, G.; Noe, A.; Matern G.; Kuebler, W. Diagnostic efficiency of troponin T measurements in acute myocardial. Circulation 83 (1991): 902-912.
- [29] Lu, Q.W.; Morimoto, S.; Harada, K.; Du, C.K.; Yanaga, F. T.; Miwa, Y.; Sasaguri, T.; Ohtsuki, I. Cardiac troponin T mutation found in dilated cardiomyopathy stabilizes the troponin T-tropomyosin interaction and causes Ca<sup>2+</sup> desensitization. J. Mol. Cell. Cardiol. 35 (2003): 1421–1427.
- [30] Rabe, J.; Buttgenbach, S.; Schroder, J.; Hauptmann, P. Monolithic miniaturized quartz microbalance array and its application to chemical sensor systems for liquids. IEEE Sensors J. 3 (2003): 361 – 368.
- [31] Dirk, S.; Lieven, H.; Kristien, B.; Serge M. Antibody Fragments as Probe in Biosensor Development. Sensors 8 (2008): 4669-4686.
- [32] Surugiu, I.; Danielsson, B.; Ye, L.; Mosbach, K.; Haupt, K. Chemiluminescence imaging ELISA using an imprinted polymer as the recognition element instead of an antibody. Anal. Chem. 73, (2001): 487–491.
- [33] Koshets, I.A.; Kazantseva, Z.I.; Shirshov, Yu. M. Polymer films as sensitive coatings for quartz crystal microbalance sensors array. Semiconductor Physics Quantum Electronics & Optoelectronics. 6 (2003): 505-507.
- [34] Jimenez, Y.; Fernandez, R.; Torres, R.; Arnau, A. A contribution to solve the

- problem of coating properties extraction in quartz crystal microbalance applications. IEEE Transactions on Ultrasonics, Ferroelectrics, and Frequency Control. 53 (2006): 1057 – 1072.
- [35] Pengchao, S.; Mortensen, J.; Komolov, A.; Denborg, J.; Moller, P.J. Polymer coated quartz crystal microbalance sensors for detection of volatile organic compounds in gas mixtures. Anal. Chimica Acta. 597 (2007): 223-230.
- [36] Rebecca, C. W. L.; Martin, M. F. C.; Jianzhong, L. Alcohol sensing membrane based on immobilized ruthenium (II) complex in carboxylated PVC and surface covalently bonded alcohol oxidase. Talanta 48 (1999): 321-331.
- [37] Ming, H. P.; Hui, B. N.; Md, A. R.; Mi, S. W.; Yoon, B. S. Label-Free Detection of Bisphenol A Using a Potentiometric Immunosensor. Electroanalysis 20 (2007): 30-37.
- [38] Sylvia, D.; Leonidas, G. B. Ion-selective electrodes using an ionophore covalently attached to carboxylated poly (vinyl chloride). Analyst 133(5) (2008): 635-642.
- [39] Oi-wah, L.; Bing, S.; Wuming, Z. Evaluation of methods to minimize effects of liquid viscosity and density on the oscillating frequencies of thickness-shear-mode (TSM) piezoelectric resonators. Analytica Chimica Acta 312(2) (1995): 217-222.
- [40] Liu, Y.C.; Wang, C.M.; Hsiung, K.P. Comparison of different protein immobilization methods on quartz crystal microbalance surface in flow injection immunoassay. Anal. Biochem. 299 (2001): 130-135.
- [41] Sabina, S.; Rosanna, T.; Andrea, P.; Nicolò, D.; Gino, B. A piezoelectric

- immunosensor based on antibody entrapment within a non-totally rigid polymeric film. Sensors and Actuators B: Chemical 111 (2005): 331-338.
- [42] Monika, M.; Ralph, W.; Stephanus, B. Miniaturized QCM-based flow system for immunosensor application in liquid. Sensors and Actuators B: Chemical 111 (2005): 410-415.
- [43] Xiao-Li, S.; Yanbin, L. A QCM immunosensor for Salmonella detection with simultaneous measurements of resonant frequency and motional resistance. Biosens. and Bioelectron. 21 (2005) 840–848.
- [44] Shigeru K.; Miki, N.; Jong-Won, P.; Hidenobu, A.; Kazunori, Y.; Mitsuo, H. Evaluation of a high-affinity QCM immunosensor using antibody fragmentation and 2-methacryloyloxyethyl phosphorylcholine (MPC) polymer. Biosens. and Bioelectron. 20 (2004) 1134–1139.
- [45] Qun-Wei, L. Cardiac troponin T mutation R141W found in dilated cardiomyopathy stabilizes the troponin T–tropomyosin interaction and causes a Ca<sup>2+</sup> desensitization. Journal of Molecular and Cellular Cardiology 35(2003): 1421-1427.
- [46] Fang, J.; Yi, Y.; Din, B.; Song, X. Resonant Raman Scattering of Coherent Picosecond Pulses by One and Two on Si (111) Substrate. Appl. Phys. Lett. 92 (2008):1311-1315.
- [47] Yan, F.; Vo-Dinh, T. Surface-enhanced Raman scattering detection of chemical and biological agents using a portable Raman integrated tunable sensor. Sensor and Actuators B 121 (2007): 61.
- [48] Liu, GL.; Lee, L. P. Fabrication and characterization of electrostatic Si/SiGe quantum dots with an integrated read-out channel. Appl. Phys. Lett. 87



(2005): 1074-1101.

- [49] Alexander, T.; Le, D.M. Confocal Raman Microscopy of Optical-Trapped Particles in Liquids. Apply Optics 46 (2007): 38-78.
- [50] Suzuki, M.; Maekita, W.; Wada, Y.; Nakajima, K.; Kimura, K.; Fukuoka, T. et al. Ag nanorod arrays tailored for surface-enhanced Raman imaging in the near-infrared region. Appl Phys. Lett. 88 (2006): 2031-2135.
- [51] Ruan, C.; Eres, G.; Wang, W.; Zhang, Z.; Gu, B. Controlled Fabrication of Nanopillar Arrays as Active Substrates for Surface-Enhanced Raman Spectroscopy. Langmuir 23 (2007): 5757-5760.
- [52] Gu, G. H.; Kim, J.; Kim, L.; Suh, J. S. Discrete Dipole Approximation Calculations of Optical Properties of Silver Nanorod Arrays in Porous Anodic Alumina. J. Phys. Chem. C 111 (2007): 7906.
- [53] Lombardi, I.; Cavallotti, PL.; Carraro, C.; Maboudian, R. Template assisted deposition of Ag nanoparticle arrays for surface-enhanced Raman scattering applications. Sensor and Actuators B 125 (2007): 353.
- [54] Driskell, J. D.; Shanmukh, S.; Liu, Y.; Chaney, S. B.; Tang, X-J.; Zhao, Y-P. et al. The Use of Aligned Silver Nanorod Arrays Prepared by Oblique Angle Deposition as Surface Enhanced Raman Scattering Substrates. J. Phys. Chem. C 112 (2008): 895.
- [55] Nie, S.; Emory, S. R. Probing Single Molecules and Single Nanoparticles by Surface-Enhanced Raman Scattering. Science 275 (1997): 1102.
- [56] Wang, Y.; Kneipp, H.; Perelman, L. T.; Itzkan, I.; Dasari, R. R.; Feld, M. S. et al. Single Molecule Detection Using Surface-Enhanced Raman Scattering. Phys. Rev. Lett. 78 (1997): 1667.

- [57] Liao, P. F.; Bergman, J. G.; Chemla, D. S.; Wokaun, A.; Melngailis, J.; Hawryluk, A. M. et al. Surface-enhanced Raman scattering from molecules in tunnel junctions. Chem. Phys. Lett. 82 (1981): 355.
- [58] Nuntawong, N.; Horprathum M.; Eiamchai P.; Wong-ek K.; Patthanasettakul V.; Chindaudom P. Surface-enhanced Raman scattering substrate of silver nanoparticles depositing on AAO template fabricated by magnetron sputtering. Vacuum 84 (12) (2010): 1415–1418.
- [59] Zhang, X.; Yonzon, C. R.; Young, M. A.; Stuart, D. A.; Van, D. R. P. Biological applications of localised surface plasmonic phenomena. IEEE Proc. Nanobiotechnol. 2005: 152.
- [60] Walsh, R. J.; Chumanov, G. Silver Coated Porous Alumina as a New Substrate for Surface-Enhanced Raman Scattering. Appl. Spectrosc. 55 (2001): 1695.
- [61] Xiao, G. N.; Man, S. Q. Self-Assembled on Ag, Cu, Au, and Pt. Chem. Phys. Lett. 447 (2007): 305.
- [62] Zuxuan, L.; Christopher, M. Y.; Joseph, I. S. Michael D W. Operation of an ultrasensitive 30 MHz quartz crystal microbalance in liquids. Anal. Chem. 65 (1993): 1546–1551.
- [63] Ekinci, K. L.; Huang, X. M.; Roukes, M. L. Ultrasensitive nanoelectromechanical mass detection. Appl. Phys. Lett. 84 (2004): 4469-4471.
- [64] Schram, M.; Mandel, J.; Drost, S. Ultrasensitive quartz crystal microbalance sensors for detection of m13-phages in liquids. Biosens. and bioelectron. 12(2001): 735-743.

- [65] Zenonas, J.; Stanley, B. Electrochemical quartz crystal microbalance study of perchlorate and perrhenate anion adsorption on polycrystalline gold electrode. *Electrochemistry communications* 2(2000): 412-416.
- [66] Rafael, G.; Matt, D.; Tad, D.; David, A.; Chana, M. H. W. Ultrasensitive quartz crystal microbalance with porous gold electrodes. *Appl. Phys. Lett.* 84(2004): 628-630.
- [67] Brunauer, S.; Emmett, P. H.; Teller, E. Adsorption of gases in multimolecular layers. *J. Am. Chem. Soc.* 60(1938): 309-319.
- [68] Driskell, J.; Shanmukh, S.; Liu, Y.; Chaney, S.; Tang, X.-J.; Zhao, Y. P.; Dluhy, R. The use of aligned silver nanorod arrays prepared by oblique angle vapor deposition. *Journal of Physics Chemistry*. 122 (2008): 895–901.
- [69] Rosa, F. D.; Lauro, T. K. An SPR immunosensor for human cardiac troponin T using specific binding avidin to biotin at carboxymethyl-dextran-modified gold chip. *Clinica Chimica Acta* 376 (2007): 114-120.
- [70] Inger, V. Self-assembly of antibody fragments and polymers onto gold for immunosensing. *Sensors and Actuators B* 106 (2005): 311–316.
- [71] Paterson, S. J.; Robson, L. E.; Kosterlitz, H. W.; Jin, W-Q. Effect of Tris, HEPES, and TES buffers on binding at  $\mu$ -,  $\delta$ -, and  $\kappa$ -opioid sites in guinea pig brain. *Journal of Pharmacological Methods* 23 (1990): 275-283.
- [72] Olivieri, E.; Sebastiano, R.; Citterio, A.; Gelfi, C.; Righetti, P. G. Quantitation of protein binding to the capillary wall in acidic isoelectric buffers and means for minimizing the phenomenon. *Journal of Chromatography* 894 (2000): 273-280.
- [73] Thom, H.; Patrick, F.; Alan, F.; Kelly L. Properties of casein micelles in high

- pressure-treated bovine milk. Food Chemistry 87 (2004): 103-110.
- [74] Laurent, G.; Fe, L. N.; Aubard, J.; Levi, G. Evidence of multipolar excitations in surface enhanced Raman scattering. Phys. Rev. B 71 (2005): 045430.
- [75] Jiang, H.; Chen, W. X.; Xu, Z. D.; Chin, N. Scanning Tunneling Microscopy of Ring-Shape Endohedral Metallofullerene (Nd@C<sub>82</sub>)<sub>6,12</sub> Clusters. J. Phys. Chem. 11 (1998): 82.
- [76] Félidj, N.; Aubard, J.; Lévi, G.; Krenn, J. R.; Salerno, M.; Schiner, G. et al. Atomic chains of group-IV elements and III-V and II-VI binary compounds studied by a first-principles pseudopotential method. Phys. Rev. B 65 (2005): 075419.
- [77] Naujok, R. R.; Duevel, R. V.; Corn, R. M. Fluorescence and Fourier Transform surface-enhanced Raman scattering measurements of methylene blue adsorbed onto a sulfur-modified gold electrode. Langmuir 9 (1993): 1771-1774.
- [78] Hulchineon, K.; Heater, R.; Albery, J.; Hillman, A. R. Reduction of nitrobenzene in aqueous alkaline solution at an Ag electrode: Observation by SERS, RRDE and UV absorption. J. Chem. Soc. Faraday Trans. 1(80) (1984): 2053.

## **BIOGRAPHY**

Krongkamol Wong-ek was born on September, 1980 in Nakornratchasima Province, Thailand. She began studying in the bachelor degree of medical technology by specialized election of Thammasat University in year 1998 and graduated in 2002. She received the scholarship from Thai government under the National of Science and Technology for Development Agency (NSTDA) graduate project for master course in Biomedical Instrumentation at King Mongkut's University of Technology and graduated in 2005. Then she worked at the department of Medical Technology and Graduate Program of Biomedical Science, Faculty of Allied Health Science, Thammasat University until 2009.

Since 2007, she had become a Ph.D. student in Nano-Biosensor field and worked under the supervision of Associate Professor Dr. Orawon Chailapakul. In 2009, she had received the scholarship from Thailand Graduate Institute of Science and Technology (TGIST), NSTDA which collaborated with Dr. Adisorn Tuantranont and his team at Nanoelectronics and MEMS Laboratory, National Electronics and Computer Technology Center (NECTEC), in which project is to study the Quartz Crystal Microbalance (QCM) and Flow Injection System. In the same time, she had also worked with Dr. Noppadon Nuntawong and his team for Surface- Enhanced Raman Scattering Substrate Fabrication at Photonics Technology Laboratory, NECTEC. And in 2010, she had a chance to do research project with Professor Anthony G. Cass, Imperial Collage London, UK for 6 months. She graduated with Ph.D. degree in Nanoscience and Technology of academic year 2010 from Chulalongkorn University.

**APPENDIX A**  
Publications

### List of Publications

1. **Wong-ek K**, Eiamchai P, Horprathum M, Patthanasettakul V, Limnonthakul P, Chindaudom P, Nuntawong N, Silver nanoparticles deposited on anodic aluminum oxide template using magnetron sputtering for surface enhanced raman substrate, *Thin Solid Film*, 2010; 518: 7128–7132.
2. **Wong-ek K**, Chailapakul O, Nuntawong N, Jaruwongrungsee K, Tuantranont A. Cardiac Troponin T detection using polymers coated quartz crystal microbalance as a cost effective immunosensor, *Biomed Tech (Berl)*, 2010. (In Press)
3. Nuntawong N, Horprathum M, Eiamchai P, **Wong-ek K**, Patthanasettakul V, and Chindaudom P, Surface-enhanced Raman scattering substrate of silver nanoparticles depositing on AAO template fabricated by magnetron sputtering, *Vacuum*, 2010; 84(12): 1415-1418.

### List of Conference Proceedings

1. **Wong-ek K.**, Chailapakul O., Nuntawong N., Jaruwongrungsee K., Sritongkham P. Tuantranont A., Mass Sensitive Sensor, A Comparative Study Between PVC And PEI Coated on Quartz Crystal Microbalance, *IEEE International Nanoelectronics Conference*, 2010.
2. **Wong-ek K.**, Chailapakul O., Prommas J., Jaruwongrungsee K., Nuntawong N., Tuantranont A., QCM Based On Flow System For Cardiovascular Disease, *IFMBE Proceedings on World Congress on Medical Physics and Biomedical Engineering*, 2009.
3. **Wong-ek K.**, Wisitsoraat A., Jaruwongrungsee K., Tuantranont A., Comparative study of controlled of QCM, PEI, glutaraldehyde for immobilization of cTnT antibody to diagnosis cTnT, *IEEE International Nanoelectronics Conference*, 2008.
4. **Wong-ek K.**, Wisitsoraat A., Jaruwongrungsee K., Tuantranont A., Modified Quartz crystal microbalance biosensor for cardiovascular marker diagnosis, *The Tenth World Congress on Biosensors*, 2008.



Contents lists available at ScienceDirect

Thin Solid Films

journal homepage: [www.elsevier.com/locate/tsf](http://www.elsevier.com/locate/tsf)

## Silver nanoparticles deposited on anodic aluminum oxide template using magnetron sputtering for surface-enhanced Raman scattering substrate

Krongkamol Wong-ek<sup>a</sup>, Pitak Eiamchai<sup>b</sup>, Mati Horprathum<sup>b</sup>, Viyapol Patthanasettakul<sup>b</sup>, Puenisara Limnonthakul<sup>c</sup>, Pongpan Chindaudom<sup>b</sup>, Noppadon Nuntawong<sup>b,\*</sup>

<sup>a</sup> Nanoscience and Technology Program, Chulalongkorn University, Bangkok 10330, Thailand

<sup>b</sup> National Electronics and Computer Technology Center, 112 Thailand Science Park, Phahonyothin Rd., Klong Luang, Pathumthani 12120, Thailand

<sup>c</sup> Department of Physics, Faculty of Science, King Mongkut's University of Technology Thonburi, Bangkok 10140, Thailand

### ARTICLE INFO

#### Article history:

Received 30 April 2009

Received in revised form 16 June 2010

Accepted 6 July 2010

Available online 24 July 2010

#### Keywords:

Silver nanoparticles

Raman scattering

Surface enhanced raman scattering

Magnetron sputtering

Anodic aluminum oxide

Scanning electron microscopy

### ABSTRACT

Low-cost and highly sensitive surface-enhanced Raman scattering (SERS) substrates have been fabricated by a simple anodizing process and a magnetron sputtering deposition. The substrates, which consist of silver nanoparticles embedded on anodic aluminum oxide (AAO) templates, are investigated by a scanning electron microscope and a confocal Raman spectroscopy. The SERS activities are demonstrated by Raman scattering from adsorbed solutions of methylene blue and pyridine on the SERS substrate surface. The most optimized SERS substrate contains the silver nanoparticles, with a size distribution of 10–30 nm, deposited on the AAO template. From a calculation, the SERS enhancement factor is as high as  $8.5 \times 10^7$ , which suggests strong potentials for direct applications in the chemical detection and analyses.

© 2010 Elsevier B.V. All rights reserved.

### 1. Introduction

Raman spectra have been widely used to identify a wide variety of unknown chemical and biological molecules. Such molecules generally hold vibrational energy levels unique for particular molecular species. Practically the Raman spectra obtained from measurements also reflects fingerprints of the molecular structures. However, a conventional Raman spectroscopy usually suffers from a small fraction of a Raman scattering cross section. As a result, a detectable Raman intensity requires a large amount of specimen and a strong incident light. Because of its inconvenience, the conventional Raman spectroscopy therefore needs enhancement to the Raman sensitivity. A developed technique, also known as surface-enhanced Raman scattering (SERS), has drawn a great deal of work in its mechanism in order to make practical uses for the chemical and biological analyses [1–6]. In addition, the SERS method presents several potential advantages over other spectroscopic techniques in terms of measurement speed, high sensitivity, portability, and simple maneuver.

Despite a number of extensive researches focused on the SERS technique, its mechanism is still under debated [4–6]. It has now been widely recognized that for a given metal nanoparticle system, the

SERS activity occurs for nanoparticles between 10 and 100 nm in size [6]. The most effective SERS substrates to date are colloidal silver or gold clusters widely used in the bulk-volume solution-based detections [7–10]. However, these nanoparticles fabricated from a chemical reduction usually lose effectiveness from residual organics. This may have an adverse influence in the work that requires a highly selective detection. In contrast, a fabrication of metal nanostructures by physical vapor deposition has relatively clean surfaces. The assembly of the nanostructural arrays on silicon substrate can be used as a SERS-active on a chip. The efforts in fabricating metal nanopillars [11], nanoclusters [12] and nanogrooves [13] as a SERS-active layer on silicon substrates have been extensively studied and demonstrated. Nonetheless, the sample fabrication of such reports requires significantly serious and expensive efforts that hinder their applications beyond a laboratory scale.

In this work, we explore a method to fabricate highly sensitive, cost effective SERS substrates. The magnetron sputtering system, which benefits from an easy adaptation to a large-scale production, is used to deposit silver nanoparticles on top of a thin anodic aluminum oxide (AAO) template. The presence of the AAO template, which has previously been fabricated by a simple anodizing process on a silicon substrate, aims to increase the surface area and prevent coalescence of the deposited silver nanoparticles. By maintaining a high density of the silver nanoparticles deposited on the prepared substrates, a large SERS enhancement activity can now be obtained.

\* Corresponding author.

E-mail address: [noppadon.nuntawong@nectec.or.th](mailto:noppadon.nuntawong@nectec.or.th) (N. Nuntawong).



## 2. Experimental details

All metal films coated on a silicon substrate are prepared by a homemade dc magnetron sputtering system. A high vacuum (HV) state is obtained from mechanical and turbo-molecular pumps. The plasma cleaning is performed on the silicon surface with 70W RF power, 16.25 MHz frequency, and 5 sccm argon flow for 5 min prior to the metal deposition. During the film deposition, the base pressure and the operating pressure of the deposition chamber reach  $1.0 \times 10^{-3}$  Pa and 0.4 Pa, respectively. The metal films are then deposited with a DC power supply using 0.1 A sputtering current and 340 kV voltage on the desired substrate. The substrate is fixed on a substrate holder with a distance between the sputtering targets to substrate of 70 cm.

First, an AAO template is prepared by a fabrication of an aluminum film on top of a p-type (100) silicon substrate. With a 3-in. aluminum (99.99%; KJ.Lesker) sputtering target, we now obtain the aluminum film of 120 nm as verified by a Hitachi's s-5200 field emission scanning electron microscope (FE-SEM) using an operating voltage of 10 kV. The as-deposited film is then followed by an anodizing process. From one power supply, we connect its anodic electrode to the as-deposited sample and its cathode electrode to a gold-plated silicon substrate. Both connected samples are then submerged in an oxalic acid at 0.3 M concentration. The anodizing current which is precisely controlled by a Motech's LPS-305 digital power is supplied at 10 mA with a voltage limit of 40 V. After 15 min, a large fraction of the aluminum film is removed, transforming the film into  $\text{Al}_2\text{O}_3$  nanopores with 5–10 nm thick sidewalls. The nanopore substrate is subsequently dissolved in 5 wt.%  $\text{H}_3\text{PO}_4$  for 30 min in order to remove the  $\text{Al}_2\text{O}_3$  sidewalls, thus widening the pore size. We now acquire the AAO template on the silicon substrate that can readily be used next in the preparation of the silver nanoparticles.

On the same sputtering system, we use a 3-in. silver (99.99%; KJ.Lesker) sputtering target to deposit silver nanoparticles on the prepared AAO template. The deposition rate is approximately 1 nm/s as calibrated by a spectroscopic ellipsometer (J.A. Woollam; HTC-100). The features and size distribution of the silver nanoparticles on both types of the substrates can be characterized by FE-SEM. For a straightforward comparison, we focus our experiment on the AAO templates and the blank silicon wafers, both deposited with the silver nanoparticles for 8 and 16 s. Our final samples of the deposited silver nanoparticles on the AAO templates, so called the surface-enhanced Raman substrates (SERS), are expected to yield higher Raman sensitivity for test molecules.

The Raman sensitivity of the SERS substrates can be easily analyzed from the Raman spectra taken by an NT-MDT NTEGRA Raman spectrometer equipped with a thermoelectrically cooled detector with spectral resolution of  $2 \text{ cm}^{-1}$ . A 633 nm He-Ne laser is used as the excitation source. The laser power is maintained at 3.5 mW. 100 $\times$  objective lens is used, giving a spot size of around  $1 \mu\text{m}^2$ . We use two types of aqueous solution, i.e., methylene blue (MB) and pyridine, to provide probing molecules in order to evaluate SERS activities of the fabricated SERS substrates. First, each droplet of the MB solution, with a volume of  $5 \times 10^{-2}$  ml and a concentration of  $5 \times 10^{-3}$  M, on the SERS substrates is allowed to dry in air atmosphere. The Raman spectra are then taken immediately using a laser excitation. In order to confirm the effectiveness of the SERS substrates, pyridine, which is 2–3 orders of magnitude less sensitive than MB, is also used. Each pyridine droplet at a volume of  $5 \times 10^{-2}$  ml, made by dilution of an aqueous solution of  $1 \times 10^{-3}$  M pyridine in  $5 \times 10^{-2}$  M HCl, is again allowed to dry before the Raman spectral measurements.

## 3. Results and discussion

When we first acquired the thick aluminum film deposited on the silicon substrates, the electrolytic process immediately follows.

Fig. 1(a) shows the surface topology of the aluminum film after the anodization for 15 min. The image illustrates a large fraction of aluminum film which is transformed into  $\text{Al}_2\text{O}_3$  shallow nanoholes with the diameter of 10 nm. We dissolved  $\text{Al}_2\text{O}_3$  compound from the obtained sample in 5 wt.%  $\text{H}_3\text{PO}_4$  for 30 min to widen up the pore size. An increase of the pore size can be observed in Fig. 1(b) which illustrates the nanoholes with diameter of 30–40 nm on the aluminum surface. An inset in Fig. 1(b) shows a cross-sectional image which suggests that the pore is completely opened from the top surface of the aluminum film to the silicon substrate interface. From a simple calculation, the density of the nanoholes in the fabricated AAO template is approximately  $2 \times 10^{10} \text{ cm}^{-2}$ .

After fabricating the AAO template on the silicon wafer with the optimized conditions, we deposit the silver nanoparticles for 8 and 16 s on the prepared template. The SEM images for the surface topology of the as-deposited samples are illustrated in Fig. 2. In Fig. 2(a), the deposition for 8 s results in the silver nanoparticles with a diameter size of 10–30 nm clearly observed inside the pore of the AAO template. With a filling probability of approximately 50%, the density of the embedded silver nanoparticles inside the nanopores is approximately  $1 \times 10^{10} \text{ cm}^{-2}$ . For the deposition time of 16 s, we observe a narrower pore size in Fig. 2(b) when compare with that in Fig. 2(a). Fig. 2(b) also indicates an observable coalescence of silver nanoparticles along the sidewalls and the top of the AAO template. For a pictorial description, the schematic of the silver nanoparticles deposited on the AAO template is illustrated in Fig. 3. The figure depicts the early stage of the sputter deposition, where the silver nanoparticles fill both inside the nanopores and on top of their sidewalls.

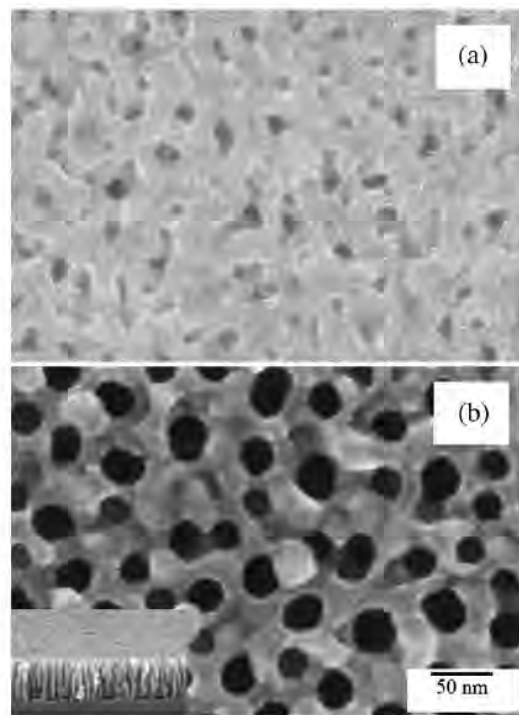


Fig. 1. SEM images of the surface topology of the anodized aluminum: (a) before etching, and (b) after 30 min of  $\text{H}_3\text{PO}_4$  etching.

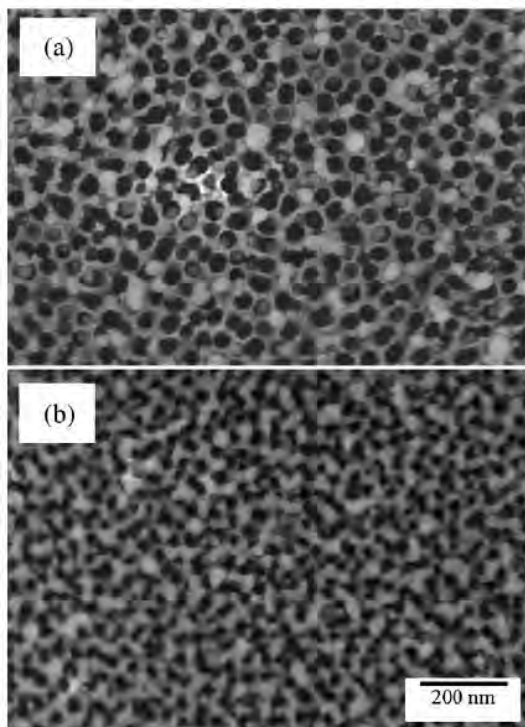


Fig. 2. SEM images of the surface topology of the SERS substrates with the silver nanoparticles deposited on the AAO template for (a) 8 s, and (b) 16 s.

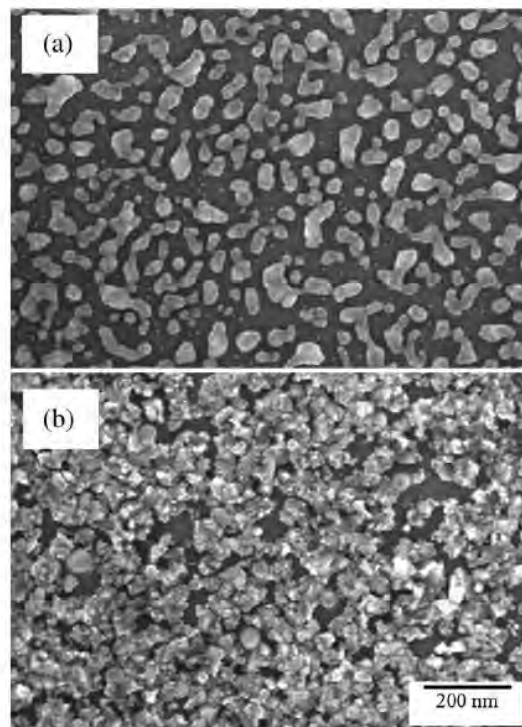


Fig. 4. SEM images of the surface topology of the substrates with the silver nanoparticles deposited on the blank silicon wafers for (a) 8 s, and (b) 16 s.

For comparison, we also deposit the silver nanoparticles, for 8 and 16 s, on the blank silicon wafers without the AAO template. The SEM images for the surface topology of these as-deposited samples are illustrated in Fig. 4. Without the AAO-template layers, the nanoparticles deposited for 8 s appear to migrate along the substrate surface and coalesce to form a larger island as shown in Fig. 4(a). The coalescence of Ag clusters results in the decrease in the density and the surface area of the silver nanoparticles that can be bounded to an analyte. For the deposition time of 16 s, the silver nanoparticles begin to form crystallites which appear as sharp-edge grain boundaries as shown in Fig. 4(b). The crystalline formation of the silver film from the

figure has been confirmed by X-ray diffraction in a glancing incident mode (results not shown). Note that the coalescence and the crystallization of the smoother surface would result in the reduction of the silver surface area that could deteriorate the electromagnetic coupling effect between the silver nanoparticles.

With several types of Raman-active substrates available, we first examine their Raman sensitivity with tiny droplets of the MB solution. The Raman spectra of MB adsorbed on the different SERS substrates are presented in Fig. 5. Spectrum (a) indicates the Raman spectrum of MB adsorbed on the blank silicon substrate without the SERS structure. The peak at  $520\text{ cm}^{-1}$  corresponds to the typical Raman shift of the crystalline silicon substrate. From this spectrum, the Raman scattering intensity originated from MB adsorbed on this type of surface is not strong enough to be observed. Spectrum (b) presents the Raman spectral intensity of MB adsorbed on the blank AAO, which increases a broad spectrum for the silicon peak. This broad-spectral region is most likely a result of interactions between MB and the AAO nanopores due to the increased surface area combined with the capillary effect. The combination eventually leads to an increase in the background scattering. Spectra (c) and (d) present the effects of the silver nanoparticles coated for 16 and 8 s, respectively, on the silicon substrate surfaces without the AAO templates. These substrates containing the silver nanoparticles promote some characteristic Raman peaks of MB to become visible. The results indicate the enhancement activity from the silver nanoparticles although they are deposited on the smooth surface. Note that the Raman intensity of the spectrum (c) is half as much as that of the spectrum (d), indicating that the coalescence of the silver nanoparticles is an important factor that limits the Raman enhancement of these prepared substrates.

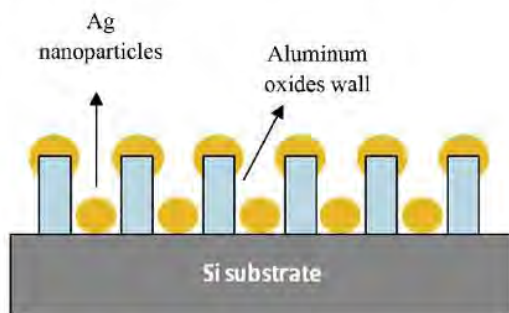


Fig. 3. Schematic of the silver nanoparticles deposited on the AAO template previously fabricated on top of the silicon wafer.

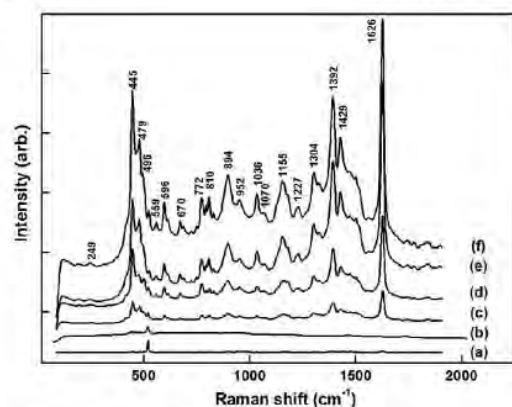


Fig. 5. Raman spectra of dried methylene blue droplets on several types of the sample surfaces: (a) blank silicon surface, (b) blank AAO template on Si, (c) 16 s silver nanoparticles deposited on Si, (d) 8 s silver nanoparticles deposited on Si, (e) 16 s silver nanoparticles deposited on AAO template, and (f) 8 s silver nanoparticles deposited on AAO template.

Next, spectra (e) and (f) show the spectral Raman intensities of the prepared SERS substrates which consist of the silver nanoparticles, deposited at 16 and 8 s, respectively, in the AAO templates. Note that the spectrum (e) verifies that the SERS substrate prepared with 8 s of the silver deposition on the AAO template yields the maximum SERS enhancement factor as a result of a high density of an isolate silver nanoparticle as discussed above. The SERS spectrum from this sample also reveals several molecular details of MB adsorbed on the SERS substrate. For example, the peak at  $249\text{ cm}^{-1}$  is originated from the Silver–N stretching of the Silver–(MB) complex [14,15]. This peak cannot be observed in normal Raman spectra measured from the other types of the prepared substrates. In addition, two main characteristic peaks of MB at  $445$  and  $1626\text{ cm}^{-1}$  correspond to the C–N–C skeleton bending and the C–C stretching, respectively [14,16,17]. The relatively strong intensity and the sharp details of these peaks indicate that the MB molecules are tightly adsorbed on the SERS surface. The final results are the highly enhanced Raman signal. Apart from the aforementioned Raman peaks, the other band assignments for the MB molecular structures are summarized in Table 1. Note that all assigned bands are in good agreement with the Refs. [16–18], although the bands without proper assignments at 894 and  $1304\text{ cm}^{-1}$  are also reported in the previous study by another group [14].

To confirm the SERS activity of the optimized SERS substrates, we use pyridine as the other probing molecules because they are much less sensitive than the MB molecules. The intense spectrum of pyridine adsorbed on the optimized SERS substrate can be observed as shown in Fig. 6. This spectrum shows the molecular details that resembles previously reported SERS spectra obtained from silver colloids [19,20], indicating a highly effective SERS enhancement. The broad peak at around  $235\text{ cm}^{-1}$  can again be assigned to the

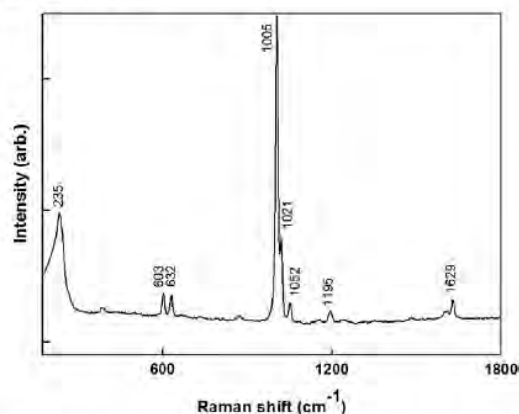


Fig. 6. Raman spectrum of dried droplets of a solution of  $1 \times 10^{-3}\text{ M}$  pyridine and  $5 \times 10^{-2}\text{ M}$  HCl on the SERS substrate with 8 s silver nanoparticles deposited on the AAO template.

stretching mode of the Silver–N bond. The most intense bands in the spectrum at  $1005$  and  $1021\text{ cm}^{-1}$  correspond to a symmetric ring breathing mode and a trigonal ring breathing mode, respectively.

Finally, we calculate the Raman enhancement factor from the spectra in Fig. 5. The enhancement factor is defined as the ratio of inelastic scattering intensity per molecule between the presence and absence of the SERS structure. The Raman enhancement factor can be written as [14–16,21,22]:

$$G = \frac{I_{\text{SERS}}}{I_{\text{Ref}}} \cdot \frac{N_{\text{Ref}}}{N_{\text{SERS}}} \quad (1)$$

$I_{\text{SERS}}$  is the enhanced intensity of the adsorbed MB molecules on the SERS substrate. The value of  $I_{\text{SERS}}$  mainly arises from a single molecule layer covering a nanoparticle array, from which other additional molecules layers of analytes on the SERS substrate, as previously reported [14], do not contribute in Raman gain and can be neglected.  $I_{\text{Ref}}$  is the spontaneous Raman scattering intensity from the bulk MB molecules under the laser spot on the blank silicon substrate.  $N_{\text{SERS}}$  is the number of the single-layer molecules covering the SERS substrate under the laser spot.  $N_{\text{Ref}}$  is the number of the bulk molecules excited by laser on the surface of the regular substrate. In order to obtain the values of these four parameters, we follow the same procedures based on the published literatures [14–16,21,22]. Using the  $100\times$  objective lens, we determine the area of the laser spot size at around  $1\text{ }\mu\text{m}^2$ . We also calculate the area of a single molecule of MB to be approximately  $2\text{ nm}^2$  [23]. Thus, the value of  $N_{\text{SERS}}$  under the laser excitation is approximately  $5 \times 10^5$  molecules. The focusing scope of laser beam is approximately  $5\text{ }\mu\text{m}$ , thus scattering from all MB molecules underneath the laser spot is detected. Assuming a uniform distribution of MB over the droplet area of  $2\text{ mm}^2$ , the value of  $N_{\text{Ref}}$  is

Table 1  
Band assignments and enhancement factors calculated from the SERS spectra (c)–(f) as shown in Fig. 5.

Band assigned	$\delta(\text{C-N-C})$	$\alpha(\text{C-S-C})$	N/A	$\beta(\text{C-H})$	$\nu(\text{C-N})$	N/A	$\alpha(\text{C-H})$	$\nu_{2\text{sym}}(\text{C-N})$	$\nu(\text{C-C})$ ring	Average
Raman shift ( $\text{cm}^{-1}$ )	445	612	894	1036	1155	1304	1392	1429	1626	
G factor	c	$8.9 \times 10^6$	$1.1 \times 10^7$	$8.7 \times 10^6$	$1.1 \times 10^7$	$9.1 \times 10^6$	$9.0 \times 10^6$	$7.9 \times 10^6$	$1.2 \times 10^7$	$7.4 \times 10^6$
	d	$2.3 \times 10^7$	$2.5 \times 10^7$	$2.1 \times 10^7$	$2.6 \times 10^7$	$2.3 \times 10^7$	$2.3 \times 10^7$	$2.1 \times 10^7$	$2.9 \times 10^7$	$2.0 \times 10^7$
	e	$4.2 \times 10^7$	$5.3 \times 10^7$	$4.7 \times 10^7$	$6.3 \times 10^7$	$5.6 \times 10^7$	$5.6 \times 10^7$	$5.0 \times 10^7$	$7.7 \times 10^7$	$4.7 \times 10^7$
	f	$7.6 \times 10^7$	$9.8 \times 10^7$	$8.1 \times 10^7$	$1.1 \times 10^8$	$8.7 \times 10^7$	$8.2 \times 10^7$	$6.8 \times 10^7$	$1.1 \times 10^8$	$5.8 \times 10^7$

Please cite this article as: K. Wong-ek, et al., Thin Solid Films (2010), doi:10.1016/j.tsf.2010.07.017

approximately  $7.5 \times 10^{10}$  molecules. Therefore, from Eq. (1), the enhancement factor  $G$  is simply  $(1.5 \times 10^5) \cdot (I_{\text{SERS}}/I_{\text{Ref}})$ . The enhancement factors of each assigned Raman peak as measured from different SERS substrates are also shown in Table 1. The results show that the highest enhancement factor can be achieved at the average value of  $8.5 \times 10^7$  from the spectrum ( $f$ ), which obtained from the optimized SERS substrate.

#### 4. Conclusions

In this paper, we discuss the fabrication of the low-cost, highly sensitive SERS substrates by the magnetron-sputtering deposition of the silver nanoparticles on the prepared AAO templates. The presence of the AAO templates helps suppress the coalescence of the deposited nanoparticles. With the optimized deposition conditions, we obtain a high density of the silver nanoparticles, at approximately  $1 \times 10^{10} \text{ cm}^{-2}$ , embedded along the sidewalls and on the tops of the AAO nanoholes. The SERS activity of the fabricated SERS substrate is demonstrated by using MB and pyridine as the probing molecules. The molecular details of both analytes can be clearly observed from the strong Raman spectral intensities. Calculated from the Raman signals based on the MB probing molecules, the enhancement factor for our SERS substrates can be achieved up to  $8.5 \times 10^7$ , which suggests promising potentials for direct applications in the chemical detections and analyses.

#### Acknowledgements

This work has been supported by Sensor Technology (SST), National Electronics and Computer Technology Center (NECTEC), Thailand and Thailand Graduate Institute of Science and Technology

(TGIST), research grant of National Science and Technology Development Agency (NSTDA), Ministry of Science and Technology, Thailand.

#### References

- [1] K. Kneipp, Y. Wang, H. Kneipp, L.T. Perelman, I. Itzkan, *Phys. Rev. Lett.* 78 (1997) 1667.
- [2] K. Kneipp, H. Kneipp, J. Kneipp, *Acc. Chem. Res.* 39 (2006) 443.
- [3] C. Ruan, G. Eres, W. Wang, Z. Zhang, B. Gu, *Langmuir* 23 (2007) 5757.
- [4] H.X. Xu, E.J. Bjerneld, M. Kall, L. Borjesson, *Phys. Rev. Lett.* 83 (1999) 4357.
- [5] A. Otto, I. Mrozek, H. Grabhorn, W. Akemann, *J. Phys. Condens. Matter* 4 (1992) 1143.
- [6] M. Moskovits, *J. Raman Spectrosc.* 36 (2005) 485.
- [7] T.M. Cotton, S.G. Schultz, R.P. Vanduyne, *J. Am. Chem. Soc.* 102 (1980) 7960.
- [8] J. Jiang, K. Bosnick, M. Maillard, L. Brus, *J. Phys. Chem. B* 107 (2003) 9964.
- [9] Y.W.C. Cao, R.C. Jin, C.A. Mirkin, *Science* 297 (2002) 1536.
- [10] B.D. Moore, L. Stevenson, A. Watt, S. Flitsch, N.J. Turner, C. Cassidy, D. Graham, *Nat. Biotechnol.* 22 (2004) 1133.
- [11] S.B. Chaney, S. Shanmukh, R.A. Dluhy, Y.-P. Zhao, *Appl. Phys. Lett.* 87 (2005) 031908.
- [12] J. Fang, Y. Yi, B. Din, X. Song, *Appl. Phys. Lett.* 92 (2008) 131115.
- [13] T.A. Alexander, D.M. Le, *Appl. Opt.* 46 (2007) 3878.
- [14] G.N. Xiao, S.Q. Man, *Chem. Phys. Lett.* 447 (2007) 305.
- [15] H. Jiang, W.X. Chen, Z.D. Xu, *Chin. J. Chem. Phys.* 11 (1998) 82.
- [16] G. Laurent, N. Félidj, J. Aubard, G. Lévi, J.R. Krenn, A. Hohenau, G. Schider, A. Leitner, F.R. Aussenegg, *Phys. Rev. B* 71 (2005) 045430.
- [17] R.R. Naujok, R.V. Duevel, R.M. Corn, *Langmuir* 9 (1993) 1771.
- [18] K. Hulchineon, R. Heater, J. Albery, A.R. Hillman, *J. Chem. Soc. Faraday Trans. 1* (80) (1984) 2053.
- [19] J.A. Creighton, C.G. Blatchford, M.G. Albrecht, *J. Chem. Soc. Faraday Trans. 2* (75) (1979) 790.
- [20] J.A. Creighton, *Surf. Sci.* 124 (1983) 209.
- [21] M. Green, F.M. Liu, *J. Phys. Chem. B* 107 (2003).
- [22] N. Félidj, J. Aubard, G. Lévi, J.R. Krenn, M. Salerno, G. Schider, B. Lamprecht, A. Leitner, F.R. Aussenegg, *Phys. Rev. B* 65 (2002) 075419.
- [23] R. Hoppe, G. Schulz-Bkloff, D. Wöhrle, E.S. Shpiro, O.P. Tkachenko, *Zeolites* 13 (1993) 222.

## Cardiac troponin T detection using polymers coated quartz crystal microbalance as a cost-effective immunosensor

Krongkamol Wong-ek<sup>1\*</sup>, Orawon Chailapakul<sup>1</sup>, Noppadon Nuntawong<sup>2</sup>, Kata Jaruwongrunsee<sup>3</sup> and Adisorn Tuantranont<sup>3</sup> ((\*\*author: please check/ confirm that all names are in order of first name, last name\*\*))

<sup>1</sup> Nanoscience and Technology Program, Chulalongkorn University, Bangkok, Thailand

<sup>2</sup> Photonics Technology Laboratory, National Electronics and Computer Technology, Thailand Science Park, Patumthani, Thailand

<sup>3</sup> Nanoelectronics and MEMS Laboratory, Thailand Science Park, Patumthani, Thailand

### Abstract

Cardiac troponin T (cTnT) detection has been the focus of increased interest due to its role in myocardial infarction diagnosis. In this study, we report a relatively low cost technique to detect cTnT using a quartz crystal microbalance (QCM) sensor. A sensitive detection is achieved by introducing a QCM surface with a carboxylic polyvinyl chloride immobilization layer. The surface morphologies of this polymer film under varied deposition thickness have been investigated by field emission scanning electron microscopy and atomic force microscopy. A cTnT detection result from a modified QCM surface can be obtained within a short response time by a direct detection of the immunoreaction and a direct conversion of mass accumulation into a frequency shift, representing a measurable electrical signal. The relationship between the cTnT concentration and the response current from a QCM sensor shows detectability at the concentration of cTnT as low as 5 ng/ml.

**Keywords:** cardiac troponin; quartz crystal microbalance; sensors.

### Introduction

Cardiac troponin complex is an important marker that has recently replaced creatine kinase (CK), M (muscle) B (brain) as the analysis of choice of acute myocardial infarction (AMI) diagnosis [10]. Cardiac troponin T (cTnT) is one of the three proteins of the troponin complex, which mediates the calcium activity elevated in patients with AMI, and is recognized by World Health Organization diagnostic criteria

[31]. Multiple studies have demonstrated that cTnT is an important prognostic indicator in patients presenting with chest pain, even when CK-MB fraction is not elevated [1]. Several methods have been used to detect cTnT, such as enzyme linked immunosorbent assay [13, 25] or radioimmunoassay [3, 28], and have now become standard analytical methods. Nonetheless, limitations of these methods include a relatively slow process, a highly reagent consumption and a complicated procedure. In addition, these methods require an expensive analyzer system for a high sensitivity detection because the elevated cTnT concentration collected from a patient with heart damage could be as low as 5 ng/ml [14]. Even though the new development of automated commercial systems in the present market can deliver detection limits below 0.05 ng/ml [8, 9, 33], the high running cost still hinders cTnT measurement from daily clinical diagnostics.

Development of the commercial quartz crystal microbalance (QCM) system has offered a new opportunity for a rapid and low-cost cTnT sensor. By combining the QCM system with an immunoassay method, the quantification of cTnT protein can be done within a short period of time and with a minimum amount of sample and reagent use. Moreover, the QCM system provides a much simpler maneuver, is relatively less expensive, and is more stable than other conventional methods. Surprisingly, the QCM technique has been rarely reported in the study of cTnT detection. To date, there is only one investigation of cTnT detection using this technique [22]. The use of the QCM technique to detect cTnT could be a powerful parameter in AMI diagnosis, but has not been well studied.

The classical application of QCM is a thin film thickness monitoring system, in which a resonance frequency is inversely proportional to a total thickness of the thin film deposited on a quartz crystal surface. Monolayer sensitivity is easily reached. The QCM not only can be applied to rigid film but also in humidity and gas sensing. Although the liquid and gas molecules deposited on the quartz surface are not rigid material, they can be immobilized by the hygroscopic and gas sensing layer, which is rigidly deposited on the electrode surface [5, 7, 15, 23, 24]. For applications in biosensors, a sensor can be used to detect an additive mass of a specific biomolecule by sensing an immunoreaction on the immobilization layer of the quartz surface.

Owing to the great potential that the QCM method can offer in biosensors applications, the development of the surface modification techniques has been widely studied [11, 16, 21, 29, 30]. With this technique, the QCM sensor is coated with selected polymer that adsorbs the proteins and other biomolecules through an immobilization process. Because of the difference in physical properties of each polymer, choice of polymers and fabrication method are critical

\*Corresponding author: Krongkamol Wong-ek, Nanoscience and Technology Program, Chulalongkorn University, Bangkok 10330, Thailand  
E-mail: wongek@tu.ac.th

factors in enhancing an amount of the absorbed molecules on the quartz crystal surface [4, 17, 18, 20, 26]. In this study, cTnT detection using the QCM system was achieved by using polyvinyl chloride doped with carboxylic group coated on the quartz surface as an immobilization layer. This polymer which is a high plasticized membrane is used to improve cTnT immobilization by introducing a carboxyl group between surface of a quartz crystal and the 1-ethyl-3-(3-dimethylaminopropyl) carbodiimide (EDC), *N*-hydroxysuccinimide (NHS) crosslinker. The thicknesses of this polymer film under varied deposition thickness have been controlled using a step profiler. The surface morphologies were investigated using field emission-scanning electron microscopy (FE-SEM) and atomic force microscopy (AFM). Before cTnT detection, the stability of polymer coated QCM under fluid flow was investigated by injecting the fluid into the continuous flow system at various flow rates. The stability of polymer film was analyzed by recording the frequency fluctuation due to changes in velocity/viscosity of the fluid. For the cTnT detection experiments, multiple immobilization steps were performed including adsorption of EDC and NHS crosslinker on polymer film, followed by protein G adsorption. Then the cTnT with controlled concentration was injected into the flow system. Using the modified QCM sensor, the presence of cTnT can be detected within a short response time by the direct detection of the immunoreaction converted into the measurable acoustic resonant frequency shift. The experiments were repeated with cTnT at various concentrations ranging between 5 ng/ml and 50  $\mu$ g/ml.

## Materials and methods

### Reagents and materials

Carboxylic polyvinyl chloride (PVC-COOH), EDC, NHS and Protein G extracted from Streptococcal bacteria were purchased from Sigma-Aldrich Chemical Co. Inc. ((\*\*city, country of manufacturer\*\*)) Biotech grade Tetrahydrofuran (THF) purchased from Merck (Darmstadt, Germany) was used as a solvent for PVC-COOH. Spraying reagent was prepared by dissolving 1 mg of bulk PVC-COOH in 1 ml of THF with constant stirring for 10 min at room temperature. The 1-M phosphate buffer saline (PBS, pH 7.4) was used as a buffer solution for the continuous flow system. EDC and NHS were dissolved in distilled water just before being used at concentrations of 50 mM and 25 mM, respectively. The Monoclonal Antibody 9G6 and Human Cardiac Troponin T were purchased from Abcam Co. Inc. ((\*\*city, country of manufacturer\*\*)). The mouse monoclonal antibody of the IgG was produced only for use in these experiments. Commercial Silver-surface AT-cut quartz crystal with a fundamental resonance frequency of 12 MHz from Stanford Research System Inc. ((\*\*city, country of manufacturer\*\*)) was used as a base device.

### Polymer film fabrication and characterization

Fabrication of the polymer film on the quartz crystal surface consists of multiple preparation steps. First, the quartz crystal

was cleaned by methanol. Then, an airbrush system equipped with a 0.3-mm diameter nozzle was used to spray the solutions of PVC-COOH on the active zone of the quartz crystal surface. The spraying pressure of 1 bar was controlled during the deposition of the polymer precursors. The deposition rate was determined using a Veeco Dektak 150 step profiler ((\*\*city, country of manufacturer\*\*)). A series of samples was prepared with deposition thickness of 100, 200 and 300 nm. Then, the quartz crystal was washed five times in HNO<sub>3</sub> solution to eliminate excess of unbound polymer. Finally, the coated quartz crystal was rinsed with the PBS buffer to normalize the pH of the polymer surface. The quartz crystal was dried under nitrogen gas (N<sub>2</sub>) prior to measurements.

Surface morphologies of polymer films deposited on quartz surface under varied deposition thickness were investigated by a Hitachi S-5200 field emission scanning electron microscope ((\*\*city, country of manufacturer\*\*)). A Seiko Instrument SPA 400 ((\*\*city, country of manufacturer\*\*)) atomic force microscope was used to verify the root mean square (RMS) roughness and surface morphology of each sample.

### Flow injection system and stability of coated polymers under liquid flow

The continuous flow QCM sensor system developed by the Nanoelectronics and MEMS Laboratory (Patumthani, Thailand) was used for the cTnT detection experiments. This system consists of a NE-1000 programmable syringe pump from New Era Pump system Inc. ((\*\*city, country of manufacturer\*\*)) A microchannel flow cell equipped with the QCM device was connected to the syringe pump on one edge to collect the liquid flow. The liquid passes through the surface of the QCM and draws off on the opposite edge. The change in mass loading of the QCM sensor was directly measured though the quartz frequency shift using a universal frequency counter (Agilent 53131A, ((\*\*city, country of manufacturer\*\*))) connected to the device via an oscillator circuit. The measuring frequency shift data was transmitted to a computer via a GPIB port.

Before cTnT detection, the stability of PVC-COOH coated QCM under flow injection system was investigated. This was done by injecting the PBS to the system at various flow rates ranging from 50 l/min to 500 l/min. The QCM frequency shift resulting from liquid flow was then observed. At this step, the flow rate that delivered the most stable frequency shift was determined. Subsequently, the polymer-coated QCM was tested under this flow rate for the rest of the experiment.

### Preparation of cTnT concentrations

In this study, the bench-top instrument of an electrochemiluminescence detection technique from Roche Co., Ltd. ((\*\*city, country of manufacturer\*\*)) was performed to verify cTnT concentrations before using cTnT in QCM experiments. The diluted cTnT solution can be prepared by mixing the stock of cTnT and PBS buffer. The achieved

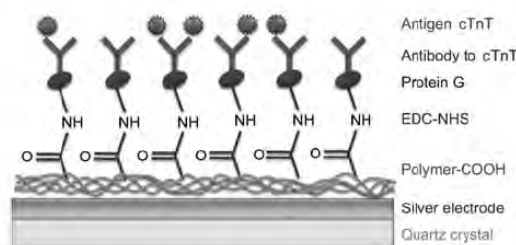


**Figure 1** Illustration of the immobilization scheme of cTnT on quartz crystal.

concentrations of cTnT which were 5, 50, 500, 5000 and 50,000 ng/ml were kept in a cool place at  $-20^{\circ}\text{C}$  until use. Then, the verified cTnT concentrations were used in this experiment.

#### cTnT detection procedure

During immobilization, the flow injection system was kept under a constant PBS flow. The immobilization sequence consisted of multiple reagent injection steps. A schematic diagram of the cTnT immobilization principle is shown in Figure 1. All reagents were injected into the system using the following steps. First, a mixer of 500  $\mu\text{l}$  EDC and 500  $\mu\text{l}$  NHS was injected into the flow system to activate the polymer-coated surface to immobilize Protein G via covalent bonds between a carboxyl group and an amine group. EDC reacted with carboxylic group on polymer surface and NHS was stabilized amide reactive intermediate, thus increasing EDC-mediated coupling reaction with protein. Next, the Protein G coating was performed by injecting 1 ml of 0.025  $\mu\text{g}/\text{ml}$  protein G into the system to initiate binding reaction to the Fc regions of cTnT antibodies. The Protein G coating should considerably improve the response of the sensor at the antibody-antigen binding step. Then, 1 ml of 0.025  $\mu\text{g}/\text{ml}$  cTnT antibody was injected and followed by 1 ml of 0.5 mg/ml Casein blocking reagent. The blocking reagent was used to prevent non-specific reaction of antigen to the excess dangling bonds. For the antigen-antibody binding step, 1 ml of cTnT antigen at fixed concentrations (5, 50, 500, 5000 and 50,000 ng/ml) was injected into the chamber, and allows flow for 20 min (loop system). The cTnT antigen was rinsed off with PBS to remove excess conjugated product. During the course of the experiment, the QCM frequency was recorded. Combined with the cTnT antigen-antibody binding, the frequency shift can now be correctly determined.

## Results and discussion

#### Polymer film morphologies

SEM images of uncoated and coated quartz crystal with 200 nm thick PVC-COOH are shown in Figure 2A and B, respectively. Changes in surface morphology of quartz crys-

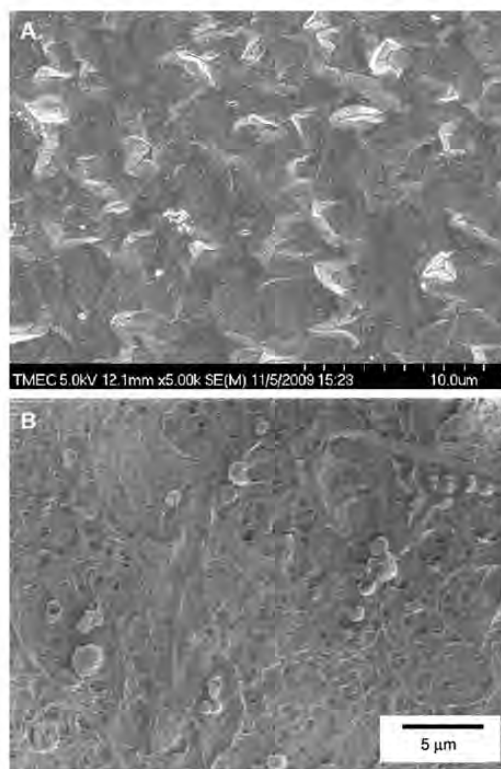


**Figure 2** SEM images show surface morphologies of (A) uncoated and (B) PVC-COOH coated quartz surfaces.

tal after PVC-COOH film deposition can be clearly observed. A step-like surface of the quartz crystal was smoothed by existence of the PVC-COOH film. The relationship between the deposition thickness and the RMS roughness measured by AFM is tabulated in Table 1 and indicates that an uncoated quartz surface consists of a rough surface with RMS roughness of 95.72 nm. The roughness decreases to 6.72 nm with a presence of 100 nm thick PVC-COOH film. The RMS roughness then increases to a value of 56.87 nm with an increase in deposition thickness to 200 nm. At 300 nm thickness, a polymer surface became flatter with an RMS roughness value of 44.76 nm, which is most likely due to coalescence of polymer film. The optimum value of RMS roughness at 200 nm thick film could be beneficial for immobilization of protein due to the largest

**Table 1** Root mean square (RMS) roughnesses of PVC-COOH coated quartz surfaces after polymer films at various thicknesses were deposited. ((\*\*\*author: please confirm that this is the correct Table\*\*\*)

Thickness (nm)	0	100	200	300
RMS roughness (nm)	95.72	6.72	56.87	44.76

surface area available in this series of film coating. For this reason, we selected PVC-COOH polymer film at a thickness of 200 nm to be used as an immobilization layer of the QCM system.

#### Stability of the polymer film under PBS flow

The result (not shown) of an uncoated quartz crystal under various flow rates at 5, 10, 20, 30, 40 and 50 l/min indicated that the negative frequency shift was almost linearly proportional to the flow rate due to the increase in mass loading from the fluid pressures. The frequency shift started from approximately 5 Hz with a flow rate of 5 l/min to around 70 Hz at a flow rate of 50 l/min. However, we found that only at the flow rates of 5 and 40 l/min render a frequency shift stable within 5 min after the injection. The unstable frequency shift at other flow rates is most likely due to fluctuation in the fluid velocity after interacting with polymer-coated surface. For this reason, we maintained the flow of 5 l/min for the rest of the experiments.

#### cTnT detection

The frequency shift response of the PVC-coated QCM sensor which included all immobilization procedures, starting from initial PBS flow to antibody-antigen binding step on the QCM sensor surface, is shown in Figure 3 as time progressing steps from (A) to (H). In step (A), the PBS flow was introduced into the system that resulted in frequency fluctuation of approximately 200 Hz. After 15 min, the frequency shift became stable and the mix of EDC/NHS was injected into the flow system as shown in step (B). At this step, the frequency fluctuates down and up at a frequency range of approximately 1 kHz due to an abrupt change in viscosity. This type of fluctuation was expected for every injection step. The EDC/NHS was injected at a continuous rate for 15 min. After the flow stopped, the frequency dropped and became stable at a frequency shift of approxi-

mately 440 Hz below the previous step. This indicates increases in mass loading from adsorption of EDC/NHS on the PVC-coated QCM surface. In step (C), diluted Protein G was injected into the system and resulted in another frequency fluctuation. After injecting Protein G for 10 min and then stopped, the frequency shift was approximately 150 Hz below the previous step. However, the plot shows that the resonant frequency gradually increased within a range of 50 Hz before the cTnT antibody was introduced into the system at step (D). This increase in frequency suggests that Protein G adsorbed on the QCM surface was partially dissolved by PBS buffer. At step (D), the cTnT antibody was injected into the system for 10 min and resulted in a stable frequency shift of approximately 50 Hz from the binding activity between Protein G and antibody. The frequency was stable under PBS flow for 30 min until the Casein blocking reagent was introduced in step (E). After this step, the frequency dropped approximately 200 Hz due to additional mass from Casein.

The Ab-Ag binding activity can be seen after cTnT antigen was injected into the system for 2 min at step (F). It can be observed that QCM responds well to the controlled concentration of the cTnT at 50 ng/ml under 20 min of the loop flow between step (F) and (G). At step (G), the loop flow was disconnected and PBS rinse was performed. After this step, the plot shows that resonant frequency still decreased for another 25 min, then increased from a removal of the excess binding. The frequency became stable after 20 min, which produced the frequency shift at a steady state of  $\Delta f = 150$  Hz. The noise level of this measurement was less than  $\pm 5$  Hz. The total time for the preparation step (A) to (F) was 2 h and 40 min, and 1 h for response time in cTnT antibody-antigen reaction to from step (F) to steady state in step (H).

The experiment was repeated with cTnT at other concentrations ranging between 5 ng/ml and 50  $\mu$ g/ml and the results are plotted in Figure 4, with the values of cTnT con-

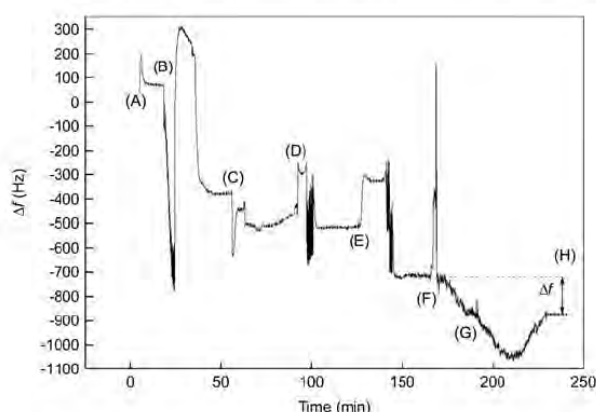


**Figure 3** Frequency response of modified QCM sensor under continuous flow system at multiple immobilization steps (A) introducing PBS flow, (B) EDC/NHS adsorption, (C) Protein G coating, (D) cTnT Ab coating, (E) Casein blocking reagent coating, (F) Ab-Ag complex, (G) PBS rinse and (H) steady-state level of 50 ng/ml cTnT detection.



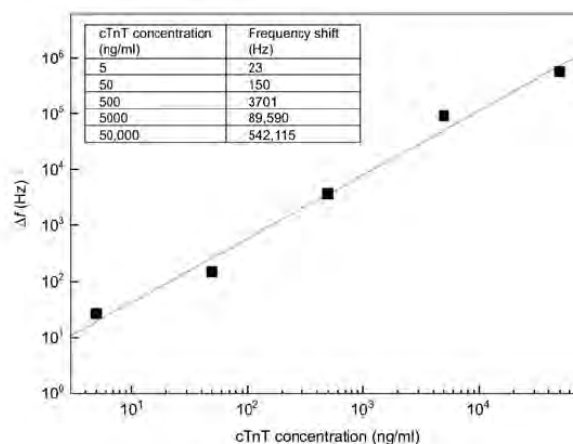


Figure 4 QCM frequency shift of modified QCM sensor as a function of cTnT concentration.

centration and average frequency shift data shown in the inset. The frequency shifts were found to be proportional to the cTnT concentration, which started from 23 Hz at the cTnT concentration of 5 ng/ml. The frequency shift increased drastically to 3.7 kHz, whereas the cTnT concentration reaches 0.5 g/ml. At a concentration of 50 g/ml, the frequency shift increased to 542 kHz. This value was close to the upper detectability limit of QCM, which was around 1 MHz for 12 MHz QCM. We can conclude from this data that our system can detect diluted cTnT down to the detection limit at a concentration of 5 ng/ml. At the lower concentration, the frequency shift was embedded under the noise level (around  $\pm 5$  Hz) and cannot be calculated.

Although the sensitivity of this report is much lower than other recent methods used in clinical measurements, the use of the QCM for disposable low cost and reliable cTnT immunosensor can be beneficial as an alternative screening diagnosis. The ultrahigh sensitivity might be achieved by increasing the frequency range and combining with other surface modification techniques [2, 6, 12, 19, 27, 32].

#### Reusability

After the experiment was done, a modified QCM was regenerated by rinsing its quartz surface with 0.1 M sodium hydroxide. The protein layer was removed from surface by changing the pH value to alkaline. Then the crosslinker layer was rearranged by changing the environment to pH 7.4. Following this procedure, the PVC-COOH coated QCM was successfully reused to collect new experimental data up to three times.

#### Conclusion

In conclusion, we developed a sensitive cTnT detection method by using a surface-modified QCM. The quartz surface of a commercial QCM was coated with a 200-nm thick

PVC-COOH using the spray coating technique. To initiate surface capability of antibody-antigen binding complex, we used a flow injection system with attachments of crosslinker reagents onto the modified quartz surface. The PVC-COOH coated quartz surface demonstrated an effectiveness of cTnT detection. The frequency shift was found to be proportional to the cTnT concentrations. The sensitivity limit of the developed QCM system for the cTnT detection was 5 ng/ml with a noise level less than  $\pm 5$  Hz. The PVC-coated QCM was successfully reused to collect new experimental data up to three times.

#### Acknowledgements

This research was supported by the National Electronics and Computer Technology Center (NECTEC) and the Technology for Development Agency and the Thailand Graduate Institute of Science and Technology (TGIST), research grant of National Science NSTDA, Ministry of Science and Technology, Thailand.

#### References

- [1] Apple FS, Wu AHB. Myocardial infarction redefined role of cardiac troponin testing. *Clin Chem* 2001; 47: 377–379.
- [2] Brunauer S, Emmett PH, Teller E. Adsorption of gases in multimolecular layers. *J. Am Chem Soc* 1938; 60: 309–319.
- [3] Cummins B, Auckland ML, Cummins P. Cardiac-specific troponin-I radioimmunoassay in the diagnosis of acute myocardial infarction. *Am Heart J* 1987; 113: 1333–1344.
- [4] Daunert S, Bachas LG. Ion-selective electrodes using an ionophore covalently attached to carboxylated poly (vinyl chloride). *Analyst* 2008; 133: 635–642.
- [5] Diethelm J. Studies of viscoelasticity with the QCM piezoelectric sensors. Berlin: Springer 2006.
- [6] Ekinici KL, Huang XM, Roukes ML. Ultrasensitive nanoelectromechanical mass detection. *Appl Phys Lett* 2004; 84: 4469–4471.

- [7] Garcia R, Dixon M, Danial T, Allara D, Chana MHW. Ultra-sensitive quartz crystal microbalance with porous gold electrodes. *Appl Phys Lett* 2004; 84: 628–630.
- [8] Giannitsis E, Kurz K, Hallermayer K, Jarausch J, Jaffe AS, Katus HA. Analytical validation of a high-sensitivity cardiac troponin T assay. *Clin Chem* 2010; 56: 254–261.
- [9] Helleskov ML, Ladefoged S, Hildebrandt P, Atar D. Comparison of four different cardiac troponin assays in patients with end-stage renal disease on chronic haemodialysis. *Acute Card Care* 2008; 10: 173–180.
- [10] Jaffe AS, Ravkilde J, Roberts R, et al. It's time for a change to a troponin standard. *Circulation* 2000; 102: 1216–1220.
- [11] Jimenez Y, Fernandez R, Torres R, Arnao A. A contribution to solve the problem of coating properties extraction in quartz crystal microbalance applications. *IEEE Trans Ultrason Ferroelectr Freq Control* 2006; 53: 1057–1072.
- [12] Jusys Z, Bruckenstein S. Electrochemical quartz crystal microbalance study of perchlorate and perchlorate anion adsorption on polycrystalline gold electrode. *Electrochem Commun* 2000; 2: 412–416.
- [13] Katus HA, Rempis A, Looser S, Hallermeier K, Scheffold T, Kubler W. Enzyme linked immuno assay of cardiac troponin T for the detection of acute myocardial infarction in patients. *J Mol Cell Cardiol* 1989; 21: 1349–1353.
- [14] Katus HA, Rempis A, Neumann FJ, et al. Diagnostic efficiency of troponin T measurements in acute myocardial. *Circulation* 1991; 83: 902–912.
- [15] Kikuchi M, Omori K, Shiratori S. Quartz crystal microbalance (QCM) sensor for ammonia gas using clay and polyelectrolyte layer-by-layer self-assembly film. *Proc IEEE Sens* 2004; 2: 718–721.
- [16] Koshets IA, Kazantseva ZI, Shirshov YM. Polymer films as sensitive coatings for quartz crystal microbalance sensors array. *Semiconduct Phys Quant Electron Optoelectron* 2003; 6: 505–507.
- [17] Lau OW, Shao B, Zhang W. Evaluation of methods to minimize effects of liquid viscosity and density on the oscillating frequencies of thickness-shear-mode (TSM) piezoelectric resonators. *Anal Chim Acta* 1995; 312: 217–222.
- [18] Lau RCW, Choi MMF, Lu J. Alcohol sensing membrane based on immobilized ruthenium (II) complex in carboxylated PVC and surface covalently bonded alcohol oxidase. *Talanta* 1999; 48: 321–331.
- [19] Lin Z, Yip CM, Joseph IS, Ward MD. Operation of an ultra-sensitive 30 MHz quartz crystal microbalance in liquids. *Anal Chem* 1993; 65: 1546–1551.
- [20] Lindner E, Cosofret VV, Buck RP, et al. Electroanalytical and biocompatibility studies on microfabricated array sensors. *Electroanalysis* 2005; 7: 864–870.
- [21] Liu YC, Wang CM, Hsiung KP. Comparison of different protein immobilization methods on quartz crystal microbalance surface in flow injection immunoassay. *Anal Biochem* 2001; 299: 130–135.
- [22] Lu QW, Morimoto S, Harada K, et al. Cardiac troponin T mutation found in dilated cardiomyopathy stabilizes the troponin T-tropomyosin interaction and causes Ca<sup>2+</sup> desensitization. *J Mol Cell Cardiol* 2003; 35: 1421–1427.
- [23] Lucklum R, Behling C, Hauptmann P. Role of mass accumulation and viscoelastic film properties for the response of acoustic-wave-based chemical sensors. *Anal Chem* 1999; 71: 2488–2496.
- [24] Lucklum R, Hauptmann P. The quartz crystal microbalance mass sensitivity viscoelasticity and acoustic amplification. *Sens Actuators B Chem* 2000; 70: 30–36.
- [25] Muller BM, Hallermayer K, Schröder AA. Improved troponin T ELISA specific for cardiac troponin T isoforms assay development and analytical and clinical validation. *Clin Chem* 1997; 43: 458–466.
- [26] Piao MH, Noh HB, Rahman MA, Won MS, Shim YB. Label-free detection of bisphenol A using a potentiometric immunosensor. *Electroanalysis* 2007; 20: 30–37.
- [27] Rabe J, Buttgenbach S, Schroder J, Hauptmann P. Monolithic miniaturized quartz microbalance array and its application to chemical sensor systems for liquids. *IEEE Sens J* 2003; 3: 361–368.
- [28] Reimhult K, Yoshimatsu K, Risveden K, Chen S, Ye L, Krozer A. Cardiac-specific troponin-I radioimmunoassay in the diagnosis of acute myocardial infarction. *Biosens Bioelectron* 2008; 23: 1908–1914.
- [29] Si P, Mortensen J, Komolov A, Denborg J, Moller PJ. Polymer coated quartz crystal microbalance sensors for detection of volatile organic compounds in gas mixtures. *Anal Chim Acta* 2007; 597: 223–230.
- [30] Surugiu I, Danielsson B, Ye L, Mosbach K, Haupt K. Chemiluminescence imaging ELISA using an imprinted polymer as the recognition element instead of an antibody. *Anal Chem* 2001; 73: 487–491.
- [31] Tunstall PH, Kuulasmaa K, Amouyel P, Arveiler D, Rajakangas AM, Pajak A. Myocardial infarction and coronary deaths in the World Health Organization MONICA Project. *Circulation* 1994; 90: 583–612.
- [32] Utenthaler E, Schraml M, Mandel J, Drost S. Ultrasensitive quartz crystal microbalance sensors for detection of m13-phages in liquids. *Biosens Bioelectron* 2001; 12: 735–743.
- [33] Wu AHB, Agee SJ, Lu QA, Todd J, Jaffe AS. Specificity of a high-sensitivity cardiac troponin I assay using single-molecule-counting technology. *Clin Chem* 2009; 55: 196–198.

Received February 18, 2010; accepted June 21, 2010



## Surface-enhanced Raman scattering substrate of silver nanoparticles depositing on AAO template fabricated by magnetron sputtering

Noppadon Nuntawong<sup>a,\*</sup>, Mati Horprathum<sup>a</sup>, Pitak Eiamchai<sup>a</sup>, Krongkamol Wong-ek<sup>b</sup>, Viyapol Patthanasettakul<sup>a</sup>, Pongpan Chindaudom<sup>a</sup>

<sup>a</sup> Photonics Technology Laboratory, National Electronics and Computer Technology, 112 Thailand Science Park, Patumthani, Thailand  
<sup>b</sup> Nanoscience and Technology Program, Chulalongkorn University, Bangkok, Thailand

### ARTICLE INFO

#### Article history:

Received 8 July 2009  
 Received in revised form  
 22 December 2009  
 Accepted 26 December 2009

#### Keywords:

Silver nanoparticles  
 Raman scattering  
 SERS  
 Magnetron sputtering  
 AAO  
 Sensor

### ABSTRACT

In this report, we describe a fabrication process of low-cost and highly sensitive SERS substrates by using a simple anodizing setup and a low-energy magnetron sputtering method. The structure of the SERS substrates consists of silver nanoparticles deposited on a layer of anodic aluminum oxide (AAO) template. The fabricated SERS substrates are investigated by a scanning electron microscope (SEM), a transmission electron microscope (TEM), and a confocal Raman spectroscope. We have verified from the surface morphology that the fabricated SERS substrates consist of high-density round-shape silver nanoparticles where their size distribution ranges from 10 to 30 nm on the top and the bottom of nanopores. The surface-enhanced Raman scattering activities of these nanostructures are demonstrated using methylene blue (MB) as probing molecules. The detection limit of  $10^{-8}$  M can be achieved from this SERS substrate.

© 2010 Elsevier Ltd. All rights reserved.

### 1. Introduction

Raman spectroscopy, based on an inelastic scattering of photons, has been used to identify a wide variety of chemical and biological molecules by their Raman spectra. However, a conventional Raman spectroscopy suffers from a small scattering cross section. The problem can be solved by a surface-enhanced Raman scattering (SERS) technique which greatly enhances the sensitivity of the conventional Raman spectroscopy [1–6]. This powerful technique hence is applicable to detect molecular species and has recently drawn a considerable attention in researches in chemical and biological analyses. In addition, SERS offers several potential advantages over other spectroscopic techniques because of its measurement speed, high sensitivity, portability, and simple maneuverability.

Despite a considerable number of researches in the SERS technique, its mechanism is still under debated [3]. In general, enhancement factors for the SERS substrates are reported between  $10^5$  to  $10^8$  [7–10]. Note that, an extraordinarily high enhancement factor ( $\sim 10^{14}$ ) was reported on an active SERS system using colloidal silver molecules [11,12]. However, metal colloid suffers from its aggregation states. Although different analytes produce different aggregation states, they equally impose unreliable Raman

intensity and difficulty for standardization. Lithography is another ideal method for producing uniform and reproducible SERS substrates [13,14]. Although their enhancement factor can be achieved up to  $\sim 10^9$  [14], the lithographic technique is very expensive in a large-area production of the SERS substrates. In this work, we here report a fabrication process of low-cost and highly sensitive SERS substrates, based on a magnetron sputtering system. The magnetron sputtering technique has a primary advantage in an easy adaptation to a large-scale production. We use the magnetron sputtering system to deposit silver nanoparticles on top of a thin AAO template which is previously coated on each silicon substrate. The presence of the AAO template helps increase the surface area and prevent coalescence of the deposited silver nanoparticles. The AAO template thus maintains a high density of the silver nanoparticles to obtain a large SERS enhancement factor. Note that the silicon-based support makes the SERS substrates easier to handle than those fabricated on fragile porous alumina foils as previously reported [15].

### 2. Experimental details

#### 2.1. Sputtering system

All of the metal nanoparticles in the SERS substrates are prepared by a homemade high vacuum (HV) DC magnetron

\* Corresponding author.

E-mail address: [noppadon.nuntawong@nectec.or.th](mailto:noppadon.nuntawong@nectec.or.th) (N. Nuntawong).

sputtering system. Its deposition chamber reaches a base pressure at approximately  $1 \times 10^{-3}$  Pa. During the film deposition, an operating pressure is maintained at 0.4 Pa by a throttle valve. Plasma cleaning is performed for 5 min prior to the metal deposition on the silicon surface using 70 W of an RF power, 16.25 MHz of an RF frequency, and 5 sccm of an argon flow. The metal deposition is then followed with a DC sputtering power of 34 W.

## 2.2. Preparation of AAO templates

For each AAO template, a 120 nm thick aluminum film is first deposited on a (100) silicon substrate. In an anodizing step, the substrate is connected to a power supply of an anodic electrode, and subsequently immersed in 0.3 M oxalic acid. A gold plate on the silicon substrate is used as a cathodic electrode. The anodizing current is precisely controlled by a Motect's LPS-305 digital power supply at the current of 10 mA with the voltage limit of 40 V. During this step, a large fraction of the aluminum film will be transformed into nanopores confined to 5–10 nm  $\text{Al}_2\text{O}_3$  side walls. The substrate is then submerged in 5 wt%  $\text{H}_3\text{PO}_4$  for 30 min in order to remove the  $\text{Al}_2\text{O}_3$  layer, thus opening cylindrical nanochannels along the top surface of the AAO film toward the silicon surface.

## 2.3. Sputtering of silver nanoparticles

The silver nanoparticles are deposited on each AAO template by the DC magnetron sputtering system. The sputtering target is a 3-inch high-quality pure (99.99%) silver manufactured by K.J. Lesker. The deposition rate is approximately 1 nm/s as calibrated by a spectroscopic ellipsometer (HS-190) manufactured by J.A. Woollam.

## 2.4. Surface characterizations and analyses

The film thickness is verified by Hitachi's s-5200 field emission scanning electron microscope (FE-SEM). The FE-SEM is also used to examine the lateral features of the AAO nanopores and the silver nanoparticles deposited on their matrix. The cross-sectional details of the SERS structures are characterized by JEOL 2010 (200 kV) transmission electron microscope (TEM).

## 2.5. Raman scattering characteristics

The fabricated SERS substrates are cut into several  $5 \times 5 \text{ mm}^2$  pieces. Each of these samples will be one time used to characterize reference molecules. In this report, methylene blue (MB) is selected as probing molecules on the fabricated substrates in order to determine the SERS activities. A sensitive NT-MDT NTEGRA Raman spectrometer equipped with a confocal optical microscopy system is used to characterize the Raman spectra. Prior to the measurements, a drop of methylene blue (MB) at  $5 \times 10^{-2}$  mL in volume is deposited on each SERS surface. The sample with the MB droplet is left to dry at room temperature in an air atmosphere, and is immediately measured for the Raman spectra using a 633 nm He-Ne laser excitation. In this study, the Raman scattering characteristics are conducted as the MB concentration varies between  $5 \times 10^{-8}$  M and  $5 \times 10^{-3}$  M.

## 3. Results and discussion

### 3.1. Physical characteristics of SERS substrates

Fig. 1(a) shows the top-view image of one SERS substrate taken by the FE-SEM. The image illustrates a uniform nanopore array with

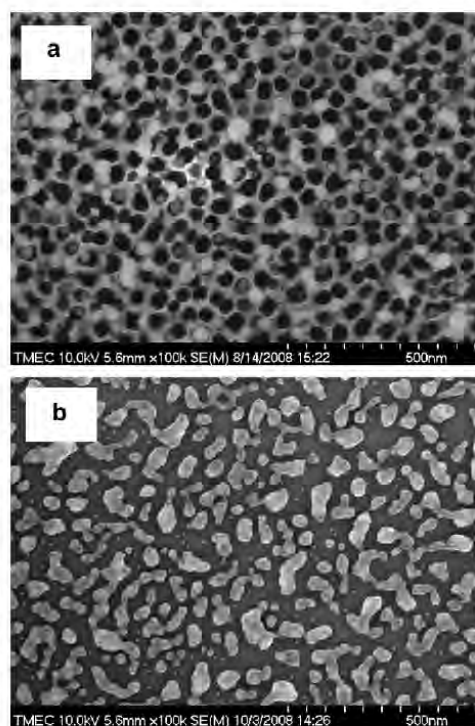


Fig. 1. SEM images of the SERS substrates with the silver nanoparticles deposited by the magnetron sputtering for 8 seconds (a) on the AAO template (b) on the Si surface.

a pore size distribution between 30 and 40 nm, and an interpore distance around 80–100 nm. The silver nanoparticles with the diameter size around 10–30 nm are observed both on the inside and outside of the AAO nanochannels. The density of the silver nanoparticles on this particular sample is about half of that of the nanopore array at approximately  $1 \times 10^{10} \text{ cm}^{-2}$ . Without the AAO template, these nanoparticles will migrate along the substrate surface and coalesce to form a larger island as shown in Fig. 1(b). The coalescence results in the decrease in the density and the surface area of silver nanoparticles that can be bounded by the probing molecules. The coalescence hence reduces the coupling effect between the silver nanoparticles and degrades the Raman enhancement factor.

The structural details of the SERS substrates are further investigated by cross-sectional TEM images. One of the images has been selected and shown in Fig. 2. The TEM image verifies that the nanopores are completely opened from the aluminum top surface down to the silicon substrate interface. In addition, the image reveals the silver nanoparticles embedded on the bottom of the nanochannels and on the top of the AAO surface. The TEM image also indicates the difference in size distribution between the nanoparticles embedded on each layer. The silver nanoparticles on the bottom of the nanochannels range between 10 and 20 nm in size, while those on the top of the AAO range between 20 and 30 nm in size. The size difference is most likely due to a shadowing effect of sputtered material between these two locations.

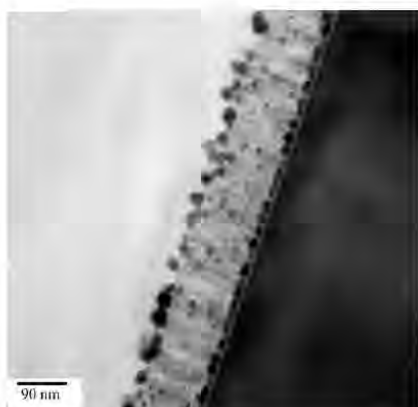


Fig. 2. Cross-sectional TEM images of the SERS substrates with the silver nanoparticles on AAO template.

### 3.2. SERS measurements

The Raman spectra of MB at the concentration of  $5 \times 10^{-3}$  M on the different types of the substrates are presented in Fig. 3. Since the main absorption peaks of MB solution are located at 656, 610 and 293 nm [16], the resonant Raman effect from the excitation wavelength may partially improve the Raman intensities. However, this resonant effect is expected to be much smaller than SERS effect. The normal Raman spectrum of solid MB molecules adsorbed on the silicon substrate without the SERS structure is shown in spectrum (a). The peak at  $520 \text{ cm}^{-1}$  corresponds to the Raman scattering of the crystalline Si substrate. The spectrum indicates that the Raman signal of MB without enhancement is not strong enough to be observed due to small amount of Raman scattering from the material deposited on the Si surface. Spectrum (b) presents the enhancement effect on the Raman scattering of the silver nanoparticles coated directly on the silicon wafer. With this sample, characteristic Raman peaks of MB become visible, indicating enhancement activity from the silver nanoparticles. For the SERS

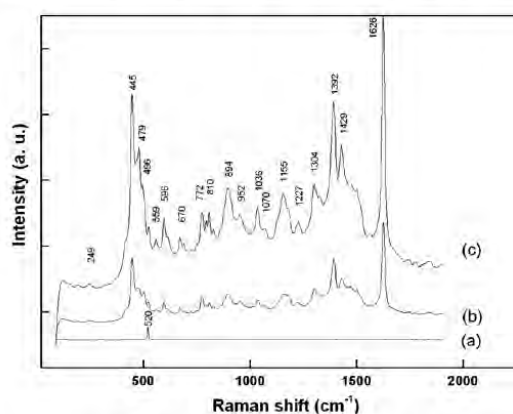


Fig. 3. Raman spectra of the methylene blue droplets at the concentration of  $5 \times 10^{-3}$  M as left dried on (a) the Si substrate, (b) the silver nanoparticles deposited on the Si substrate, and (c) the silver nanoparticles deposited on the AAO template.

substrate with the silver nanoparticles embedded in the AAO template, the Raman intensities increase drastically as shown in spectrum (c). This suggests that the coalescence of the silver nanoparticles is an important factor that limits the Raman enhancement factor of these substrates. That is, the presence of nanochannels increases the surface area for the deposition of the silver nanoparticles and suppresses the coalescence. These results in further enhancement of the SERS intensities and thus allow the SERS substrates to reveal several molecular details of the MB molecules adsorbed on their surface.

Fig. 4 shows the Raman spectra of MB with the concentrations varied from  $5 \times 10^{-2}$  M to  $5 \times 10^{-8}$  M on the fabricated SERS substrate. One of the interesting features that should be pointed out here is the comparison in the SERS intensities between MB with the concentrations of  $5 \times 10^{-3}$  M and  $5 \times 10^{-2}$  M. At this point, the SERS intensity increases, instead of decreases, with a decrease in the MB concentration. This indicates that the enhanced Raman signal is generated only from a thin layer of analyte molecules embedded close to the metal nanoparticles. Other additional layer of analyte molecules weakens the scattering signal, instead of the strengthening. The Raman scattering intensities decrease at concentrations below  $5 \times 10^{-3}$  M, which indicate reduction in MB monolayer film deposited on the SERS substrates. The Raman intensity almost disappears for MB at  $5 \times 10^{-8}$  M concentration compared to that of the higher MB concentrations. However, the inset shows that some of MB band peaks can still be able to observe at this ultra low concentration. This verified a high sensitivity of this fabricated SERS substrate.

### 3.3. Calculation of Raman enhancement factors

The observed MB band positions are in general agreement with the previously published results [17–21]. For quantitative comparison, we use the Raman enhancement factor which is defined as the ratio of the elastic scattering intensity per molecule between the presence and the absence of SERS. The Raman enhancement factor is written as [15–18]:

$$G = \frac{I_{\text{SERS}} \cdot N_{\text{Ref}}}{I_{\text{Ref}} \cdot N_{\text{SERS}}}$$

In this formula,  $I_{\text{SERS}}$  is the enhanced intensity of the adsorbed MB molecules on the SERS substrate.  $I_{\text{Ref}}$  is the spontaneous Raman

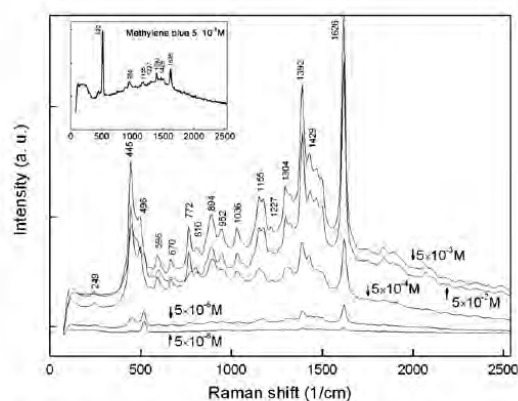


Fig. 4. Raman spectra of the methylene blue droplets with different concentrations on the SERS substrates. An inset shows spectrum of the droplet at  $5 \times 10^{-8}$  M.

scattering intensity from the bulk MB molecules under the laser spot on the blank Si substrate.  $N_{\text{Ref}}$  is defined as the number of the bulk MB molecules excited by the laser without Raman enhancement effect. For a scattering volume of  $1000 \mu\text{m}^3$ ,  $N_{\text{Ref}}$  is approximately  $3.3 \times 10^{11}$  molecules.  $N_{\text{SERS}}$  is the number of molecules uniformly spreading on SERS substrate under laser spot. Using a  $100\times$  objective lens, the area of laser spot is around  $1 \mu\text{m}^2$ . As the maximum SERS intensity is obtained from MB at concentration of  $5 \times 10^{-3}$  M, which is corresponding to  $10^4$  monolayers of MB, the value of  $N_{\text{SERS}}$  under laser excitation is therefore  $6 \times 10^9$  molecules. We now obtain the average values of the enhancement factors for the spectrum (b) and (c) in Fig. 3 as  $4.46 \times 10^3$  and  $1.71 \times 10^4$ , respectively. Note that, if we assume a monolayer of molecules for the value of  $N_{\text{SERS}}$  as reported previously [16,17], the enhancement factor of these SERS will be on the order of  $10^8$ . However, there is still no consensus that the SERS signal mainly arises from a single molecule layer covering on nanoparticle array.

#### 4. Conclusions

We have discussed the fabrication process of the low-cost and highly sensitive SERS substrates, which can be achieved by the deposition of the silver nanoparticles on the AAO templates using the magnetron sputtering system. Using the AAO templates, the coalescence of the silver nanoparticles can be suppressed. The density of silver nanoparticles deposited on the SERS substrates can be optimized to be more than  $1 \times 10^{10} \text{cm}^{-2}$ . By using methylene blue as the reference analyte, the SERS substrates allow an excellent observation of the MB molecular details and offer the enhancement factor more than  $1.71 \times 10^4$ . In addition, the SERS substrates fabricated in this report has detectability to MB at the ultra low

concentration of  $10^{-8}$  M. These results suggest that the developed SERS substrates are promising in applications of chemical detections and analyses. For future work, we expect to optimize the nanochannel size and thickness of the AAO arrays which would further increase the SERS enhancement factors for this structure.

#### References

- [1] Chaney SB, Shanmukh S, Dluhy RA, Zhao Y-P. *Appl Phys Lett* 2005;87:031908.
- [2] Fang J, Yi Y, Din B, Song X. *Appl Phys Lett* 2008;92:131115.
- [3] Yan F, Vo-Dinh T. *Sens Actuators B* 2007;121:61.
- [4] Liu GL, Lee LP. *Appl Phys Lett* 2005;87:074101.
- [5] Alexander TA, Le DM. *Appl Opt* 2007;46:3878.
- [6] Suzuki M, Maekita W, Wada Y, Nakajima K, Kimura K, Fukuoka T, et al. *Appl Phys Lett* 2006;88:203121.
- [7] Ruan C, Eres G, Wang W, Zhang Z, Gu B. *Langmuir* 2007;23:5757.
- [8] Gu GH, Kim J, Kim L, Suh JS. *J Phys Chem C* 2007;111:7906.
- [9] Lombardi I, Cavallotti PL, Carraro C, Maboudian R. *Sens Actuators B* 2007;125:353.
- [10] Driskell JD, Shanmukh S, Liu Y, Chaney SB, Tang X-J, Zhao Y-P, et al. *J Phys Chem C* 2008;112:895.
- [11] Nie S, Emory SR. *Science* 1997;275:1102.
- [12] Wang Y, Kneipp H, Perelman LT, Itzkan I, Dasari RR, Feld MS, et al. *Phys Rev Lett* 1997;78:1667.
- [13] Liao PF, Bergman JG, Chemla DS, Wokaun A, Melngailis J, Hawryluk AM, et al. *Chem Phys Lett* 1981;82:355.
- [14] Zhang X, Yonzon CR, Young MA, Stuart DA, Van Duyne RP. *IEEE Proc Nanobiotechnol* 2005;152.
- [15] Walsh RJ, Chumanov G. *Appl Spectrosc* 2001;55:1695.
- [16] Xiao GN, Man SQ. *Chem Phys Lett* 2007;447:305.
- [17] Laurent G, Féridj N, Aubard J, Lévi G. *Phys Rev B* 2005;71:045430.
- [18] Jiang H, Chen WX, Xu ZD. *Chin J Chem Phys* 1998;11:82.
- [19] Féridj N, Aubard J, Lévi G, Krenn JR, Salerno M, Schiner G, et al. *Phys Rev B* 2005;71:075419.
- [20] Naujok RR, Duevel RV, Corn RM. *Langmuir* 1993;9:1771.
- [21] Hulchineon K, Heater R, Albery J, Hillman AR. *J Chem Soc Faraday Trans* 1984;1(80):2053.

## QCM BASED ON FLOW SYSTEM FOR CARDIOVASCULAR DISEASE

K. Wong-ek<sup>1</sup>, O.Chailapakul<sup>1</sup>, J. Prommas<sup>2</sup>, K. Jaruwongrungrsee<sup>3</sup>, N. Nuntawong<sup>4</sup>,  
and A. Tuantranont<sup>3</sup>

<sup>1</sup>Nanoscience and Technology Graduate Program, Chulalongkorn University, THAILAND  
Email: wongek@tu.ac.th

<sup>2</sup>Biosensor Laboratory, Faculty of Medical Technology, Mahidol University, THAILAND

<sup>3</sup>Nanoelectronics and MEMS Laboratory, National Electronics and Computer Technology Center

<sup>4</sup>Photonic Technology Laboratory, National Electronics and Computer Technology Center  
Pathumthani, THAILAND

**Abstract**— Quartz Crystal Microbalance (QCM) is a special sensor which has acoustic impedance detector by mass loading. In this study Cardiac Troponin T (CTnT) which elevates in all patients with AMI diagnosed by World Health Organization (WHO) criteria is used as immunological assay onto sensor. Detection of the Troponin T is developed based on antigen - antibody system on QCM sensor as solid support and signal transduction for immobilization to monitor risk marker of myocardial infarction. To immobilize antibody, the sensor is functionalized with Polyvinyl chloride (PVC) doped COOH by spray coating technique. The modified sensor testing results can be given in short response time and a direct conversion of mass accumulation into a frequency shift representing a measurable electrical signal. The relationship between the Cardiac Troponin T concentration and the response current could be observed in the minimum concentration range at 5 ng/ml.

**Keywords**— Quartz Crystal Microbalance; Cardiac marker; Acute Myocardial Infarction, Biosensor; Flow injection

### I. INTRODUCTION

Cardiac troponins are part of the new definition of acute myocardial infarction (AMI) by the European Society of Cardiology and the American College of Cardiology (ESC/ACC). They are released into the blood circulation from injured heart muscle cells [1] during cardiac ischemia with no overlap with skeletal muscle troponins under normal conditions. [2] Multiple studies have demonstrated that both cTnI and cTnT are important prognostic indicators in patients presenting chest pain, even when MB fraction of creatine kinase (CK) is not elevated. [3] Particularly, the troponins T is wider accepted as a tool to stratify patients with chest pain, moreover the detection of cardiac troponin might also be useful prognosticator in high risk patients. There are several methods being able to detect troponin T such as enzyme linked immunosorbent assay (ELISA), radioimmunoassay (RIA) which are normally used but there are suffered from relatively low throughput, high reagent

and large amount of sample consumption. Development of fast and sensitive CTnT detecting sensor by Quartz Crystal Microbalance (QCM) with Immunoassay method for the quantification of CTnT protein is great importance because QCM have advance capability in consuming less amount of reagent; therefore less amount of sample is required. Approach for cTnT detection using QCM technique, which has more potential to be truly direct measurements, as well as rapid, specific and user-friendly should be explored.

In 1959, Sauerbrey derived the equation of frequency shift of the quartz resonator in gas phase:

$$\Delta f = -\frac{2f_0^2}{\sqrt{\rho_q \mu_q}} \frac{\Delta M}{A} \quad (1)$$

where:  $\Delta f$  is the frequency shift of the resonator,  $f_0$  is the fundamental frequency,  $\rho_q$  is the density of quartz ( $2.648 \text{ g/cm}^3$ ),  $\mu_q$  is the shear modulus of quartz ( $2.947 \times 10^{11} \text{ g/cm} \times \text{s}^2$ ),  $\Delta M$  is the mass deposited on the surface of electrode and  $A$  is piezoelectrically active area (for the  $2/\sqrt{(\rho_q \mu_q)}$  can be expressed as a constant,  $k$ , which is  $2.26 \times 10^{-7}$ ). This equation can describe the additive mass rigidly deposited on the electrode surface. It can also be approximately applied for humidity and gas sensing. Although the water molecules and gas molecules deposited on the electrode are not rigid material, they can be absorbed by the hygroscopic and gas sensing layer, which is rigidly deposited on the electrode surface.

A modified QCM biosensor, combining the specificity of antibodies [4] with the sensitivity of the quartz crystal microbalance will provide a potentially rapid and direct measurement of CTnT concentration. The bioprobes on gold sensor is expected to have high active region per antigen antibody reaction. The sensor is mass sensitive detectors based on oscillating silver quartz crystal with some certain frequency. Due to complex binding, crystal

frequency will decrease with amount of deposited material and could be used to measure change in its mass.

In this work, surface of QCM is coated with Polyvinyl chloride (PVC) doped COOH, 1-Ethyl-3-[3-dimethylaminopropyl]carbodiimide Hydrochloride (EDC) and *N*-hydroxysuccinimide (NHS). Protein G and CTnT Antibody to detect human CTnT which are specific biochemical assays to provide evidence of acute myocardial infarction (AMI). By our knowledge, CTnT detection based on QCM has not been developed before. The deposited QCM is used as an immunosensor and the relationship of frequency change relative to CTnT concentrations are characterized. [5] and [6]

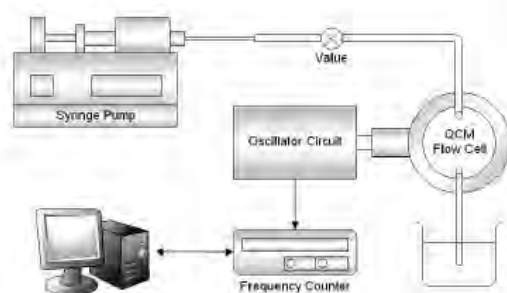


Figure 1 Diagram of developed flow injection system

## II. MATERIALS AND EXPERIMENTAL

### A. Reagents and coating materials

Polyvinyl chloride (PVC), EDC/NHS and Protein G from Streptococcal bacteria are purchased from Sigma-Aldrich Chemical Co. Inc. Biotech grade Tetrahydrofuran (THF) (Merck, Darmstadt, Germany) is used as a solvent of PVC-COOH and is prepared by dissolving 0.25 mg in 10 ml of THF with constant stirring for 10 minute at room temperature. The 1M phosphate buffer saline (PBS, pH 7.4) is used as a buffer solution. Monoclonal antibody 9G6 and Human Cardiac Troponin T are purchased from Abcam Co. Inc.. The mouse monoclonal antibody is of the IgG and is produced for use only in these experiments. Gold surface AT-cut QCM which are 5 MHz frequency range from Stanford Research System, Inc. are used. In this study, flow system is shown in diagram of figure 1. This system is developed by Nanoelectronics and MEMS Laboratory (NECTEC, NSTDA Thailand).

### B. Immobilization procedures

Immobilization of the CTnT – QCM sensor is done by multiple coating steps. Firstly, QCM has to be cleaned prior coating by 1:1 of 30% H<sub>2</sub>O<sub>2</sub> and 96% H<sub>2</sub>SO<sub>4</sub> (Piranha solution) Then spray coating technique is provided in active zone of the QCM surface in a solution of 2.5% PVC-COOH. Then sensor is five times washed in HNO<sub>3</sub> solution to eliminate excess polymer and rinses with PBS buffer and dry with Nitrogen gas (N<sub>2</sub>) before used. The flow system which has a peristaltic pump and manual switching valve connects to laptop with Window XP operating system sent frequency shift directly in every second controlled by developed program. All process are used flow rate at 0.5  $\mu$ l per second [7]. After a QCM is placed, EDC/NHS is injected to QCM chamber system which performed by 1 ml of 25 mM EDC in distilled water mixed with 1 ml of 50 mM NHS in DI, then flowed for 30 minutes in chamber and then followed by 30 minutes flow of PBS solution [8]. After removing excess reagent, the 2 ml of 3  $\mu$ g/ml CTnT antibody is injected and flowed for 30 minutes, and then washed by rinsing PBS buffer for 5 minutes. Figure 2 represents to Scanning Electron Microscope (SEM) image of Protein that adsorbs onto QCM surface.

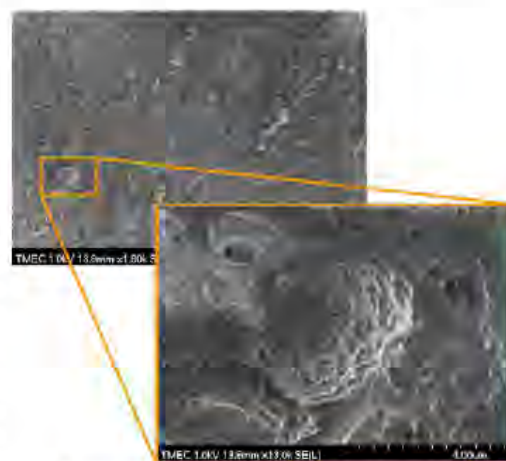


Figure 2 SEM image of the QCM sensor electrode surface after immobilized with protein G.

### C. Analytical procedure

To detect QCM sensor antigen-antibody binding step, CTnT antigen 1 ml of 50 ng/ml is injected into the chamber



then flowed for 60 minutes (loop system) and then rinsed with PBS to remove excess conjugated product. The testing data of frequency shift collects to computer via GPIB port and show in figure 3.

#### D. Reusability

After application is done, modified QCM could be regenerated a cross-linker layer by rinsing sensor with 0.1M Sodium hydroxide. The protein layer is removed from surface by changing pH-value to alkaline area and rearranged crosslinker layer by change environment to pH 7.4 which possible to use for new detection.

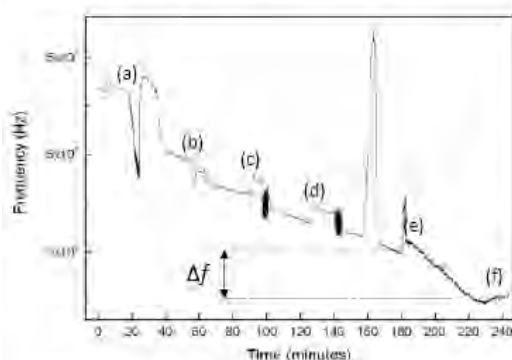


Figure 3 Frequency response for modified QCM sensor as a function of 50 ng/ml CTnT detection (a) EDC/NHS adsorption, (b) Protein G coating, (c) Ab coating, (d) Casme blocking reagent coating (e) Ab-Ag complex and (f) steady-state measured with modified QCM flow injection system.

### III. RESULTS AND DISCUSSION

In this research, the developed QCM sensor is characterized by acoustic resonant frequency analysis. The frequency shift response of QCM sensor which includes antibody-antigen binding immobilized on sensor surface is shown as steps (a)-(d) in Figure. 3. Protein G coating in step (b) is used to increase an ability of CTnT adsorption due to its potential of binding between the Fc region together with CTnT antibody. The sensor coated with protein G should exhibits a good response to the CTnT antigen with short response times. It can be seen after step (e) that the Ab-Ag binding can respond well to the controlled relative concentration of CTnT at 50 ng/ml, which produce the frequency shift after steady state of  $\Delta f = 400$  Hz. The noise level of this measurement is less than  $\pm 10$  Hz. The total

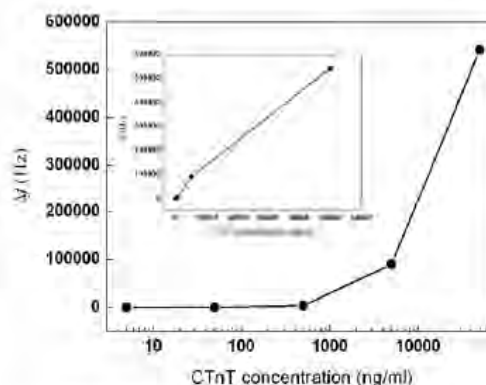


Figure 4 Linear-logarithmic relation between CTnT concentration and frequency shift plotting (inset) linear-linear relation

response time for the preparation step (a)-(d) of each sample is 2 hours and from antibody reacts with CTnT antigen from (e) to (f) is 60 minutes. The frequency responses from other tests are found to be stable and proportional to the CTnT concentration down to detection limit at CTnT concentration of 5 ng/ml.

Figure 4 shows the relation between frequency shift and CTnT concentration. The frequency response can be quantified from CTnT with concentration of 5 ng/ml, which is corresponding to a frequency shift of 23 Hz. The frequency shift increase drastically to around 90 kHz while the CTnT concentration reach 5  $\mu$ g/ml. With CTnT concentration of 50  $\mu$ g/ml, the frequency shift increase to around 542 kHz, this is close to the upper limit of system (using 5 MHz QCM) detectability at around 1 MHz.

### IV. CONCLUSIONS

In conclusion, we have developed a Cardiac Troponin T sensor by spray coating technique of PVC-COOH with attachments of cross linker reagents onto a commercial quartz crystal resonator. To improve surface capability of antibody-antigen binding complex, we use a flow injection system in this experiment. The modified QCM electrode is shown an effectiveness of increased adsorption ability for protein-G. The sensitivity of coated sensor is increased tremendously compared to uncoated sensor. The frequency shift has found to be proportional to CTnT concentrations. The highest sensitivity of modified CTnT-QCM detection is 5 ng/ml with noise level less than  $\pm 10$  Hz.

## ACKNOWLEDGEMENTS

This research is supported by National Electronics and Computer Technology Center research grant of National Science and Technology for Development Agency, Ministry of Science and Technology, Thailand.

## REFERENCES

1. Hougen HP, Valenzuela A, Lachica E, Villanueva, E. (1992) Sudden cardiac death: a comparative study of morphological, histochemical and biochemical methods. *Foren Sci Int.* 52, 161-169.
2. Mair J, Dienstl F, Puschendorf B. (1992) Cardiac troponin T in the diagnosis of myocardial injury. *Critical reviews in clinical laboratory sciences.* 29, 31-57.
3. De Winter RJ, Koster RW, Sturk A, Sanders GT. (1995) Value of myoglobin, troponin T, and CK-MBmass in ruling out an acute myocardial infarction in the emergency room. *Circulation.* 92, 3401-3407.
4. B. Cummins, M.L. Auckland, P. Cummins. (1987) *Am. Heart J.* 113.1333-1344.
5. J. Rabe, S. Buttgenbach, J. Schroder, and P. Hauptmann, "Monolithic miniaturized quartz microbalance array and its application to chemical sensor systems for liquids," *IEEE Sensors Journal*, Vol. 3, pp. 361 - 368, August 2003.
6. Masashi Kikuchi, Katsuya Omori, and Seimei Shiratori, "Quartz Crystal Microbalance (QCM) Sensor for Ammonia Gas using Clay/Polyelectrolyte Layer-by-Layer Self-Assembly Film," *IEEE Sensors Proceedings 2004*, vol. 2, pp. 718-721, October 2004.
7. M. Michalzik, R. Wilke, S. Buttgenbach, "Miniaturized QCM-based flow system for immunosensor application on liquid," *Sensors and Actuators B*, pp. 410-415, April 2005
8. Y. Jimenez, R. Fernandez, R. Torres, and A. Arnau, "A contribution to solve the problem of coating properties extraction in quartz crystal microbalance applications," *IEEE Transactions on Ultrasonics, Ferroelectrics, and Frequency Control*, Vol. 53, pp. 1057 - 1072, May 2006.